Experimentally Determined Material Parameters for Temperature Prediction of an Automobile Tire using Finite Element Analysis

by

Willem Burger van Blommestein

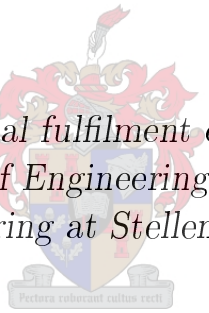

Thesis presented in partial fulfilment of the requirements for the degree of Master of Engineering (Mechanical) in the Faculty of Engineering at Stellenbosch University

Supervisor: Prof. G. Venter
Co-supervisor: Dr. M.P. Venter

December 2016

Declaration

By submitting this thesis electronically, I declare that the entirety of the work contained therein is my own, original work, that I am the sole author thereof (save to the extent explicitly otherwise stated), that reproduction and publication thereof by Stellenbosch University will not infringe any third party rights and that I have not previously in its entirety or in part submitted it for obtaining any qualification.

Date: ...December 2016.....

Abstract

The following report documents the experimental determination and validation of a tires material parameters for use in a thermal finite element simulation procedure. Uni-axial tensile tests were performed on tire samples. The force displacement response of each was used to determine material properties by means of direct curve fits and iterative numerical procedures. Equivalent finite element simulation models were used to validate the properties. Hysteresis behaviour of the rubber regions were identified by dynamic mechanical analysis. Material definitions were incorporated into existing finite element models developed by Maritz (2015) to predict the steady-state heat generation and temperature distribution within a tire due to hysteresis. The use of material properties from literature resulted in inaccurate model predictions when compared to experimental measurements. A series of validation experiments and equivalent simulations were performed in order to evaluate the resulting structural response. The updated models provided accurate predictions of structural deformation and tread contact pressure distributions under a variety of loading conditions. Experimental rolling tire temperature measurements were taken on a test bench. A comparison of the results with those obtained from the equivalent thermal models revealed remarkable similarities and improvements.

Uittreksel

Die volgende verslag dokumenteer die eksperimentele bepaling en bekragtiging van 'n voertuig band se materiale eienskappe vir gebruik in 'n termiese eindige element simulasie prosedure. Eenassige trek toetse is uitgevoer op monsters van 'n band. Die krag verplasingsgedrag van elk is gebruik om materiale eienskappe te bepaal deur middel van direkte kurwe passings en iteratiewe numeriese prosedures. Ekwivalente eindige element simulasie modelle is gebruik om die eienskappe te verifieer. Histerese gedrag van die rubber streke is identifiseer deur dinamiese meganiese analise. Materiale definisies is opgeneem in bestaande eindige element modelle ontwikel deur Maritz (2015) om die bestendige toestande hitte generasie- en temperatuurverspreiding binne in 'n band te voorspel as gevolg van histerese. Die gebruik van materiale eienskappe vanuit die literatuur het gelei tot onakkurate model voorspellings in vergelyking met eksperimentele resultate. 'n Reeks validasie eksperimente en ekwivalente simulasies is uitgevoer om die resulterende strukturele gedrag te evalueer. Die op-gedateerde modelle het akkurate voorspellings voorsien van strukturele vervorming en loopvlak kontak druk verspreiding onder 'n reeks belasting toestande. Eksperimentele rollende band temperatuur metings is geneem op 'n toetsbank. 'n Vergelyking van die resultate met dié vanaf die ekwivalente termiese modelle het merkwaardige ooreenkomste en verbeteringe uitgelig.

Acknowledgements

I would like to express my sincere gratitude to the following people and organisations:

- The Anglo America group for providing funding towards this project.
- Prof. Gerhard Venter and Dr. Martin Venter for their support, guidance and knowledge.
- Melody van Rooyen and Charles F. Jekel Jr. for assistance and guidance with laboratory equipment and software.
- The Department of Mechanical and Mechatronic Engineering staff for the help and assistance with fabrication and testing. In addition; Mr Julian Stanfliet for assistance and guidance with laboratory testing equipment.
- My friends, family, and especially Liesa Brand, for all of the emotional support during the entire project duration. Without you this project would not have been completed.
- The Stellenbosch University Rhasatsha HPC: http//www.sun.ac.za/hpc.

Contents

List of Figures

List of Tables

Nomenclature

Scalar variables

A_m	Curve fit coefficient 1 for Mooney-Rivlin constitutive model
B_m	Curve fit coefficient 2 for Mooney-Rivlin constitutive model
B	Bulk modulus
C_p	Specific heat
C_{10}	Curve fit coefficient 1 for third-order Mooney deformation model
C_{01}	Curve fit coefficient 2 for third-order Mooney deformation model
C_{11}	Curve fit coefficient 3 for third-order Mooney deformation model
C_{20}	Curve fit coefficient 4 for third-order Mooney deformation model
C_{30}	Curve fit coefficient 5 for third-order Mooney deformation model
E	Young's modulus
f	Frequency
G	Shear modulus
G^*	Complex modulus
G'	Storage modulus
$G"$	Loss modulus
$g"$	Dissipation module
H	Hysteresis coefficient
H_c	Forced convection film coefficient
I	Strain invariant

K	Thermal conductivity
$LossU_{sed}$	Loss strain-energy density
p	Hydrostatic pressure
$\dot{q}_v$	Rate of heat generation per unit volume
T_c	Period of rotation
$TotalU_{sed}$	Total strain-energy density
V	Volume
v	Velocity
W	Strain-energy
ΔW	Elemental hysteretic loss per unit volume
ε	Emissivity
$\varepsilon_{1,K}$	Maximum principal value of averaged strain half-amplitudes
θ	Phase angle
λ	Stretch ratio
ν	Poisson's ratio
ω	Excitation frequency
σ	Stress

Matrices

$\boldsymbol{E}$	Material property matrix
$\boldsymbol{k}$	Element stiffness matrix

Subscripts

B	In terms of bulk modulus
E	Experimental (observed)
G	In terms of shear modulus
n	Numerical (predicted)

1	First axis direction
2	Second axis direction
3	Third axis direction

Abbreviations and acronyms

CT	Computed tomography
CSIR	Council for Scientific and Industrial Research
DIC	Digital image correlation
DMA	Dynamic mechanical analysis
DOT	Digital Optimisation Tools
FE	Finite element
HPC	High Performance Computing
IR	Infrared
PLC	Programmable logic controller
RMS	Root mean squared

Chapter 1

Introduction

The background of the thesis project is provided in this chapter, discussing the motivation for undertaking it and the contribution of its research. The overall project goal is then defined, followed by the required objectives for its successful completion.

1.1 Background

Thermo-oxidation is the irreversible chemical and mechanical decomposition of a material due to heat. This occurs inside the rubber regions of a tire when temperatures exceed 185 °C (Vu-Khanh *et al.*, 2008), resulting in the release of volatile gases. Pressure increases within the tire cavity, causing the temperature to rise even further, resulting in a more rapid oxidation rate. A similar process called pyrolysis could also occur with virtually the same signs. The key difference between these two phenomena is that pyrolysis would occur in the absence of oxygen, for example when nitrogen inflation is used.

Heat generation within a tire is unavoidable during normal use owing to the hysteresis of rubber. This refers to the absorption (loss) of deformation energy during cyclic loading. Factors such as rolling resistance and air friction also contribute to energy loss. Hysteresis has however been identified as the major source of energy losses in a tire (Tang *et al.*, 2014), resulting in internal heat generation. The rate of heat generation can be further influenced by external factors such as brake heating, environmental conditions and contact between adjacent tires (Vu-Khanh *et al.*, 2008).

Several overheating cycles will cumulatively degrade the tire structure until failure occurs in the form of a blow-out. In such a case the weakened structure would simply give way under the increased inflation pressure. A more severe mode of failure would occur if the gas temperature and pressure were to exceed its auto-ignition point. For this to occur, the cavity would require a sufficient volume of flammable gas, as well as an oxygen concentration above 5.5 %.

The mixture would self-ignite, causing a violent explosion with pressures waves in excess of 6 MPa. This can result in severe injury or death of a person in close proximity during the time of the explosion. An external source such as lightning or contact with overhead power cables have also been reported to cause ignition (Vu-Khanh *et al.*, 2008).

Worker safety is of utmost importance to the Anglo America Mining group. They have identified pyrolysis and thermo-oxidation within their large-haul truck tires to be the cause of several incidents. Steps were subsequently taken to create a preventative safety procedure, to not only safeguard their employees, but also to avoid loss of machinery and equipment. Tire inflation by means of nitrogen eliminates the risk of thermo-oxidation, whilst a robust method of reducing pyrolysis is still to be identified.

As part of preventative safety Anglo has commissioned three research projects in the form of post-graduate masters' theses at Stellenbosch University. These projects form a combined effort to produce a finite element (FE) analysis simulation model of a full-size haul truck tire. The model would be capable of predicting the rate of heat generation and resulting temperature distributions under a variety of operating conditions. This would enable Anglo to determine a safe working envelope, with regards to load, vehicle speed and internal pressure, to prevent pyrolysis.

The first project, conducted by Maritz (2015), dealt with the generation and validation of a FE thermal tire model. The model considered hysteresis as its primary heat source, whilst including rolling resistance and appropriate heat transfer mechanisms. External heat source anomalies were excluded. The model was based on a 15-inch truck tire, with material properties sourced from published literature. The purpose of the project was to establish a modelling procedure to predict the cross-sectional temperature distributions of a generic tire under a variety of loading conditions. Results were compared to experimental data obtained through testing of an equivalent tire on a tire test bench.

The research presented here deals with experimental identification of material properties for the test bench tire, updating the simulation models and comparing the results with experimental test data. Emphasis falls on establishing and validating methods for obtaining material parameters through simplified testing. Hysteresis is again considered as the primary heat source, requiring the experimental determination of hysteresis coefficients. In addition to the material properties the material structure modelled by Maritz (2015) is redefined to account for the various rubber regions within the actual tire. The original models made use of a single material region throughout the tire cross-section. Execution of this project is a crucial step towards obtaining accurate thermal predictions. The use of material definitions obtained from literature did not provide sufficient consistency with experimental results (Maritz, 2015).

The 3rd and final project, undertaken by Jeannette Marais, entails the application of the findings from the first two projects on a full-sized haul truck tire. It includes material testing, generation of a suitable FE tire mesh and experimental testing. A safe working envelope will be proposed for the particular vehicle from the findings of this project.

The findings of these research projects will assist Anglo in an on-going effort towards preventative safety. The proposed simulation models and testing procedures could be replicated in order to create predictive simulations for any tire used on their premises. Standard operating procedures can then be created for each vehicle to prevent the occurrence of overheating and pyrolysis-related incidents.

1.2 Project goal

To improve the temperature prediction accuracy of a hysteresis-based, finite element tire thermal analysis procedure by experimental determination of material parameters.

1.3 Objectives

In order to successfully complete the project, a list of pre-determined objectives had to be met. Completion of this list, as provided below, would result in the goal of the project being satisfied.

1. Analyse the structural composition and geometry of the modelled tire and its various material regions.

2. Establish the stress-strain response of each material region within the modelled tire by uni-axial tensile testing. All material testing and validation experiments to be executed using an equivalent (215/70R15) Maxtrek SU-830 steel-belted radial tubeless truck tire. Identify appropriate structural material properties for each material within the modelled tire based upon the attained response curves. Validate the stress-strain response of the newly identified material definitions.

3. Identify the hysteresis response of each rubber material region within the modelled tire. Based on the findings, establish appropriate hysteresis coefficient values for use in the simulation models.

4. Update the material properties definitions and hysteresis coefficients within the original simulation models (as created by Maritz (2015)). Include geometric alterations as required.

5. Evaluate the structural deformation response of the updated models against that of an actual tire.

6. Perform validation comparisons of the thermal simulation model results, using experimentally established material parameters, against experimental test data. Compare results to simulation predictions using material parameters originally proposed by Maritz (2015).

Chapter 2

Literature survey

In order to meet the objectives required for the successful completion of the current project, a basic understanding of the numerical modelling of a tires mechanical and thermal response is required. This is provided in the form of a literature study, which is presented in the following chapter. It covers concepts and methods used by the original models (Maritz, 2015), whilst also including works from similarly published literature. The information provided will aid the reader in understanding how the proposed modelling procedure is developed and implemented.

2.1 Rubber

Rubber is an amorphous polymer, consisting on a microscopic level of a network of randomly-orientated long chain molecules with weak intermolecular interactions (Boyce and Arruda, 2000). It is a highly non-linear hyper-elastic material with regards to its force displacement behaviour and is often considered to be fully incompressible. When natural rubber is vulcanised, as found in automotive tires, cross links are formed between its polymer chains (Carwile and Hoge, 1966). This greatly improves the strength and hardness of the material. Hardness and abrasion resistance can be further increased by the addition of filler materials such as carbon black. Depending on the specific application, the ingredients and process used are varied in order to obtain a required material behaviour.

Modelling the behaviour of an elastomer within a FE environment by means of conventional methods is not possible owing to the near incompressibility of the material. Consider the shear- G and bulk B modulus as functions of Young's modulus E and Poisson's ratio ν of a material, as per equations 2.1 and 2.2:

$$G = \frac{E}{2(1+\nu)} \tag{2.1}$$

$$B = \frac{E}{3(1-2\nu)} \tag{2.2}$$

The bulk modulus expresses the ratio of hydrostatic pressure p to volume (V) change (equation 2.3).

$$B = \frac{-p}{\Delta V/V} \tag{2.3}$$

Under the assumption of full incompressibility, the change in volume of a material is null, with a corresponding bulk modulus of infinity. Rearranging equation 2.2, the resulting Poisson's ratio approaches 0.5. When considering the material property matrix $\boldsymbol{E}$ in terms of G and B, as per equation 2.4, the element stiffness matrix $\boldsymbol{k}$ can be expressed by equation 2.5 (Cook *et al.*, 2002).

$$\boldsymbol{E} = G\boldsymbol{E}_G + B\boldsymbol{E}_B \tag{2.4}$$

$$\boldsymbol{k} = G\boldsymbol{k}_G + B\boldsymbol{k}_B \tag{2.5}$$

As ν approaches 0.5, B would dominate the elemental stiffness. Within a FE simulation, this would act as a penalty constraint, effectively locking the mesh (Cook *et al.*, 2002). Though rubber is not fully incompressible, with Poisson's ratios slightly below 0.5, its bulk modulus has been identified to be significantly larger than the shear component.

Adequate numerical continuum mechanics based models exist for the specific purpose of simulating the non-linear and incompressible behaviour of elastomer materials. These types of models are invariant-based treatments of rubber, that effectively model strain-energy response due to deformation (Boyce and Arruda, 2000). Accordingly, a strain-energy function W exists as a function of the strain tensor of the material (Baranowski *et al.*, 2012). The experimentally obtained deformation state of a material can be used to obtain curve-fit coefficients to describe the magnitude of strain energy. Differentiation of the strain-energy function will in turn provide the corresponding stress magnitudes. The most frequently used of these strain-energy-based models is the Mooney-Rivlin constitutive model. It was successfully employed by Baranowski *et al.* (2012) to model the radial forces and deformations in a passenger car tire. The model is a function of experimentally obtained curve-fit coefficients A_m and B_m, as well as the Poisson's ratio as per equations 2.6 through 2.8.

$$W = A_m(I_1 - 3) + B_m(I_2 - 3) + C(\frac{1}{I_3^2} - 1) + D(I_3 - 1)^2 \tag{2.6}$$

$$C = 0.5A_m + B_m \tag{2.7}$$

$$D = \frac{A_m(5\nu - 2) + B_m(11\nu - 5)}{2(1 - 2\nu)} \tag{2.8}$$

The model provides the elastic strain-energy density (J/m^3), i.e. the strain energy per unit volume, due to the deformation of an element. The strain invariants (I_1, I_2 and I_3), which are based on the principal strain magnitudes, are functions of the stretch ratios (λ_1, λ_2 and λ_3) of the material. See equations 2.9 through 2.12, with reference to Figure 2.1. For incompressibility I_3 is equal to 1 (Boyce and Arruda, 2000).

$$I_1 = \lambda_1^2 + \lambda_2^2 + \lambda_3^2 \tag{2.9}$$

$$I_2 = \lambda_1^2\lambda_2^2 + \lambda_2^2\lambda_3^2 + \lambda_3^2\lambda_1^2 \tag{2.10}$$

$$I_3 = \lambda_1^2\lambda_2^2\lambda_3^2 \tag{2.11}$$

$$\lambda_i = \frac{L_i + dL_i}{L_i} \tag{2.12}$$

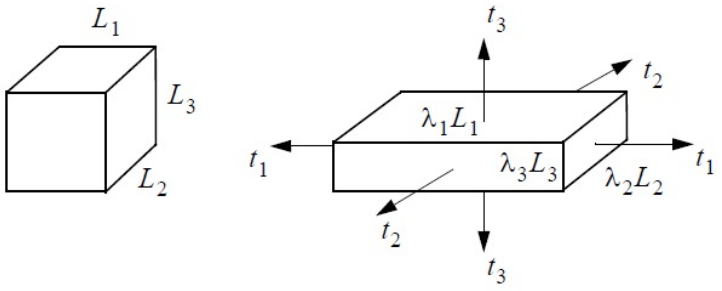

Figure 2.1: Deformation of a simple rectangle element, with t_i representing stress tensors, (Baranowski *et al.*, 2012; MSC, 2010)

The third-order Mooney deformation model (equation 2.13) can be used if higher order fits are required. Care should however be taken in such an event to avoid errors associated with polynomial fits (MSC, 2010). MCS Marc provides integrated functionality for the modelling of this material with the option of reducing its order if required.

$$W = C_{10}(I_1 - 3) + C_{01}(I_2 - 3) + C_{11}(I_1 - 3)(I_2 - 3) + C_{20}(I_1 - 3)^2 + C_{30}(I_1 - 3)^3 \tag{2.13}$$

The third-order Mooney constitutive model can be simplified by zeroing C_{11}, C_{20} and C_{30}, resulting in a two-term (C_{10}, C_{01}) Mooney model which has been shown to be applicable upto strains of 100 % (Conradie, 2014). Tang *et al.* (2014) and Lin and Hwang (2004) successfully simulated the thermal response

of a tire when using it to represent its elastomer components. Kovac and Krmela (2012) suggested its use for simulating tire mechanical behaviour and durability. Their findings suggested the requirement for coefficients obtained through experimentation. For the modelling of vulcanised rubber, the three-term variant has been identified to provide good fits and strain predictions (MSC, 2013). The three-term variant is a result of zeroing C_{20} and C_{30} in Equation 2.13. A study executed by Kumar and Rao (2016) suggested the two-term model to applicable to stress-strain response curves with a single curvature, while the three-term variant should be used in the event of a single inflection point within a particular response curve.

2.2 Characterisation of constitutive models

The constitutive models presented in Section 2.1 are based on empirical observations, rather than first principal derivations based on the physics of the mechanical response of rubber. The characterisation of the Mooney model parameters is achieved by curve-fitting experimental stress-strain response data to the model using FE analysis. The models essentially replicate a measured deformation response of a particular elastomer under load.

Conradie (2014) obtained uni-axial stress-strain response curves for samples originating from the sidewall and tread regions of a passenger car tire. Sample locations and orientations were based on a physical examination of a sample tire, as well as rubber hardness measurements using a Shore D TH210 durometer. Measurement results were used in a relative sense to identify different rubber regions. Uni-axial samples were stretched using an EZ50 tensile test bench, measuring the reaction force with a built-in load cell. Strain response was captured and analysed with stereo-photogrammetry using digital image correlation (DIC).

Global equivalent material properties were then identified for each sample region and modelled as a single elastomer material (Mooney two-term) with reinforcing isotropic rebar elements. This was to reduce computational expenses involved with modelling each individual material region within the tire structure. The use of rebars allowed the stiffness of the model to be adjusted in a specific direction by altering the rebar material's Young's modulus. This was done iteratively by comparing stress-strain behaviour of numerically equivalent tensile test simulations with the experimental data. The sidewall deformation profiles and radial force displacement behaviour of a 3D tire model (MSC Marc), using the identified global material properties, correlated well with experimental results.

Lin and Hwang (2004) followed a similar approach when modelling the heat generation and temperature distribution of a light truck tire due to cyclic loading. The models consisted of simplified elastomer (Mooney two-term), cord ply and bead wire regions as illustrated in Figure 2.2. Uni-axial tensile tests were performed on selected rubber samples, followed by experimental curve fits to obtain elastomer coefficients. Fibre-reinforced composite theory was used to identify the reinforcement angle cord ply parameters.

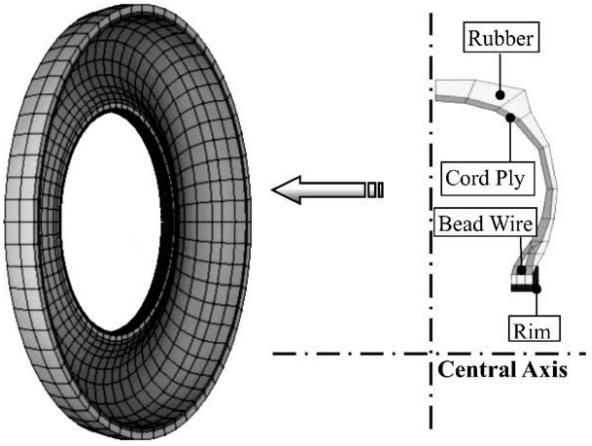

Figure 2.2: Material regions modelled by Lin and Hwang (2004)

Baranowski *et al.* (2012) performed tensile and coupon compression tests on rubber samples from a passenger car tire. Samples conformed to the PN-54/C-04253 and PN-ISO 37:2007 standards, requiring careful preparation to not include any reinforcement cords or wires. The stress-strain data curves obtained during both test procedures can be viewed in Figure 2.3.

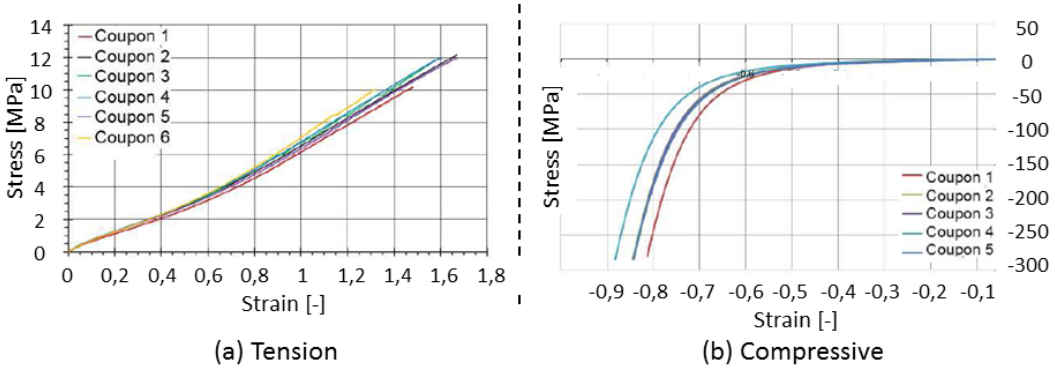

Figure 2.3: Stress-strain data curves obtained by Baranowski *et al.* (2012) for tensile (a) and compressive (b) mechanical response of a passenger car tire.

The reinforcement structure of a sample tire was studied by means of a microscope and X-ray devices. The compression mode of deformation was measured using cylindrical coupons, 17.8 mm long and 35 mm in diameter, and was only obtained from the tread region. Whilst only rectangular tensile samples with a size of 2 by 6 by 40 mm were obtained from the sidewall. An Instron 8802 tensile/compression test machine and high-speed Phanton V12 camera, with Tema 3.3 strain software, was used for testing.

Baranowski *et al.* (2012) proceeded to successfully simulate the radial deflection of a tire by means of an implicit LS-Dyna code obtained from the Michelin tire corporation. The model took into account each individual material region within the tire cross-section, as illustrated in Figure 2.4. Rubber material coefficients (Mooney two-term) were obtained from curve fits using both tensile and compressive modes of deformation as input. Elastic-plastic and orthotropic material definitions of the reinforcement structure was provided by Michelin.

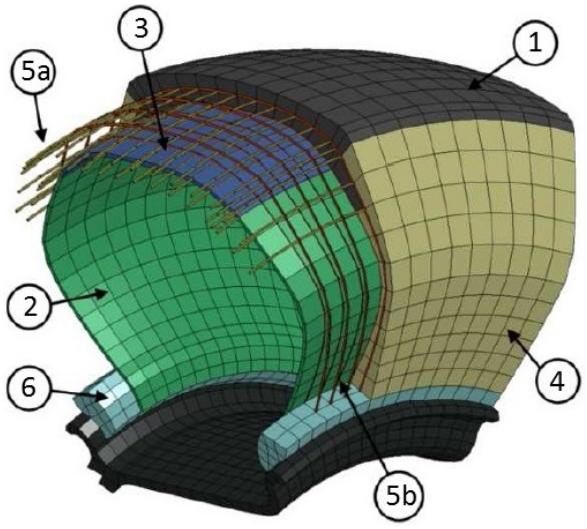

Figure 2.4: Material regions modelled by Baranowski *et al.* (2012), with 1. Tread, 2. Inner fabric, 3. Carcass, 4. Sidewall, 5a, b. Circumferential and radial cords, 6. Bead core with cords.

2.3 Hysteresis heating

When a material that exhibits hysteresis undergoes cyclic loading a fraction of the required elastic deformation energy (elastic strain energy) is absorbed and converted to heat (loss strain energy). This is due to a phase lag that exists between the strain and stress response curves of such a material (Cho *et al.*, 2013). It is the primary heating mechanism within automotive tires, with a contribution of up to 95 % to total energy loss at high rotational velocities

(Tang *et al.*, 2014). The hysteresis behaviour of a material is a function of the applied strain amplitude, excitation frequency and material temperature (Cho *et al.*, 2013). By using the strain-energy-based elastomer models discussed in Section 2.1, it is possible to predict the magnitude of hysteresis heating via FE simulation.

2.4 Hysteresis coefficient

The magnitude of heat dissipation due to hysteresis is described by the material's hysteresis coefficient. It refers to the ratio between loss- and elastic (absorbed and total input) strain energy of a material during cyclic loading deformation. The dynamic viscoelastic properties and deformation of a rubber sample can be characterised by its response to sinusoidal loading (Ebbot *et al.*, 1999; Cho *et al.*, 2013). As such, a complex modulus G^* exists as a function of the materials stress and strain response curves, expressed in terms of a storage $G^{'}$ (in-phase) and loss $G^{"}$ (out of phase) modulus (equation 2.14).

$$G^* = G^{'} + iG^{"} \tag{2.14}$$

$G^{'}$ relates to the elastic strain energy and $G^{"}$ to the loss component of strain energy. Typical results obtained through a dynamic mechanical analysis (DMA) are illustrated by Figure 2.5. The hysteresis coefficient H of the material is calculated as a function of either the complex modulus or the phase angle θ, as per equation 2.15.

$$H = \tan(\theta) = \frac{G_{"}}{G_{'}} \tag{2.15}$$

Lin and Hwang (2004) evaluated the influence of excitation frequency and temperature on the hysteresis behaviour of tire rubber by means of DMA measurements. Hysteresis coefficient values did not show a significant dependence on either the frequency or temperature, with the exception of temperature values below 0 °C. A coefficient value of 0.1 was subsequently chosen for hysteresis loss calculations. Tang *et al.* (2014) and Maritz (2015) used the same value, as sourced from published literature.

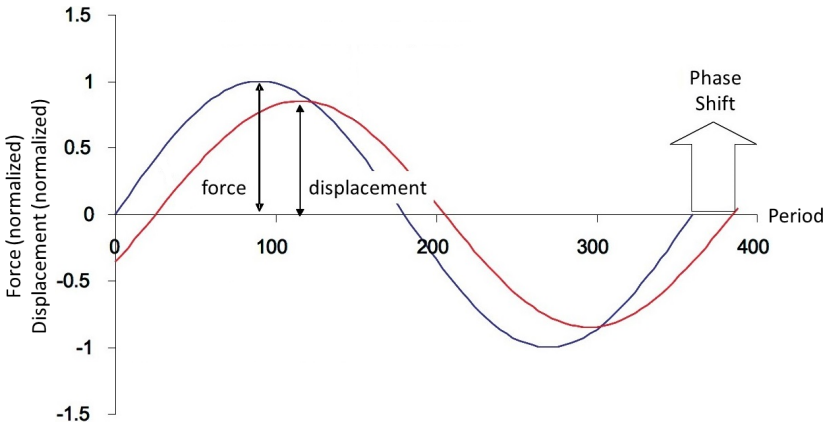

Figure 2.5: Phase lag between loss- and storage modulus observed during DMA experimental testing.

2.5 Heat generation rate

The rate of heat generation within a tire due to hysteresis is a function of the loss strain-energy density, material hysteresis coefficient and rotational frequency. Lin and Hwang (2004), Tang *et al.* (2014) and Maritz (2015) used rolling tire FE simulation models to obtain elastic strain-energy density distributions for a single rotation. Elastic strain-energy density is simply the strain energy per unit volume that is stored within an element due to deformation. The total strain-energy density ($TotalU_{sed}$) is in turn equal to the sum of positive differences in elastic strain energy for the period of deformation. Loss strain-energy density ($LossU_{sed}$) is then calculated on an element basis according to equation 2.16. The rate of heat generation corresponds to the tire deformation rate that is accounted for by its rotational frequency f. The rate of heat generation per unit volume $\dot{q}_v$ (J/m^3) is in turn equal to the product of $LossU_{sed}$ and f (equation 2.17).

$$LossU_{sed} = H \times TotalU_{sed} \tag{2.16}$$

$$\dot{q}_v = LossU_{sed} \times f \tag{2.17}$$

An alternate approach, taken by Cho *et al.* (2013), involved predicting the heat generated due to hysteresis as a function of the dissipation module $g"$ and half-amplitude strains. A dynamic 3D rolling analysis was used to obtain $g"$ and the corresponding strain values for one full tire rotation. The elemental hysteretic loss per unit volume (ΔW) is given by equation 2.18. With $\varepsilon_{1,K}$ being the maximum principal value of averaged strain half-amplitudes $(\Delta\varepsilon_{ij})^c_{K,l}$ (equation 2.19). M_l denotes the Gaussian points along the tires path of rotation.

$$\Delta W = \pi g \varepsilon_{1,K}^2 \tag{2.18}$$

$$(\Delta e_{ij})_K^C = \sum_{l=1}^{M_l} (\Delta \varepsilon_{ij})_{K,l}^c / M_l \tag{2.19}$$

The rate of heat generation $\dot{Q}$ (J/m^3) is then calculated by equation 2.20 for each element. T_c denotes the period of rotation (equation 2.21), with ω being the excitation or rotational frequency. Cho *et al.* (2013) went on to include hysteresis due to rolling resistance, comparing the resulting temperature distributions from different tread pattern shapes.

$$\dot{Q} = \frac{\Delta W}{T_c} \tag{2.20}$$

$$T_c = \frac{2\pi}{\omega} \tag{2.21}$$

2.6 Heat transfer mechanisms

Temperature distributions within a tire resulting from hysteresis heating were evaluated via steady-state thermal analyses by Cho *et al.* (2013), Maritz (2015), Lin and Hwang (2004) and Tang *et al.* (2014). Thermal material properties were assumed to be temperature-independent in all four cases. The rate of heat generation, as obtained from the tyre deformation models, was applied to individual rubber elements in the form of thermal volume flux. Conduction between adjacent elements and thermal boundary conditions allow the heat to dissipate until thermal equilibrium is reached. Proper inclusion of these heat transfer mechanisms is crucial in obtaining accurate and reliable temperature predictions.

Cho *et al.* (2013) included the influence of convection, conduction and radiation boundary conditions to the tread, sidewall and inner tire cavity as illustrated in Figure 2.6. Convection at the tread base and inner surface is relative to cavity air, whilst radiation effects are included at the lower sidewall region. The convection coefficient is constant for the tread pattern region, whilst varying linearly for the sidewall as a function of the distance to the central tire axis. Radiation emitted from the tread pattern and upper sidewall was simulated with an emissivity value of 0.95, as to nearly represent the radiation emitted from blackbody. Conduction was also added between the tire bead and rim surface.

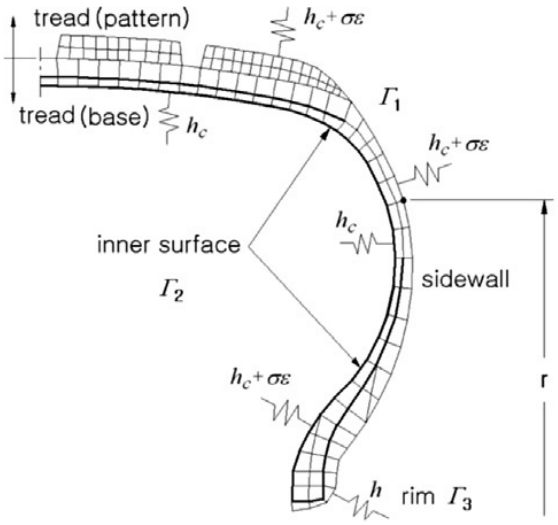

Figure 2.6: Thermal boundary conditions employed during a thermal tire simulation done by Cho *et al.* (2013). With h_c - convection, $\sigma\varepsilon$ - radiation and h - conduction.

Browne and Wickliffe (1980) established an empirical equation for a forced convection film coefficient H_c (W/m^2°C) at the outer tread and sidewall surfaces of an automotive truck tire. It is a function of the average relative air velocity (v) flowing past the wheel during a single rotation, as given by equation 2.22. This method of convection heat transfer was reported to have a dominating effect relative to the outside environment of a vehicle tire during rotation. Ebbot *et al.* (1999) performed similar measurements on a P175/70R13 passenger car tire, obtaining results that validated the findings proposed by Browne and Wickliffe (1980). It entailed the use of an inverse numerical procedure using experimental test data. Assaad *et al.* (2008) designed, built and tested a small flexible sensor to determine the convection heat transfer film coefficient at the tread surface of an automobile tire. The sensor measures changes in electrical resistances within a small resistor bridge to determine surface temperatures and transient heat flux magnitudes. Film coefficient values obtained from a P225/55R15 passenger tire were in accordance with the findings of both Browne and Wickliffe (1980) and Ebbot *et al.* (1999) for a constant velocity of 22 m/s.

$$H_c = 5.9 + 3.7v \tag{2.22}$$

Lin and Hwang (2004), Tang *et al.* (2014) and Maritz (2015) used the coefficient equation proposed by Browne and Wickliffe (1980) and Ebbot *et al.* (1999) for convection heat transfer boundary conditions at the external tread and sidewall surfaces. Lin and Hwang (2004) used an insulated internal cavity

surface, whilst Tang *et al.* (2014) and Maritz (2015) accounted for the influence of the internal air cavity by modelling it as a natural convection boundary condition. For this the velocity component in equation 2.22 was assumed to be negligible. In addition, Tang *et al.* (2014) included conduction relative to the rim and road surfaces.

2.7 Conclusion

This chapter provided a literature-based overview of key aspects involved with the finite element thermal modelling of an automobile tire under steady-state rolling conditions. It covered the appropriate use and identification of elastomer material models, modelling the occurrence of hysteresis heat generation and the use of thermal-boundary conditions. This information served as the foundation for the project with regards to the identification of material parameters (Chapter 3 & Chapter 4) and alterations to the original simulation models (Chapter 5).

The non-linear stress-strain relationship of vulcanised rubber found in automotive tires can be represented appropriately by either the two- or three-term variants of the third-order Mooney-Rivlin constitutive model. Its coefficients can be obtained directly by means of experimental curve fits using the tensile- or compression-based stress-strain response of a particular sample. These material models would allow a simulation to appropriately predict the total (elastic) strain energy resulting from deformation, as required in the hysteresis heating calculations. In order to obtain accurate thermal heat flux magnitudes, the hysteresis coefficient value of each rubber region should be determined.

Conduction, convection and radiation boundary conditions should all be included with respect to the inner cavity, outside environment and adjacent elements. The major source of heat loss will, however, be due to forced convection at the sidewall and tread surfaces relative to the air flowing past the wheel. This film coefficient value can be calculated as a function of the average relative air velocity during a single rotation. Convection relative to the internal cavity can be included by setting the velocity component equal to zero, whilst also including the influence of radiation. Conduction relative to adjacent elements must be included, whilst its influence relative to the rim is negligible. A detailed account of the model's thermal attributes is provided in Section 5.4.

Chapter 3

Material characterisation

Uni-axial tensile tests were performed on samples obtained from a 215/70R15 Maxtrek SU-830 steel-belted radial tubeless truck tire. This was to attain the force displacement behaviour of each of its constituent materials and/or regions as per Table 3.1. The corresponding stress-strain relations were then later used to identify suitable material model definitions, utilising variants of the Mooney deformation models (Section 2.1). The testing procedure is discussed in the following chapter, following from an analysis of the tire structure and material composition. Details of specialized equipment used during testing and sample preparation steps are also included.

3.1 Region identification by hardness

The international standard instrument for measuring hardness of elastomer type materials is a durometer. Measurements are based on the penetration depth of an indenter tip into the surface of a sample. A Shore D hand-held durometer was used for measurements across the cross-section of the tire in 12.5 mm increments. The accuracy of the unit is equal to 0.5 HD, with a scale ranging from 0 to 100 HD. The results were then used in a relative sense to identify the different major material regions within the tire. This is illustrated by Table 3.1, with Figure 3.1 providing a graphic illustration of the various regions.

Table 3.1: Durometer cross sectional hardness.

	Region	Shore D
1	Bead	23 - 26
2	Apex	15 - 17
3	Sidewall	11 - 14
4	Tread	23 - 25

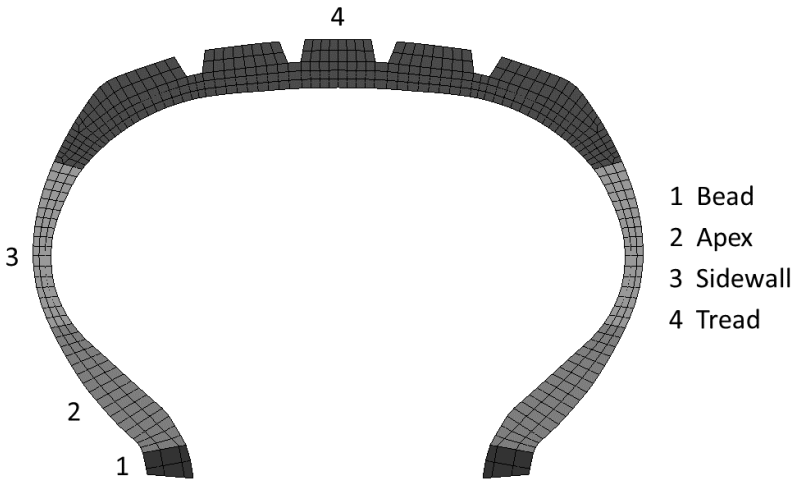

Figure 3.1: Tire elastomer regions.

3.2 Computed tomography

The steel reinforcement structure within the tread region of the tire was examined by means of a computed tomography scan at CT Scanner Facility at Stellenbosch University (du Plessis *et al.*, 2016). A direct tube micro-CT system was used, set to a resolution of 0.01 mm, with a typical voxel (or pixel volume) dimension of 0.09 mm. A cross-sectional sample of the tread was scanned and subsequently analysed, as shown in Figure 3.2. The scans revealed two adjacent layers of steel rebar, at positive and negative 30° angles relative to the tire circumference. Each layer consisted of multiple parallel steel cables, with four wound steel wires making up each cable. Measurements of the wire diameter (gauge) were made with a digital Vernier calliper and mechanical micrometer, as advised by ASTM D4975 - 04(2011). A summary of the rebar structure is provided in Table 3.2.

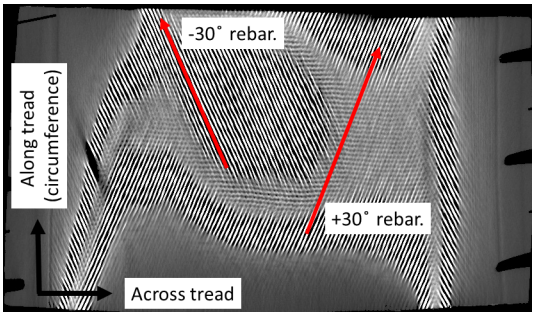

Figure 3.2: CT scan image of tire tread, illustrating two adjacent layers steel rebar wire at ±30°.

Table 3.2: Geometrical parameters of steel rebar.

Parameter	Value
Number of rebars per unit length	675/m
Rebar area	2.29 e-007 m^2
Angle relative to circumference	$\pm$ 30°
Layers	2

3.3 Cross-sectional observation

Along with the information obtained from the CT scans and durometer measurements it was possible to classify the physical composition of the tire. Additional observations on its structure were made by performing an autopsy on a cross-sectional tire sample. These steps were crucial in the analysis, as no information could be obtained from the manufacturer. The bead of the tire consisted of a solid and highly ridged steel cable encapsulated within the rubber of the lower apex region. The apex in turn consisted of a tough apex rubber elastomer, with two layers of softer sidewall rubber on both sides. A layer of radially-orientated cord ply rebar, located between the rubber regions on both sides, supplied additional stiffness in the radial direction. The sidewall region consisted of a uniform sidewall rubber with two radial cord rebar layers that extended from the apex. The cord reinforcements run across the entire cross-section of the tire. The internal structural lay-up of the apex, sidewall and tread regions are illustrated in Figure 3.3.

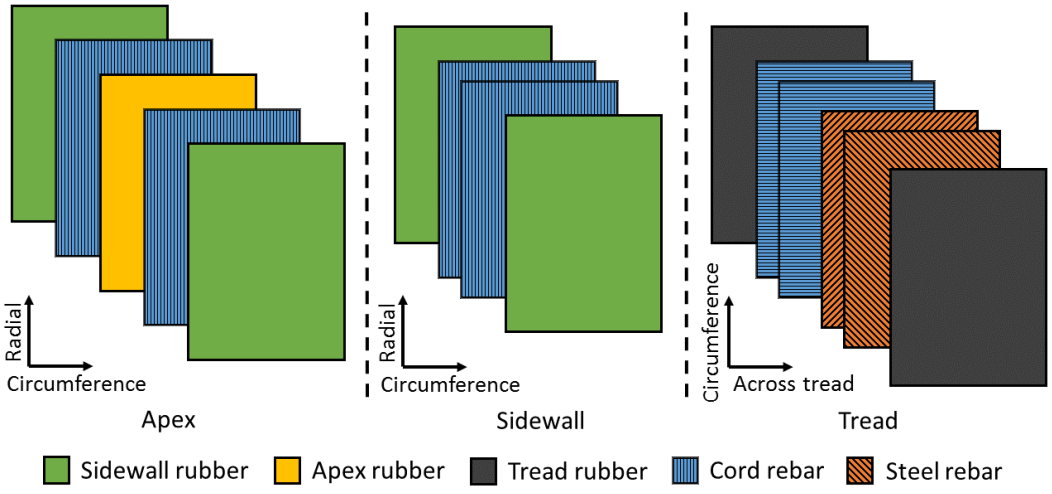

Figure 3.3: Illustration of tire structural regions.

The tread region consisted of a hard rubber material, with two layers of angled steel rebar layers. They were orientated at plus and minus 30° relative to the circumference of the tire, with specifications as given in Section 3.2. It should be noted that none of the rebar reinforcement layers were in direct contact with one another, with thin regions of rubber separating them.

3.4 Sample selection

The complex structure, geometry and composition of the tire made it difficult to perform uni-axial tensile tests on each of its individual materials. Samples were therefore chosen in a manner that would either provide individual material response, or that of an entire tire region. In the second case, the response is a combination of the individual responses of the materials that constitute that region. Such samples were selected as to have only one unknown material, with the second and/or third constitutive materials being already identified (through uniform material sample response). The stress-strain contribution of the unknown material could then be identified as the difference between that of the combined (experimental) and known material responses. This required iterative numerical procedures and equivalent tensile simulation models, using initial estimates of the initially unknown material, as discussed later in Section 4.3.1. Particulars of each tensile sample is provided in Table 3.3, with reference to Figure 3.4 and 3.5

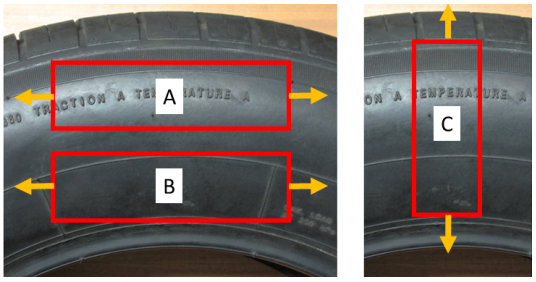

Figure 3.4: Tensile test sample locations within tire sidewall: (A) Sidewall circumferential, (B) Apex circumferential and (C) Sidewall radial. Tensile force directions identified by yellow arrows.

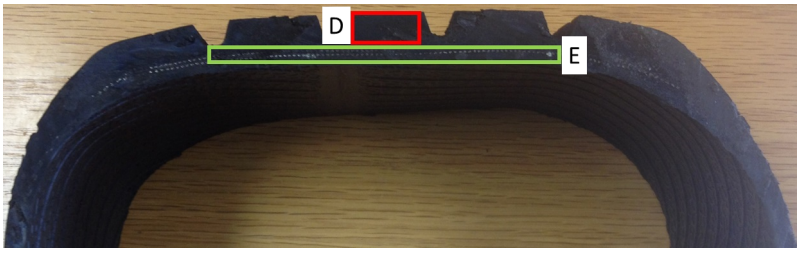

Figure 3.5: Steel rebar (green) and tread rubber (red) locations within tire cross section. Tensile force applied in-plane for tread rubber and longitudinally for rebar samples.

Table 3.3: Tensile sample selection and methodology.

Region	Test approach	Model fit approach	Material characterised
A. Sidewall circ.	Region as a whole	Non-linear elastic (direct)	Sidewall rubber (cord reinforcement assumed neglectable in this direction)
C. Sidewall rad.	Region as a whole	Non-linear elastic (Extract sidewall rubber from A to determine)	Radial cord-ply
B. Apex circ.	Region as a whole	Non-linear elastic (Extract sidewall rubber from A to determine)	Apex rubber
D. Tread	Rubber only (circumferential tire direction)	Non-linear elastic	Tread rubber
E. Steel rebar	Single wire of 4-wire cable, axial load)	Linear elastic (steel)	4-wire strand, as single strand with equivalent diameter.

The tire bead wire was not evaluated during testing due to its rigidity and stiffness. The bead region remained fully in contact with the seat of the rim during preliminary deformation tests of the tire on the test bench. Its movement and rotation was negligible relative to the deformation of the apex, sidewall and tread regions. It was modelled as a simplified solid isotropic steel member, with a Young's Modulus of 207 GPa and Poisson's Ratio of 0.3.

3.5 Sample extraction and preparation

Samples from the regions identified in Figure 3.4 were cut by waterjet. Tread rubber and steel rebar samples were however removed by hand, (as illustrated in Figure 3.5) as they were too small for waterjet cutting. A Metex M-3850D multimeter with specifications as per Table B.1, set to continuity, was used to identify corresponding steel rebar ends within a section of tire tread. A scalpel was then used to carefully fillet samples from it, taking care to avoid damage. Acetone was used to remove excess rubber by soaking, scrubbing and rubbing of samples. Tread rubber strips were obtained in a similar manner using the scalpel.

Sample geometry was dictated by the size of the MTS clamps (Section 3.6.2) and DIC (Section 3.6.1) calibration plate. Lengths were selected to accommodate the entire clamp length at both ends, whilst also providing space for the DIC calibration plate. The number of samples obtained and their respective geometries are provided in Table 3.4. Use of the LaVision DIC required the application of a high contrast speckle pattern. Spray paint was used to apply an even pattern layer onto the exposed surfaces of each sample, as illustrated in Figure 3.6. Combinations of white, grey, bronze and black were used in order to obtain a high-contrast and even distribution of speckles. Steel rebar samples were not treated due to their lack of sufficient surface area. Their deformations were to be measured directly by the extensometer.

Table 3.4: Dimensions of uni-axial tensile samples in mm.

	Length	Width	Thickness	No.
Apex circumferential	165	25	15	4
Sidewall circumferential	165	25	6	4
Sidewall radial	115	25	6	7
Steel rebar	150	θ=0.54	-	7
Tread rubber	150	9	7	3

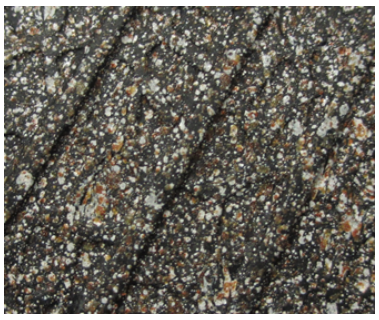

Figure 3.6: Typical high-contrast DIC speckle pattern.

3.6 Material characterisation by tensile testing

Tensile tests were performed using a MTS uni-axial test bench and LaVision stereoscopic Digital Image Correlation (DIC) equipment. The systems were interlinked, with real-time reaction force measurements from the MTS load cell being fed to the DIC analogue to digital converter unit, with specifications as per Table B.3. This enabled seamless force displacement post-processing using the accompanying DaVis software.

3.6.1 DIC

Digital image correlation (DIC) is a non-contact optical method for analysing surface displacement fields of a deformed specimen (Hild and Roux, 2006). A sequence of consecutive images are discretised into subsets of $N \times N$ pixels, which are then tracked by a post-processing algorithm. Individual pixel locations are based on a high-contrasting speckle pattern applied to the specimen surface. From this a deformation vector field is obtained, based on an initial undeformed state, followed by strain fields of the deformed surface.

A LaVision StrainMaster 2D/3D DIC unit and accommodating DaVis post-processing software was used to obtain strain responses of samples during uni-axial testing. Specifications of the system can be viewed in Table B.2. The particular DIC was a 3D stereoscopic system with two digital cameras allowing for the calculation of in-plane and out-of-plane displacements. Refer to Figure 3.7 for an illustration of its typical setup and use during tensile testing, with Figure A.1 providing an additional view. An external extensometer was used as a validating tool. The device clamps onto a sample by means of built-in grips, providing a mechanical measurement resolution of twenty-five mm.

3.6.2 MTS test bench

Tensile tests were conducted on a MTS Criterion Model 44 uni-axial tensile test bench, as shown in Figure 3.7, controlled by default TestWorks software. Samples were held in place by two mechanical jaw clamps, one located on either the top or bottom of the main structure and the second being attached to the horizontal crosshead. Specifications of the unit can be viewed in Table B.4.

The reaction load of a sample was recorded by a high-accuracy load cell located between the stationary clamp and main structure. During the execution of the project either a 1 kN (low-load) or a 30 kN (high-load) high-accuracy load cell was used, depending on the stiffness of a particular sample. The load-cells feature Transducer Electronic Data Sheets that allowed for automatic identification and calibration by the Criterion system.

3.6.3 Setup

A prepared sample was carefully located between the MTS clamps, applying sufficient force to minimise slippage. Excessive clamping would however result in premature failure at the clamp edges. Whilst avoiding pre-tensioning, the sample was straightened by adjusting the clamp locations. With the DIC apparatus set up and calibrated, as described in Appendix A.1, the test commenced as shown in Figure 3.7.

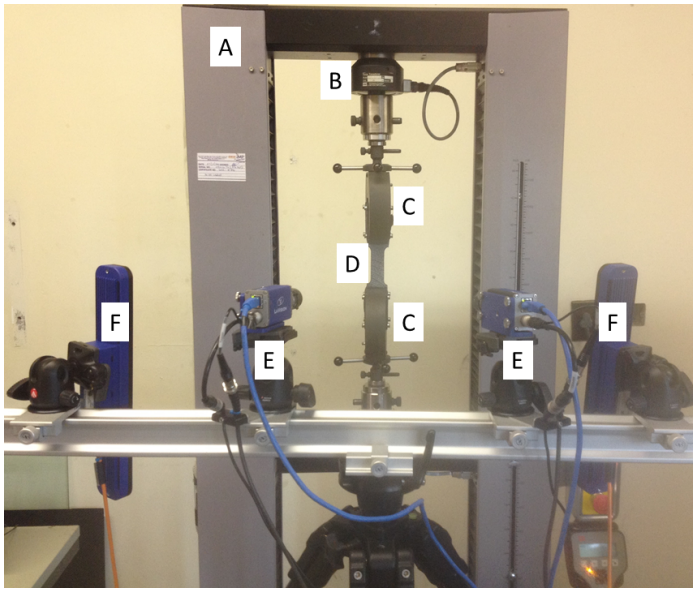

Figure 3.7: Uni-axial tensile test setup utilizing both DIC and MTS equipment. Component list: A - MTS test bench, B - MTS load cell, C - MTS clamps, D - sample, E - DIC camera and F - DIC flash. (LaVision DAC not shown).

3.6.4 Test execution

Displacement control was used to move the MTS crosshead down at a constant rate, stretching the sample located between its clamps, while simultaneously recording the load cell measurement. During this time the DIC continuously recorded the deformation of the speckle region at a constant frame rate. This process continued up until the point of structural sample failure, in which case the sample was either torn or the internal reinforcement structure broke. A discontinuity in the measured reaction force occurred in such a situation. Significant clamp slippage also signalled the end of a test.

A rate of 100 mm/min was used for all samples, with the exception of the steel rebar. For such samples the ASTM standard D4975-04(2011) specified a rate of 25 mm/min for a gauge length of 250 mm, or 10 %. The maximum attainable sample length from the tire was equal to 150 mm. A gauge length of 75 mm was subsequently selected, with a corresponding extension rate of 7.5 mm/min. An extension rate of 500 mm/min was originally used for the tread rubber samples, as specified by ASTM standard D412-15a. It was thereafter reduced to 100 mm/min in order to attain more sensible force displacement results, as the original rate was deemed excessive in conjunction with the available sample lengths.

3.6.5 Processing

Following a test, the recorded raw data was first processed within the DaVis software environment. Strain deformation fields were obtained by following the steps presented in Appendix A.2. Virtual strain gauges were used to obtain the strain behaviour within a particular region and direction of interest. Along with the imported reaction force values it was then possible to export the obtained stress-strain data as text files by means of the DaVis software. Engineering stress and strain values were selected, as required by MSC Marc, for elastomer data fitments (MSC, 2010). The curve fitting procedure only requires the stress-strain data for a particular loadcase.

3.7 Conclusion

Details of a uni-axial tensile testing procedure of samples obtained from a tire were discussed in this chapter. This included the steps followed while obtaining suitable samples, a description of the equipment used and the test procedure itself. Stress-strain data obtained from each sample was used to identify material parameters for use in the FE simulation models, the details of which are provided in the subsequent chapters of this report.

Chapter 4

Characterisation of material models

Data obtained during tensile testing served as the foundation for both direct material fits and iterative procedures. The resulting material properties were validated by numerically equivalent tensile test simulations of combined material samples, attempting to replicate the measured stress-strain response curves. Hysteresis coefficient behaviour of the tire elastomer (rubber) regions (Section 3.3), as a function of cyclic load frequency and temperature, is also discussed. An overview of suitable thermal material coefficients is also included.

4.1 Strain range alterations

Material coefficients that are obtained through direct or indirect stress-strain curve fits are dependent on the particular range of values used. The behaviour of the resulting material will only be able to predict material stress-strain response within the scope of the fitted curve. Predicted material behaviour beyond the scope can be misleading as it is not based on a measured response (MSC, 2010). The experimental stress-strain range, onto which the material models are to be fitted, must be within that of the intended simulation's range. Use of an extensively wide strain range could result in a poor resolution. Behaviour of interest within the first 5 % of an experimental data curve can likely be overlooked, i.e. simplified as a straight line, when applying a curve fit to the entire range.

The loading tire analysis (Section 5.3.2) models created by Maritz (2015) were used to identify the maximum ranges of strain present within each elastomer material region under a variety of operating conditions. The experimental stress-strain data curve ranges were subsequently altered, allowing for a 10 % excess in each case.

This was done in an iterative manner throughout the process of identifying the parameters of each material. Originally the engineering strains of all three elastomer data curves were in excess of 50 %. The altered strain ranges, as used for the subsequent material coefficient identifications presented in this chapter, are shown in Table 4.1.

Table 4.1: Altered experimental strain ranges of elastomer material data curves, as to provide best possible fits within the strain ranges of interest.

	Strain %
Apex rubber	9
Tread rubber	34
Sidewall rubber	9.5

4.2 Direct experimental data fit

It was possible to establish material properties directly from tensile test data for samples comprising of only one material. The stress-strain behaviour of the sidewall and tread rubber was defined by the hyper-elastic Mooney Rivlin material model (Section 2.1). The linear stress-strain relationship of the steel rebar was modelled as an isotropic material, with properties identified directly from tensile test data and published literature.

4.2.1 Elastomers: tread and sidewall

Mooney Rivlin material coefficients were obtained for the sidewall and tread rubber by means of the experimental data fit tool within MSC Marc. It executed a time-independent fit of the material equation onto a given stress-strain data curve. The least squares error relative to the experimental curve was automatically minimised by adjustment of the coefficient values. By using the resulting coefficients it was possible to replicate the measured material response. The resulting fits are illustrated in Figures 4.1 and 4.2 for the sidewall and tread rubber, respectively.

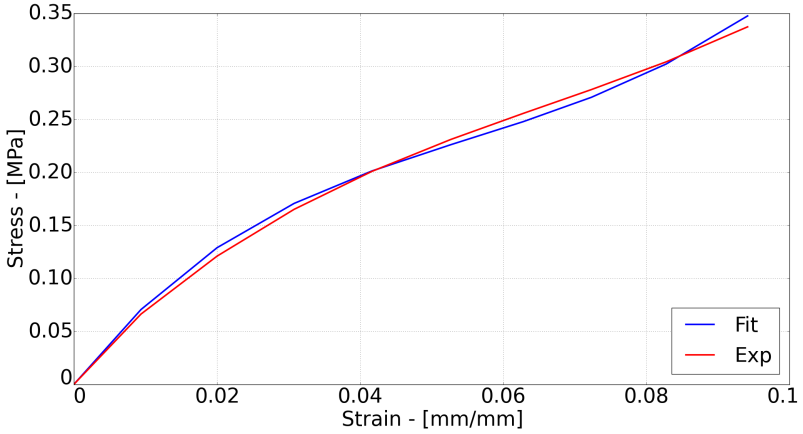

Figure 4.1: Sidewall rubber Mooney Rivlin 3-term data fit. Based on sidewall circumferential tensile test data.

The three-term variant of the third-order Mooney deformation model was selected for the sidewall, whilst its two-term equivalent was used for the tread. In each case the selected Mooney variant provided the best representation (fit) of the experimental test data. The corresponding coefficients, bulk moduli and fit errors are given in Table 4.2. The error magnitudes provided are the root mean square (RMS) values between the numerically fitted (predicted stress σ_N) and experimental (observed stress σ_E) data curves, as per equation 4.1. It is based on the stress magnitude differences at corresponding strain values, utilising a fourth-order polynomial fitted to the experimental data. This allows the stress differences to be calculated at identical strain values, as per the numerical results for a total number of data points n. All RMS error values provided in the subsequent Chapters of the report were calculated in the same manner.

$$RMSError = \sqrt{\frac{\sum_{i=1}^{n}(\sigma_N - \sigma_E)^2}{n}} \tag{4.1}$$

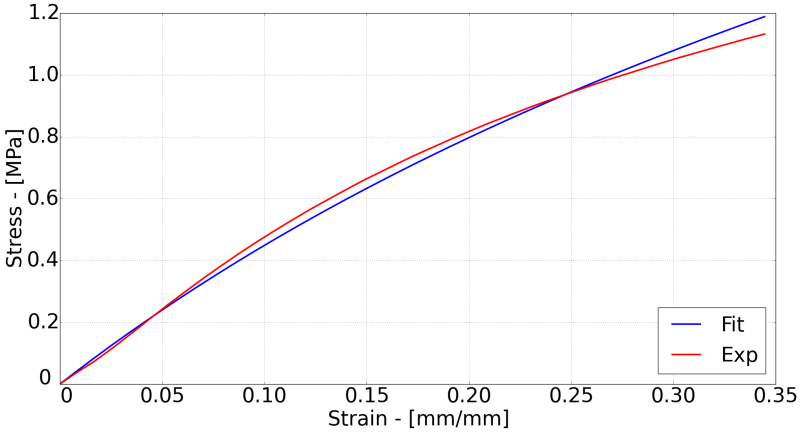

Figure 4.2: Tread rubber Mooney Rivlin 2-term data fit. Based on tread rubber tensile test data.

Table 4.2: Mooney Rivlin material coefficients obtained from direct experimental curve fits using MSC Marc software.

	Sidewall	Tread
C_{10}	-1.87597e+007	440161
C_{01}	2.02023e+007	417869
C_{11}	2.07861e+007	-
Bulk moduli	1.44262e+010	8.5803e+009
RMS error	0.0065	0.024

The obtained Mooney Rivlin material coefficient values were subject to a set of restrictions, as to provide stable solutions (Kumar and Rao, 2016). Stability in this context refers to a positive increase in material strain resulting in a positive stress response. In other words, the material models can not simulate a reduction in stress due to increased strain magnitudes. The criteria for both two- and three-term models, to which the coefficient values of Table 4.2 conformed, can be viewed in equations 4.2 and 4.3 respectively.

$$C_{10} + C_{01} \geq 0 \;\&\; C_{01} \geq 0 \tag{4.2}$$

$$C_{10} + C_{01} \geq 0 \;\&\; C_{11} \geq 0 \tag{4.3}$$

4.2.2 Steel rebar

Uni-axial steel rebar stress-strain curves obtained during testing can be viewed in Figure 4.3, with each of the multiple lines being the response of an individual sample. Sample failure indicated the end of a test in each case. The average of these curves was used to calculate the materials Young's moduli, being equal to the gradient, whilst a Poisson's ratio was sourced from published literature (Tang *et al.* (2014) and Lin and Hwang (2004)). These properties can be seen in Table 4.3, whilst the geometric parameters were as per Table 3.2.

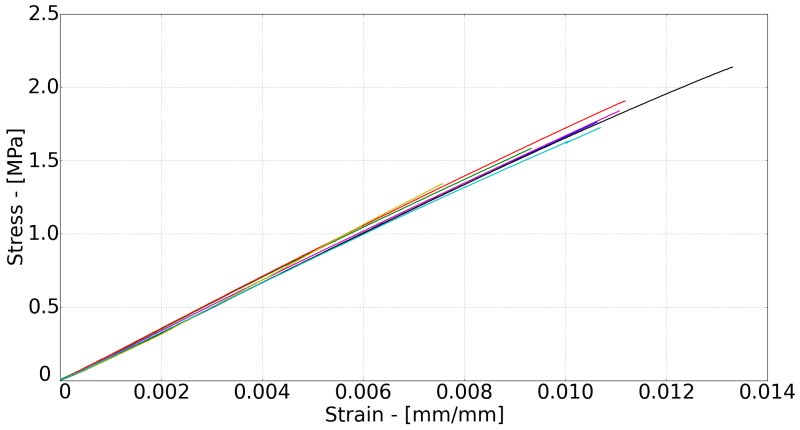

Figure 4.3: Stress-strain response curves of steel rebar samples.

Table 4.3: Isotropic steel rebar properties

Steel rebar	
Young's moduli	170.4 GPa
Poisson's ratio	0.3

4.3 Iterative method

The apex rubber and radial cord rebar material parameters were established through an inverse iterative approach. This was based on the combined material stress-strain response of the apex circumferential and sidewall radial tensile samples in each case (Section 3.4). Each sample consisted of the already established (direct curvefit) sidewall rubber material (Section 4.2.1) and the unknown material in each case. The contribution of the unknown material to the samples stress-strain response could then be identified as the difference between that of the combined material and known material (sidewall rubber) contributions, as illustrated in Figure 4.4.

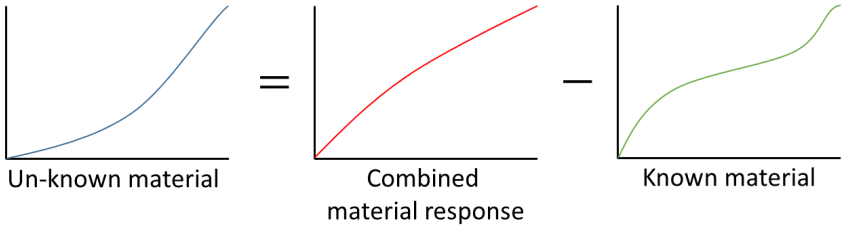

Figure 4.4: Illustration of unknown materials stress-strain contribution to the combined material tensile sample response.

A numerically equivalent tensile test simulation model was subsequently created of each combined material sample within MSC Marc, using an initial estimate of the unknown material parameters in each case. Details of the simulation models, as well as the results of a mesh refinement study, are provided in Sections 4.3.2 and 4.3.3. An optimisation software package Digital Optimisation Tools (DOT), discussed in detail within Section 4.3.1, was then used to evaluate the RMS error, as per equation 4.1, between the combined material experimental and numerical stress-strain response curves. The error calculation was based upon the stress differences at corresponding strain increments, utilising a third-order polynomial fitted to the experimental stress-strain data. This allowed the differences to be evaluated at identical strain increments, as per the numerical (predicted) results.

Based on a set of predetermined convergence criterion and side constraints, the unknown coefficients were then optimised by DOT and substituted back into the simulation model. The purpose and goal of this process was to minimise the RMS error (objective function) between the predicted and observed response curves. This procedure was executed several times by means of a Python script file until the maximum number of iterations (default 100) had been reached, no feasible solutions were found or the point of diminishing returns had been reached. The last situation was most common, with the objective function reaching a plateau within the assigned variable range, which was limited by the Mooney Rivlin stability criterion (equations 4.2 and 4.3) in this case. Using the defined material model definitions the best possible solution is found. In the event of non-satisfactory results, the initial conditions, variable ranges and search criteria were altered and the process repeated.

A graphical illustration of the process is provided in Figure 4.5. Successful completion of the procedure resulted in a set of suitable material parameters to describe the originally unknown material, as discussed in Section 4.3.4 and 4.3.5.

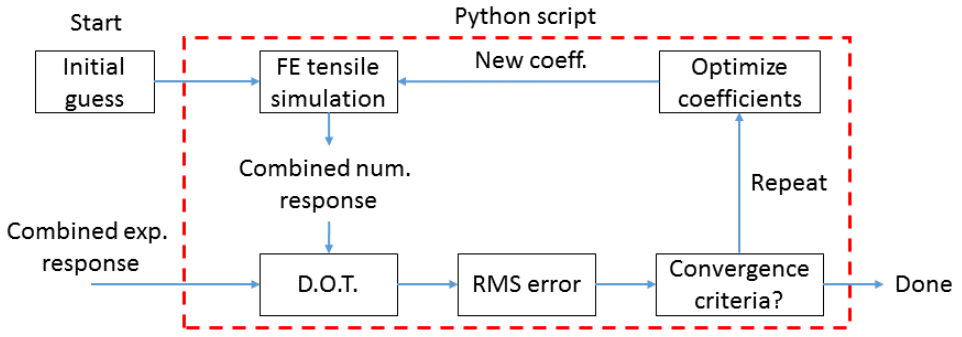

Figure 4.5: Illustration of the iterative numerical procedure used to obtain apex rubber and sidewall cord rebar material parameters.

Convergence to a solution for both materials required large computational resources due to the highly non-linear stress-strain responses of the elastomer (rubber) materials. Both processes were subsequently submitted to the Rhasatsha High Performance Computing (HPC) system at Stellenbosch University. The use of the HPC system's powerful parallel computational capabilities made it possible to attain convergence within six days for the non-linear hyper-elastic apex rubber and 1 for the cord rebar material.

4.3.1 Optimisation software

Digital Optimisation Tools (DOT) is a software package developed by Vanderplaats Research and Development Inc. intended for the assistance in solving constrained and unconstrained numerical optimisation problems. It is a multipurpose software library employing well-established gradient-based numerical optimisation methods to maximise or minimise an objective function of interest (VR&D, 2001). It does so by adjusting a set of design variables subject to a selection of inequality and/or side constraints specified by a particular application. Initial estimated values of the design variables need to be provided, in conjunction with upper and lower limits for each.

It was employed in the present study within an iterative procedure to optimise a set of material parameters based on combined material stress-strain response (Section 4.3). The objective function to be minimised was the RMS error between the predicted and observed response curves, with the design variables being the originally unknown material parameters. A summary of the software (DOT) settings used for the optimisation procedure is provided in Table 4.4. The definition of stable material coefficients refers to equations 4.2 and 4.3, with regards to the Mooney Rivlin material models.

Table 4.4: Settings used for DOT during iterative procedures.

Parameter	Setting
Objective function	RMS stress-strain curves
Type	Unconstrained minimisation
Search method	Broydon-Fletcher-Goldfarb-Shanno (BFGS) variable metric
Variables	Material coefficients
Side constraints	Stable material coefficients

4.3.2 Numerical tensile test models

Equivalent combined material simulation models of the apex circumferential and sidewall radial tensile tests were created within MSC Marc. Both simulations models were solved using an adaptive multi-criteria stepping procedure. They employ the full Newton Raphson iterative procedure with a maximum of 180 recycles. A relative residuals force tolerance was used for convergence testing. An appropriate element size was established by means of a mesh convergence study, as described in Section 4.3.3. The rubber regions were modelled by three-dimensional arbitrary distorted brick elements (type 84), whilst four-node rebar membrane elements were used to represent the cords within the sidewall. The rebars were embedded within the host elastomer regions by means of the insert function of the software. The apex simulation model consisted of 13 500 elements, while the sidewall model contained a total of 8 600 individual elements.

Excessive bulging was observed during the clamping of the sidewall radial samples during testing, requiring a pre-load to be applied in order to straighten the specimen. The sidewall structure is non-symmetric through its thickness, with an excess of soft sidewall rubber on one side. This resulted in the non-uniform sample protruding (or squeezing) from the grip edges. The required clamp displacement and resulting pre-load values, being equal to 2 mm and 225 N, were recorded on the MTS during testing and subsequently included in the numerical modelling procedure. This was done in order to ensure consistency between the numerical simulation model and the tested samples. Displacement control boundary conditions were used, as shown in Figure 4.6. An additional set of displacement control boundary conditions were then used to apply the required strain to the model. Stress-strain behaviour during the pre-load phase was neglected to correspond with the experimental results.

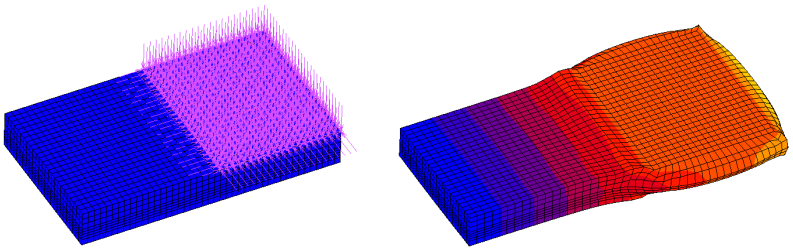

Figure 4.6: Sidewall radial tensile test simulation, showing both the original (left) and deformed (right) shapes.

The apex circumferential simulation model can be viewed in Figure 4.7. All the degrees of freedom at one end were fixed, whilst tension was applied at the opposing end by means of displacement control. At the displaced end all the remaining degrees of freedom were also fixed.

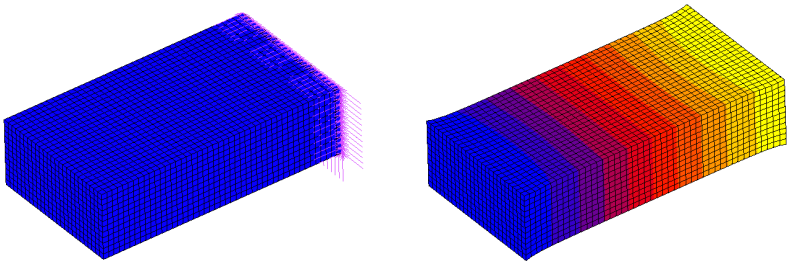

Figure 4.7: Apex circumferential tensile test simulation, showing both the original (left) and deformed (right) shapes.

4.3.3 Mesh convergence study

A mesh convergence study was conducted on a preliminary apex circumferential tensile simulation model. The influence of element size on the dynamic behaviour of the model was of interest. The goal was to identify a suitable level of mesh refinement at which additional element size reduction would have negligible influence on the force displacement response. Several refinements of an original mesh were subsequently made, with Figure 4.8 showing the original (198 element) and converged (108 000 element) models.

Displacement control was used to apply tension to the models, as described in Section 4.3.2. All of the mesh models provided nearly identical force-strain response curves. The reaction force variations were all within 4 N or 1.2 % of one another when considering the corresponding final (maximum) strain values. In order to provide an accurate representation of tensile sample behaviour, the mesh density of the 13 500 element model was deemed appropriate.

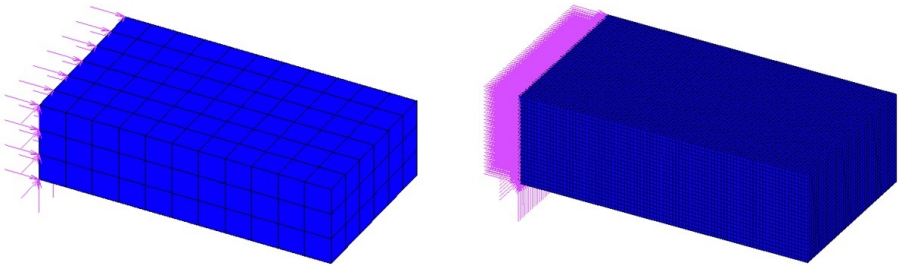

Figure 4.8: Illustration of mesh refinement on uni-axial tensile simulation models. The original course mesh (left) consisted of 198 elements, while the finest (right) had a total of 108 000 elements.

4.3.4 Results: apex rubber

The apex rubber was modelled using the three-term version of the third-order Mooney deformation model, requiring the identification of coefficients C_{10}, C_{01} and C_{11}. Converged coefficients values can be viewed in Table 4.5, along with the initial values used by the DOT procedure. Final converged coefficient values conformed to the Mooney Rivlin three-term stability criterion, as per equation 4.3. The numerical versus experimental RMS error objective function had a final value of 0.945 (equation 4.1), with a resulting force-strain curve as shown in Figure 4.9. The figure shows the combined material response of the entire apex sample region. The force versus strain response is illustrated, as opposed to stress versus strain, as it is not dependant on individual material region geometries.

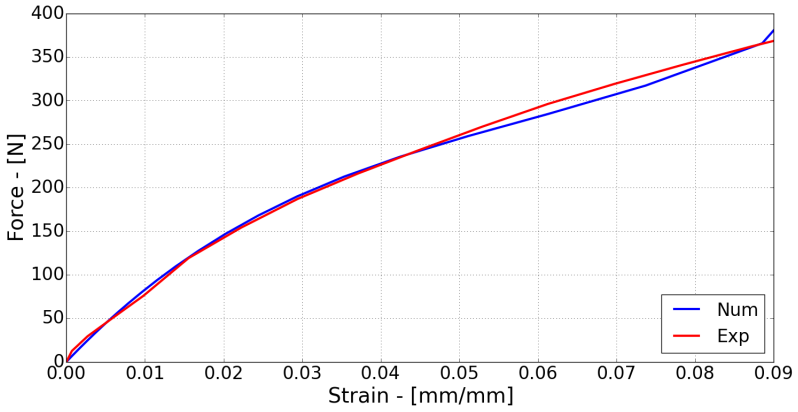

Figure 4.9: Apex tensile sample result comparison of converged numerical solution (using iterative DOT procedure) and experimental results.

Table 4.5: DOT optimisation results for Apex rubber.

Coefficient	Initial values	Converged values
C_{10}	-1.87597e+007	-1.07124e+008
C_{01}	2.02023e+007	1.16883e+008
C_{11}	2.07861e+007	1.04791e+008
RMS error	-	0.945

4.3.5 Results: cord rebar

The purpose of the cord rebar was to add tensile strength to the rubber material in the outward radial direction within the sidewall of the tire. Heat generation due to cyclic loading within this region is solely due to hysteresis of the sidewall rubber. The cord rebar was therefore modelled as a simple isotropic material, adding a linear stiffness component to the regions stress-strain response. The DOT procedure loop identified a suitable set of material parameters within seven iterations, with values provided in Table 4.6. The Young's moduli of the material was nearly equal to a value of 500 MPa, as reported by Maritz (2015). Numerical versus experimental force-strain response using the obtained material parameters can be seen in Figure 4.10. It shows the combined material response of the sidewall radial sample region.

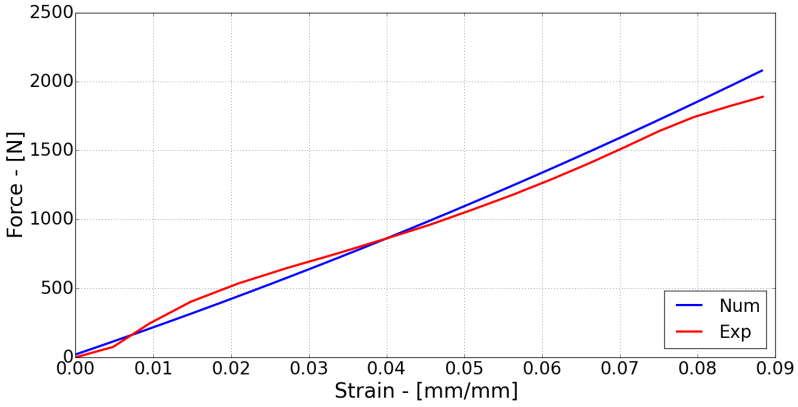

Figure 4.10: Sidewall radial tensile test sample comparison.

Table 4.6: Isotropic cord rebar properties.

Cord rebar	
Young's moduli	497 MPa
Poisson's ratio	0.1

4.4 Hysteresis coefficients

The thermal tire simulation models required hysteresis coefficient values of each elastomer region for use during heat flux calculations. The coefficient value provides an indication of the fraction of deformation strain energy that is absorbed as heat within a material (Section 2.4). In the past a value of 0.1 was used, as commonly deemed appropriate for automotive rubber materials (Maritz, 2015). In order to improve the thermal simulation accuracies, the hysteresis coefficient behaviour of the tire rubber regions were evaluated experimentally as a function of excitation frequency and temperature variation.

4.4.1 Procedure

Dynamic mechanical analysis (DMA) measurements were outsourced to the Council for Scientific and Industrial Research (CSIR) in Pretoria. Samples sent to the CSIR were dissected from a tire, representing the tread, sidewall and apex rubber regions, respectively. They made use of a dual cantilever beam testing procedure to measure the storage and loss modulus of each sample (Section 2.4). The results were subsequently used to compute the resulting hysteresis coefficient values, as per equation 2.15. Experiments were conducted at three frequency intervals, corresponding to forward wheel velocities of 20, 40 and 60 km/h for the tire of interest. Frequencies were established based on the inflated tire radius and velocity of interest. Sample temperature was varied from 20 to 90°C, to account for the influence of heat generation due to cyclic loading.

4.4.2 Results

The influence of excitation frequency and temperature variations on the hysteresis coefficient values were clearly identifiable. This can be seen in Figure 4.11 (a) for the apex and (b) tread samples, with Figure 4.12 illustrating the sidewall results. An increase in sample temperature resulted in overall increased coefficient values, with a noted exception of the tread rubber, which saw a continuous reduction past the 40°C mark. The apex and sidewall sample values showed an exponential growth when temperatures exceeded values of 50 and 80°C, respectively, for 5.18 and 7.77 Hz.

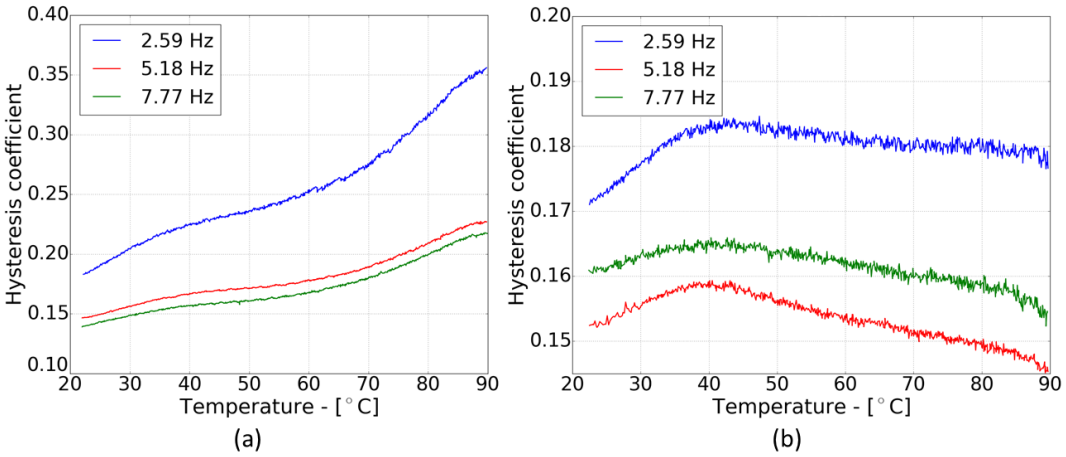

Figure 4.11: Apex (a) and tread (b) rubber hysteresis coefficient variations as function of temperature at three frequency intervals.

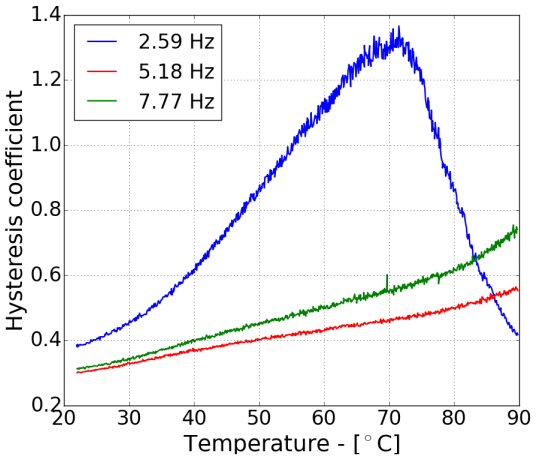

Figure 4.12: Sidewall rubber hysteresis coefficient as function of temperature at three frequency intervals.

The influence of temperature was however overshadowed by that of the particular excitation frequency, with a reduced frequency corresponding to an increased coefficient value. An increase from 2.59 to 5.18 Hz saw a significant reduction, followed by a slight increase when changed to 7.78 Hz. This was again with the exception of the thread region, wherein the lowest coefficient values were noted at the upper frequency.

The overall coefficient values of the tread and apex rubber regions were within the same order of magnitude as the popularly used value of 0.1. For simulation purposes these coefficients were assumed to be independent of temperature, taking the average value at each frequency interval, with results as given in Table 4.7. This was considered acceptable, as typical thermal tire simulation results (Section 7) indicated the material temperatures to vary between 30 and 90°C. Average coefficient values for the sidewall rubber were in excess of 0.4, indicating an excessively large thermal absorption capacity. Experimental temperature measurements taken by Maritz (2015) on an identical tire at similar operating conditions showed contradicting results. The sidewall was found to have a low temperature distribution in comparison to the tread and apex regions. The coefficient values for sidewall rubber were subsequently taken as the minimum measured value at each frequency interval.

Table 4.7: Coefficient values obtained through DMA measurement.

	Hyteresis coefficient		
Excitation frequency	Tread	Apex	Sidewall
2.59 Hz (20 km/h)	0.17	0.25	0.35
5.18 Hz (40 km/h)	0.15	0.18	0.29
7.78 Hz (60 km/h)	0.16	0.16	0.31

4.5 Additional material parameters and coefficients

Thermal properties and material densities used in the numerical tire simulation models can be viewed in Table 4.8. Ebbot *et al.* (1999) identified a variation of 1.2 % in the thermal conductivity K of tire rubber over a temperature range of 30 to 90°C. They were subsequently assumed to be independent of temperature variation during the present study. Values for the thermal conductivity K, specific heat C_p and emissivity ε were obtained from Cengel and Ghajar (2015) and Cho *et al.* (2013). Rubber densities were experimentally determined from samples by the Archimedes density measurement method, using a water filled 1000 mL volume flask (10 mL resolution) and digital mass scale (0.01 g resolution). Cord and steel values were obtained from published literature (Tang *et al.* (2014) and Cengel and Ghajar (2015)).

Table 4.8: Thermal properties and material densities. K - thermal conductivity, C_p - specific heat capacity and ε - emissivity.

	K - (W/mK)	C_p - (J/kgK)	ε	Density - kg/m^3
Apex rubber	0.16	2010	0.95	1189
Tread rubber	0.16	2010	0.95	1561
Sidewall rubber	0.13	2010	0.95	1015
Cord rebar	0.293	2000	-	1200
Steel rebar	45.3	502	-	7833
Bead wire	45.3	502	-	7833

4.6 Conclusion

This chapter described the methods and procedures followed during the identification of material properties and coefficients for use in the numerical tire models. Stress-strain response curves obtained during the uni-axial tensile testing of samples consisting of a single material were used to obtain coefficients for the steel rebar, sidewall- and tread rubbers directly by experimental data fits. The ranges of experimental data related to the rubber regions were adjusted to obtain accurate material definitions within the tire simulation model's strain ranges of interest.

It was, however, impractical to obtain separate samples for each individual material region. Combined material stress-strain response curves were subsequently used to identify the remaining unknown material parameters. This made use of equivalent tensile test simulation models and numerical algorithms which were also discussed. Comparisons between the numerical material response and experimental data curves were made throughout, obtaining satisfactory results. The thermal material properties and coefficients were sourced from published literature, whilst the rubber material densities were determined by Archimedes density measurements. Results obtained from a dynamic mechanical analysis of the rubber's hysteresis coefficient behaviour as a function of excitation frequency and temperature are also included.

Chapter 5

Numerical simulation of tire

The material definitions established in Chapters 3 and 4 were subsequently incorporated into the original four FE tire simulation models created by Maritz (2015). They replaced properties sourced from published literature, with the aim of improving the prediction capabilities of the models. Geometric alterations were also made to represent the structural composition of the tested tire more accurately. Together the models formed a numerical modelling procedure for predicting the heat generation and temperature distribution within a rolling tire due to hysteresis.

5.1 Overview

The numerical models are classified under two main analysis groups, namely structural and thermal. The purpose of the structural part was to perform a dynamic rolling analysis of the tire by modelling its inflation, loading and rolling behaviour. It was the purpose of the first three simulation models to perform these tasks, with results from each being passed on to the next simulation by means of initial conditions. This subdivision of tasks was implemented to provide more computationally affordable sub-simulations, as opposed to a single model for the entire process. It also allowed for incremental validations to be made with regards to experimental test data obtained from a physical tire. The fourth model fell under the thermal banner, with the purpose of predicting the resulting temperature distribution within the cross-section of the tire. It used information obtained during the structural analysis to do so. An illustration of this process is shown in Figure 5.1.

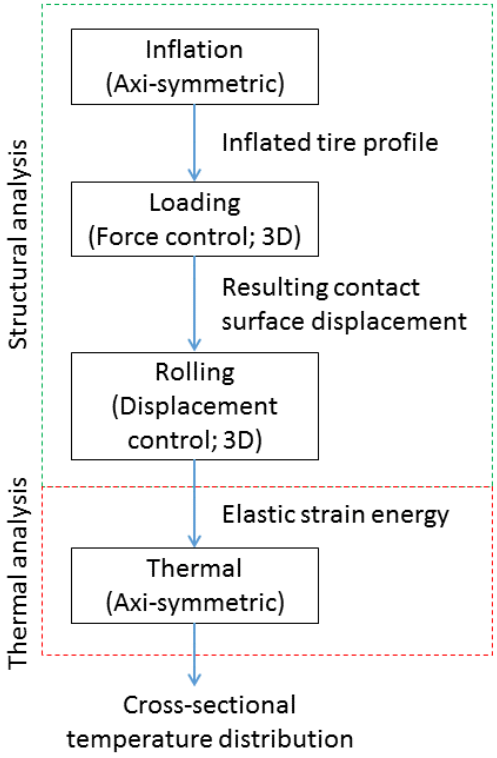

Figure 5.1: Numerical modelling procedure illustrating the interactions between individual simulation models.

5.2 Material regions

The material regions within the original models were updated to conform to the findings of Chapters 3 and 4. This included a subdivision of the originally uniform rubber region (Figure 5.2) into the apex, sidewall and tread, as well as changes to the various rebar components. The newly established material properties and coefficients were also incorporated. The tire, rim and rolling drum profiles were however left unaltered. The updated material regions are shown in Figure 5.3.

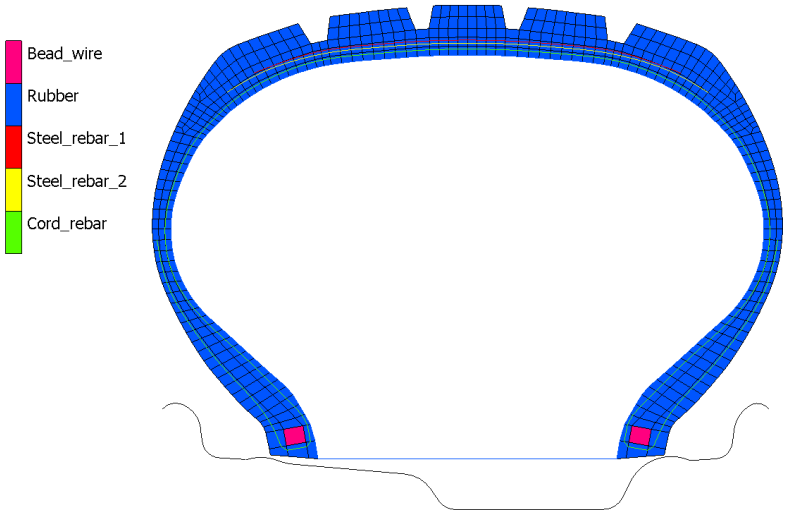

Figure 5.2: Cross sectional material regions originally modelled by Maritz (2015).

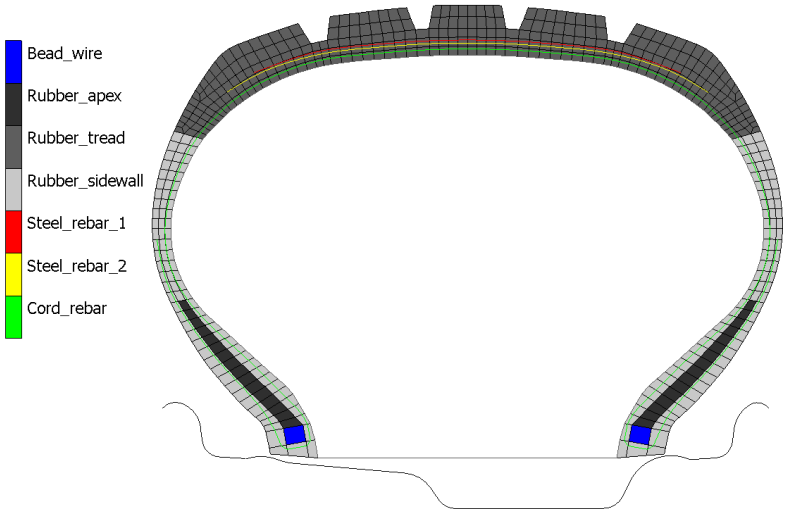

Figure 5.3: Cross sectional material regions when using experimentally established material parameters (Chapter 4).

The axisymmetric mesh originally created by Maritz (2015) (Figure 5.2) contained a total of 800 elements and 953 nodes. Of these 522 were quadrilateral (quad4) elements with typical dimensions of 3×3 mm, with the remaining 278 being linear (line2) rebars with a typical length of 3 mm. The mesh was constructed in order to provide an appropriate level of detail of the tire structure, whilst avoiding an excess number of elements. Use of a coarser mesh would result in a loss of geometric detail, particularly within the internal sidewall and apex rubber regions.

Work published by Cho *et al.* (2013), Baranowski *et al.* (2012) and Tang *et al.* (2014) suggested the use of similarly fine mesh levels when modelling an automobile tire. An axisymmetric mesh constructed by Cho *et al.* (2013) contained 722 elements, whilst an equivalent full 3-D tyre model had 34 656 individual elements. When expanding the current mesh to create a 3-D tire model (Section 5.3.3) the total number of elements was 41 652.

Refining the mesh once, without altering the element aspect ratios, resulted in a significant rise in the number of elements. The number of elements within the axisymmetric model increased to 2 644, whilst the 3-D version contained a total of 274 976 elements. This drastically increased the required computational cost of each model to the point where they became uneconomical to execute. Tang *et al.* (2014) reported similar observations due to mesh refinement on an equivalent tire model. Preliminary model comparisons to experimental tire deformation measurements, as provided in Chapter 6, yielded acceptable results when using the original mesh. Its structure was therefore left unaltered for the remainder of the project.

5.3 Structural analysis

Details of the structural simulation models used to execute the dynamic rolling analysis are provided in the following section. It includes specifications on each model, as well as descriptions of their interactions with one another. All of the models used the large strain structural analysis option, allowing them to capture the large deformations typically observed in a tire. The modelling parameters and reference properties used for cavity pressure loads were the same for each model, as provided in Table C.1. Please refer to Appendix C for details on the load case parameters used in each of the simulation models.

5.3.1 Axisymmetric inflation analysis

The first step was to obtain the inflated profile shape, with the tire mounted in place onto the bead seat of the rim. This was done by applying an inflation boundary condition, as shown in Figure 5.4, to the inner tire region using a cavity pressure load in conjunction with an enclosed cavity surface element. The cavity element did not contribute to the stiffness of the model and was required for volume calculation purposes only (MSC, 2013).

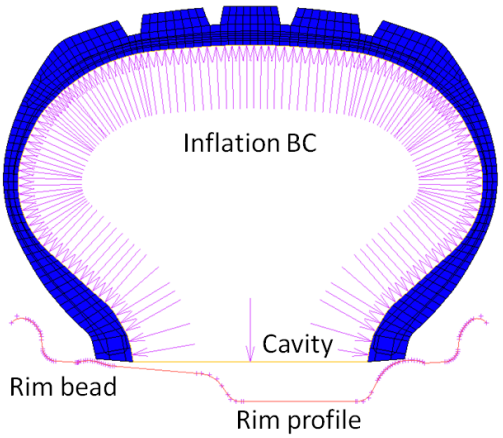

Figure 5.4: Inflation simulation model.

Air was the working fluid of choice, being added gradually over the course of one second to inflate the structure. Conducting the simulation with nitrogen as inflation medium would not influence the results of the structural simulation, as the total pressure change would remain the same. Friction relative to the rim profile was neglected, as the goal was to obtain the final inflated profile shape and not the deformation during inflation. The model consisted of 801 elements and 953 nodes, with the rim being represented by a smooth boundary.

Refer to Table C.2 for details on the inflation load case and its time-stepping procedures. The relative force tolerance was reduced from 10^{-3} in the original models to a value of 10^{-5}. This was required due to convergence issues caused by the reduced stiffness of the newly established rubber material at the tire rim interface.

5.3.2 Loading analysis

The inflation model was expanded using the advanced expand axisymmetric model to 3-D tool within MSC Marc to create a full version of the wheel. A rigid body cylindrical surface was added to represent the rolling-road drum of the experimental tire test bench, which is discussed in Section 6.2 of the report. The number and angles of repetition used were altered from the values proposed by Maritz (2015). This can be viewed in Table C.6. The effective mesh of the resulting tire model had a high resolution within its top region, as shown in Figure 5.6 (Section 5.3.3). This was to improve the model's deformation and contact prediction capabilities relative to the rolling drum surface. The model now consisted of 57 672 elements and 67 609 nodes.

Once inflated, the actual tire bead does not slip on the rim during load application and wheel rotation. This contact interaction was subsequently represented by a touching contact definition with a high friction coefficient of 0.9 (Maritz, 2015). The high friction contact between the tire tread and rolling drum surfaces was treated similarly, using a coefficient value of 0.7. It allowed for some slip between the rubber and steel surfaces during load application, as observed during tread contact patch measurements (Section 6.4.1).

The resulting inflated profile from the axisymmetric inflation analysis was used as an initial condition. This was possible due to the symmetry of the tire around its axis of rotation. The model was therefore inflated from the start, with a constant cavity pressure load being applied to maintain the tire profile shape. It was then replaced by a cavity mass load, holding the air mass constant and sealing off the tire cavity. This made use of the cavity surface element shown in Figure 5.4 as a yellow line. A load control boundary condition was then used in conjunction to apply a force at the centre of the drum, displacing it relative to the tread surface, as shown in Figure 5.5. The load was applied gradually over the duration of one second at a relative force tolerance of 0.001, followed by another half-a-second to allow the model to stabilise. Refer to Table C.3 for details on the load case parameters and stepping procedures used during the load control phase.

The purpose of the simulation model was to predict the force displacement behaviour of the drum relative to the tread surface for a given inflation pressure and load magnitude. This information was then passed on to the rolling analysis model for use in a displacement controlled boundary condition. Since the resulting radial tire displacement (deformation) was known it did not have to be simulated again, thereby reducing the required simulation cost.

The deformed profile shape of the sidewall and tread contact patch was also of interest. It was used to validate the simulations prediction capabilities by comparison to experimentally observed tire behaviour. The model is shown in Figure 5.5, illustrating the deformed shape. The entire model is shown on the left, with a zoomed in cross-sectional view of the deformed tire on the right.

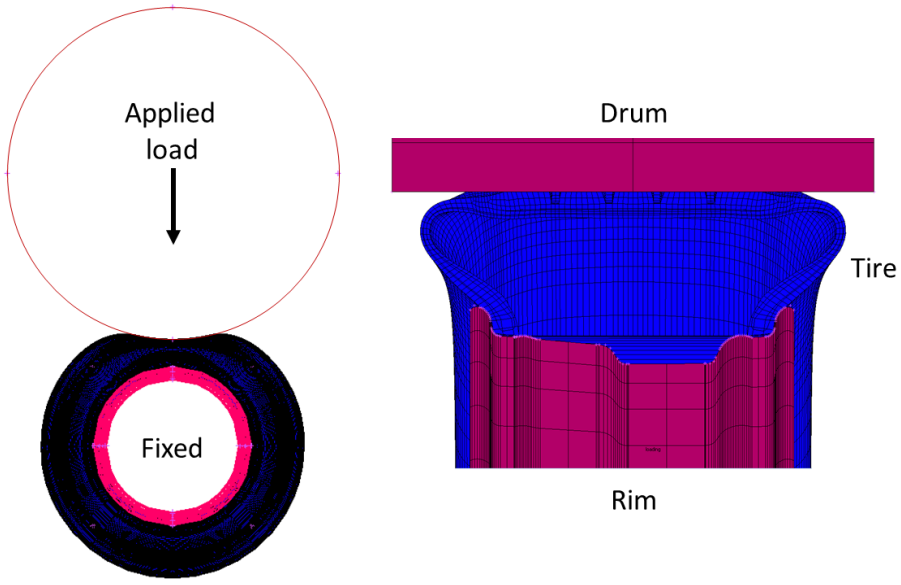

Figure 5.5: Loading analysis model illustrating deformation for 700 kg and 100 kPa.

5.3.3 Rolling Analysis

The rolling analysis simulation model was an adaptation of the loading model, in which displacement control replaced the previously used load control to enforce contact between the rolling drum and tire tread surface. This reduced the models computational expenses, as the resulting displacement magnitude for a given load and inflation pressure was obtained from the loading analysis. The number of expand repetitions and angles were altered from the loading model (Table C.7), as illustrated in Figure 5.6. This was to minimise the number of elements used and thereby further reduce the associated computational cost.

Angular velocities were applied to both the rim and rolling drum bodies, with a resulting equal tangential velocity at the tread contact location. The velocities were not ramped up gradually from a standing-start, but instead given instantaneous values in order to simulate steady-state rolling conditions. This simplification was made in order to avoid additional computational expenses associated with the acceleration of the wheel and drum combination. The table-driven velocity body control option, within the contact body definitions of the rim and drum, was used to apply the vertical drum displacement and rotation (angular velocity) of both components. The particulars of the load case that controlled these actions was identical to that of the load control boundary condition used in the loading model.

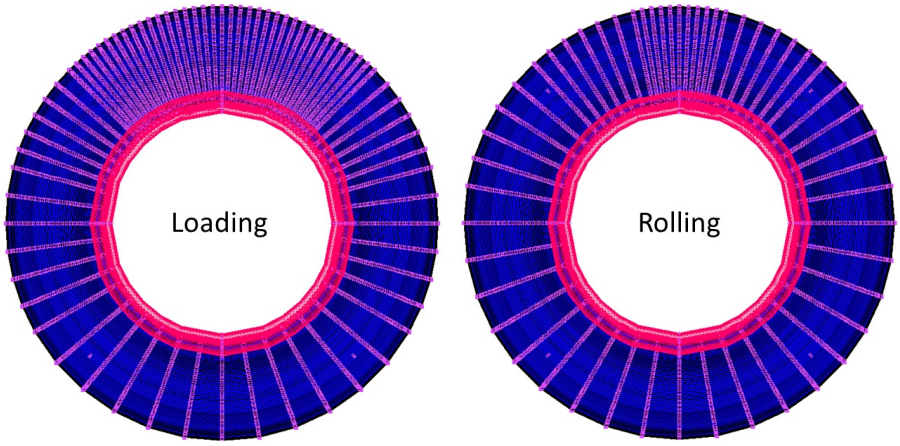

Figure 5.6: Comparison between loading and rolling tire expansions.

Tire inflation was identical to that of the loading analysis (Section 5.3.2), making use of an initial condition obtained from a previous inflation simulation (Section 5.3.1). The inflated tire was first loaded by displacement of the rolling drum over the period of half-a-second (displacement control), which was then held constant for the remainder of the simulation. This was followed by the rotation of the rim and drum. Both components were rotated at constant rotational speeds for two consecutive rotations, to allow the system to stabilise, using a relative residuals force tolerance of 0.001. Refer to Table C.4 for the particulars on the rotational load case.

The purpose of the model was to predict elastic strain-energy density behaviour (Section 2.5) of the rubber components due to cyclic deformation of the tire. Values were extracted from a particular cross-section of elements during the second rotation period and passed on to the thermal analysis procedure. From there it was possible to estimate the magnitude of heat generation within the tire due to hysteresis.

5.4 Thermal analysis

The thermal analysis model was an adaptation of the initial axisymmetric inflation simulation (Section 5.3.1) within the thermal/structural analysis class of MSC Marc. During the first second of simulation time both models are identical, with a cavity pressure load being applied to inflate and mount the structure onto the bead of the rim profile. The simulation then switched to a thermal load case, whilst maintaining a constant inflation pressure. Details on the thermal heating load case are provided in Table C.5. During this period a set of thermal boundary conditions were activated, as illustrated in Figure 5.7, to simulate the thermal behaviour of the tire under steady-state rotational conditions.

The end result of the simulation procedure was an axisymmetric (expandable) representation of the heat distribution within the tire for a particular load case of interest. Heat generation within the tire due to hysteresis was represented by thermal heat flux assigned to the individual rubber elements. The flux magnitudes (J/m^3) were calculated according to equation 2.17 (Section 2.5) as a function of the elastic strain-energy densities obtained during the structural rolling analysis. The flux for each element was subsequently multiplied by its particular volume to obtain the rate of steady-state heat generation. A detailed discussion of this process is provided in Section 6.7 of this report.

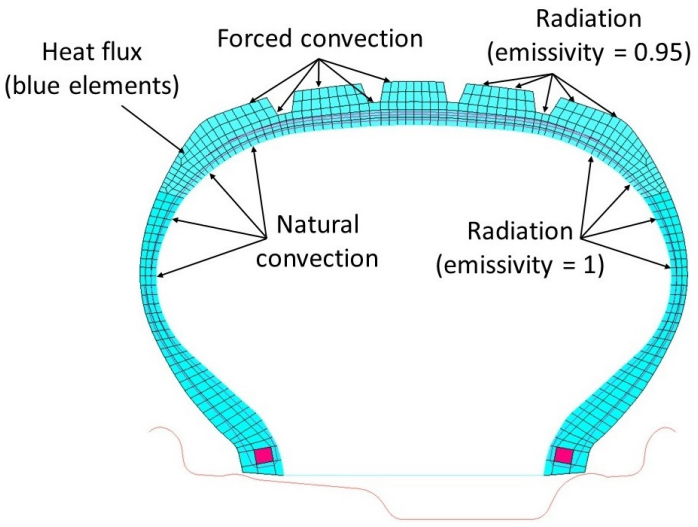

Figure 5.7: Thermal analysis boundary conditions.

The experimental tire temperature measurement procedure, as discussed later in Section 7.1, was conducted prior to the processing of the thermal analysis simulations. In order to perform relevant comparisons, the initial temperatures of both the models and experiments had to be the same. A uniform initial temperature of 27°C was subsequently specified for all elements, whilst the ambient temperature was set to a value of 29°C.

Forced convection was applied to the external sidewall and tread surfaces as an edge film boundary, simulating the influence of air flow past the tire. The film coefficient was calculated by equation 2.22 as obtained from Browne and Wickliffe (1980). A preliminary investigation revealed the steady-state model results to be insensitive to small changes in relative velocity magnitudes. A simplification was therefore made by neglecting the influence of wheel rotation on the relative velocity of air flow past the tire. The velocity component (equation 2.22) was subsequently taken as equal to that of the central wheel hub. For a wheel velocity of 60 km/h the coefficient value was equal to 67.56 $W/m^{2\circ}C$.

A natural convection boundary condition was placed between the internal cavity surface and cavity air, whilst assuming the relative cavity air velocity to be negligible. Ambient temperature magnitudes for both film boundaries were set equal to values measured during testing. The internal cavity air temperature varied significantly between load cases, whilst that of the environment remained relatively constant. Radiation effects were also included for both internal and external tread and sidewall surfaces. Emissivity was set to 0.95 for all external rubber surfaces (Cho *et al.*, 2013), whilst the internal enclosed cavity was specified with a value of 1 (Cengel and Ghajar, 2015). A summary of the thermal material properties used in the models can be viewed in Section 4.5.

5.5 Conclusion

Details of the numerical simulation models used to predict the temperature distribution due to steady-state hysteresis heating within a steel-belted radial truck tire were discussed in this chapter. The models, originally created by Maritz (2015), estimated elastic strain-energy density within the tire rubber regions under constant inflation pressure, load and rotational velocity. Three dependent structural models performed these tasks, with a fourth thermal model converting the strain energy to a resulting temperature distribution. The material properties originally obtained from published literature were replaced with experimentally obtained values, in an effort to improve simulation results. The cross-sectional material region definitions were also altered to represent the modelled tire more accurately. Finally, the contact region mesh within the loading analysis model was refined in order to improve load deformation and tread contact pressure predictions.

Chapter 6

Processing and validation of models

Preliminary validations were executed in order to evaluate the performance of the altered numerical models. The deformation of the tire structure was of interest, since it is proportionally related to the strain energy density response of the model (Section 2.5). Without an accurate prediction of deformation, it would be unlikely to obtain acceptable results from the final thermal analysis.

6.1 Overview

Experimental measurements were taken of the tires sidewall deformation and tread contact pattern relative to the rolling drum surface under a variety of load cases. They were then directly compared to results obtained from the numerical loading analysis models. Additional comparisons were also made with regards to the behaviour of the original tire models presented by Maritz (2015). This was in order to identify the extent of model behaviour improvement by using the experimentally obtained material parameters. The tire used for all measurements was identical to the one upon which the numerical models were based. Details of the experimental tire test bench that was used during this process are also included.

The processing of the elastic strain energy density values obtained from the rolling analysis models is also discussed. This involved the use of a Python script to extract values from its results file, calculate the resulting thermal heat flux and incorporate it into each of the corresponding thermal analysis models. During this process the behaviour and distribution of the strains were also analysed as a function of inflation pressure and load.

6.2 Tire test bench

The experimental tire test bench, as illustrated in Figure 6.1, consists of an axial fan-driven wind tunnel, a 0.87 m diameter steel rolling drum and an electrically driven wheel hub. This allowed a test wheel to be driven at a constant velocity against the drum, as to simulate a continuous road surface, whilst simulating vehicle air flow by the fan unit. The cylinder was height-adjustable, allowing it to exert a constant contact pressure onto the tire tread, using a load cell to measure the reaction force. Two hydraulic jacks and a mechanical screw spacer was used to adjust its height. Although this is a displacement-controlled application, the aim was to apply a load-mass (or radial load) onto the tire tread surface during testing. Simulation comparisons will be made for set load and inflation pressure values. The wind tunnel also had air pressure, temperature and velocity sensors to monitor the environment during testing. A programmable logic controller (PLC) user interface, as set up and calibrated by Volschenk (2015), was used to control and monitor the drive motor, axial fan unit, load-cell and sensors. The interface consisted of a Siemens PLC, Siemens software and Wonderware In-touch software installed on a desktop pc next to the test bench.

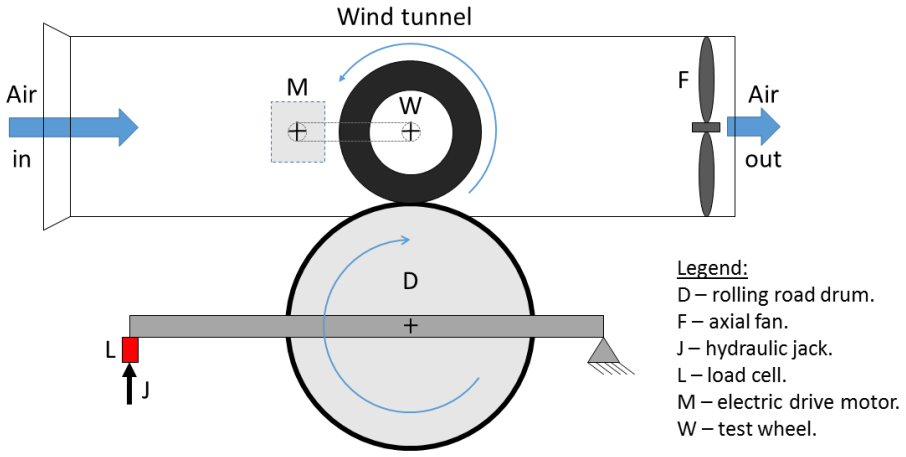

Figure 6.1: Illustration of experimental rolling road tire test bench.

Slip rings located on the drive hub were used to transmit temperature and inflation pressure data from sensors located on the wheel to the PLC system. The ambient cavity temperature and pressure was measured by sensors fixed to the side of the rim. The temperature of the inner tire cavity surface was originally measured by means of four thermocouples, glued to its surface. Cyclic loading, due to sidewall deformation under load, led to premature and uncontrolled failure of the thermocouple wires.

Three infra-red Calex PyroCouple temperature sensors were subsequently used as replacement, with specifications as given in Table B.5. Threaded plugs were machined and welded in-place onto the inner rim surface, as shown in Figure 6.2 with a sensor installed.

Figure 6.2: Calex IR PyroCouple installed in test rim.

Sensor locations and orientations were selected to provide readings of the central tread, shoulder and central sidewall regions respectively. Each sensor provided an area-averaged temperature reading of the surface region it shined on, as illustrated in Figure 6.3 on the left. Corresponding numerical results were subsequently extracted from the thermal simulations (Section 5.4) at the nodal locations along path a-b, as shown on the right of the same figure. The symmetry of the tire and its thermal distributions meant that both experimental and numerical results could be plotted on the same graph, as provided later in Section 7.2.

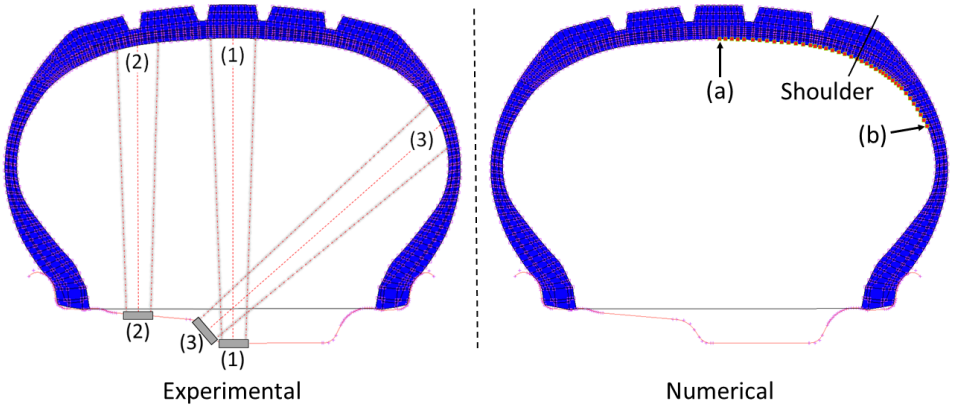

Figure 6.3: Internal cavity IR measurement locations (left) and thermal simulation model nodal locations along path a-b (right).

6.3 Sidewall profile shape

The inflated tire sidewall was measured using the LaVision DIC equipment (Section 3.6.1). Measurements were taken of the region in direct contact with the rolling drum surface on the experimental tire test bench. This was done at different load and inflation pressure values, with the wheel in a stationary position, for both deformed and undeformed cases. The resulting cross-sectional profile shapes and maximum out-of-plane deformation magnitudes were then compared to those of the loading analysis models (Section 5.3.2). Comparisons were also made to simulation results using the original (Maritz, 2015) material definitions.

6.3.1 Experimental setup, procedure and processing

The test setup was identical to the one used by Maritz (2015) for experimental tire deformation measurements, as shown in Figure 6.4 (a). A high contrast speckle pattern was applied to the sidewall region of the tire on the tire test bench, followed by the set-up and calibration of the DIC. The steps illustrated in Appendix A.1 were followed to calibrate the system with respect to the tire speckle pattern located up against the rolling drum surface.

With the tire inflated, a radial load was gradually applied to its tread surface by lifting the drum using the hydraulic jack. The DIC apparatus recorded the sidewall surface deformation during this time. This continued while monitoring the load-cell reaction force until the required load value was reached. Measurements were also made of the maximum out-of-plane sidewall deflection (across the tire width) by means of a mechanical dial gauge and large Vernier calliper. The measurements were used to validate the results obtained from the DIC. The inflation pressure and load values evaluated during testing can be viewed in Table 6.1.

Following testing, the DIC data was processed, as described in Appendix A.2, with results similar to part (b) of Figure 6.4. Together parts a and b of the figure illustrate the region of interest and resulting out-of-plane deformation obtained for a radial load of 300 kg and inflation pressure of 100 kPa. The outermost edge of the rim profile was to be used as reference location for graphical comparison with the numerical sidewall profiles and was therefore included in the post-processing mask image. The default output text files, corresponding to individual DIC images, were used to extract the x, y and z (out-of-plane) co-ordinates of each pixel. The stereoscopic DIC apparatus made it possible to measure object deformation in a 3-D space. From there it was possible to obtain a cross-sectional profile of the deformed sidewall for the region in direct contact with the drum surface. Nodal data was also extracted from the same location within the numerical loading models for each load case.

The results could then be graphically compared within the same coordinate system, as provided in the following section of the report.

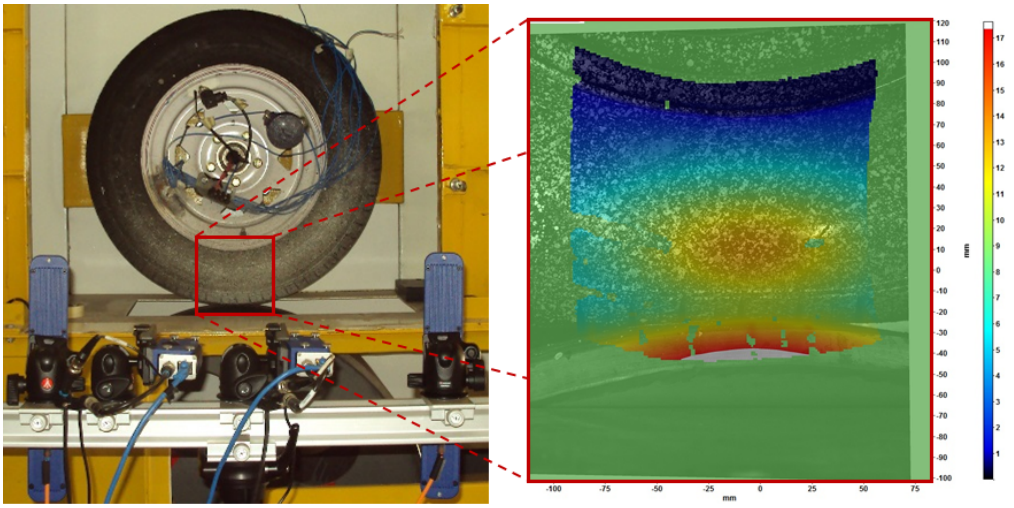

Figure 6.4: Experimental setup (a) used for sidewall profile measurements (Maritz, 2015). It illustrates the DIC region of interest (red square), along with typical out-of-plane deformation results (b) in mm obtained during post-processing.

6.3.2 Results

Typical results obtained from the sidewall deformation profile analysis are illustrated in Figure 6.5 (a) for a low load of 300 kg and inflation pressure of 100 kPa. Results for a load of 300 kg and inflation pressure of 250 kPa can be seen in Figure 6.5 (b). The actual drum surface location in each case is illustrated by the dotted black line. Note that the profiles where flipped vertically for illustration purposes, with the rim contact location being at 0 on the z-coordinate axis.

The numerical results, obtained from the loading analysis simulation models (Section 5.3.2), provided an acceptable representation of the experimental profiles for both the (100 kPa) low- and high (250 kPa) inflation load cases. The cross-sectional sidewall profile results were analysed through observation (subjective) and not through mathematical calculation. A mathematically based analysis was however performed on the maximum out-of-plane sidewall deformations, with regards to the numerical prediction errors (Table 6.1).

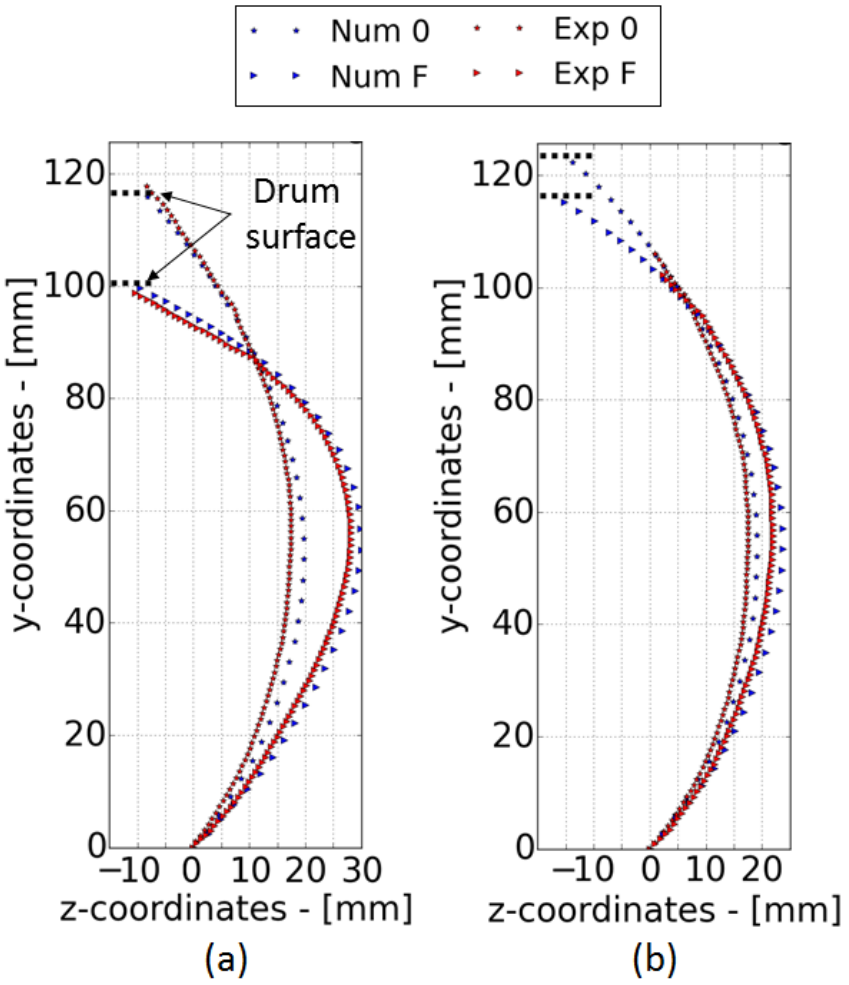

Figure 6.5: Sidewall deformation profile comparisons for (a) 300 kg & 100 kPa, and (b) 300 kg & 250 kPa. Num 0 and Exp 0 represent the un-deformed numerical and experimental results, with Num F and Exp F being their final deformed counterparts.

The numerical (Num) curves correlated the best with the DIC results (Exp) for a low load (300 kg) as a function of inflation pressure variation, as shown in Figure 6.6 (a). The correlation was lower for varying loads at a constant inflation pressure. Large variations can be seen between the corresponding curves of Figure 6.6 (b) for an inflation pressure of 100 kPa. The optical method could not accurately capture high degrees of sidewall curvature associated with the low-inflation, high-load cases (700 kg & 100 kPa). An explanation for the low correlation is that the speckles on the outer edge regions of the curved surface would effectively be hidden from the camera's line of sight.

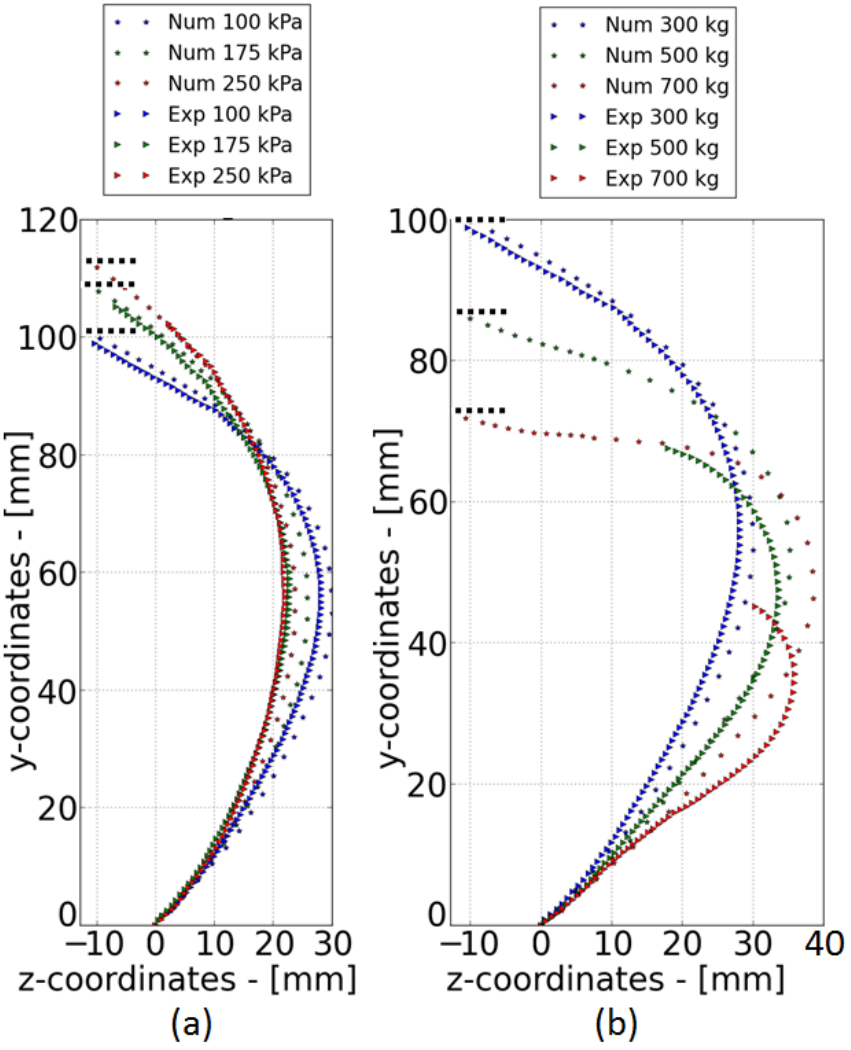

Figure 6.6: Sidewall deformation profile comparison (a) as function of varying inflation at a constant load of 300 kg, and (b) as function of varying load for a constant inflation of 100 kPa.

The benefit of using the experimentally determined (revised) material parameters became evident when comparing the deformed sidewall profiles to the ones obtained from the original models. Excessive stiffness of the materials obtained from literature prevented the tire structure from deforming adequately. This was also noted by Maritz (2015) during the execution of the initial project. It is again emphasised that the objective of his work stipulated the use of such materials, with the focus on establishing the FE modelling procedure. A typical results comparison can be seen in Figure 6.7.

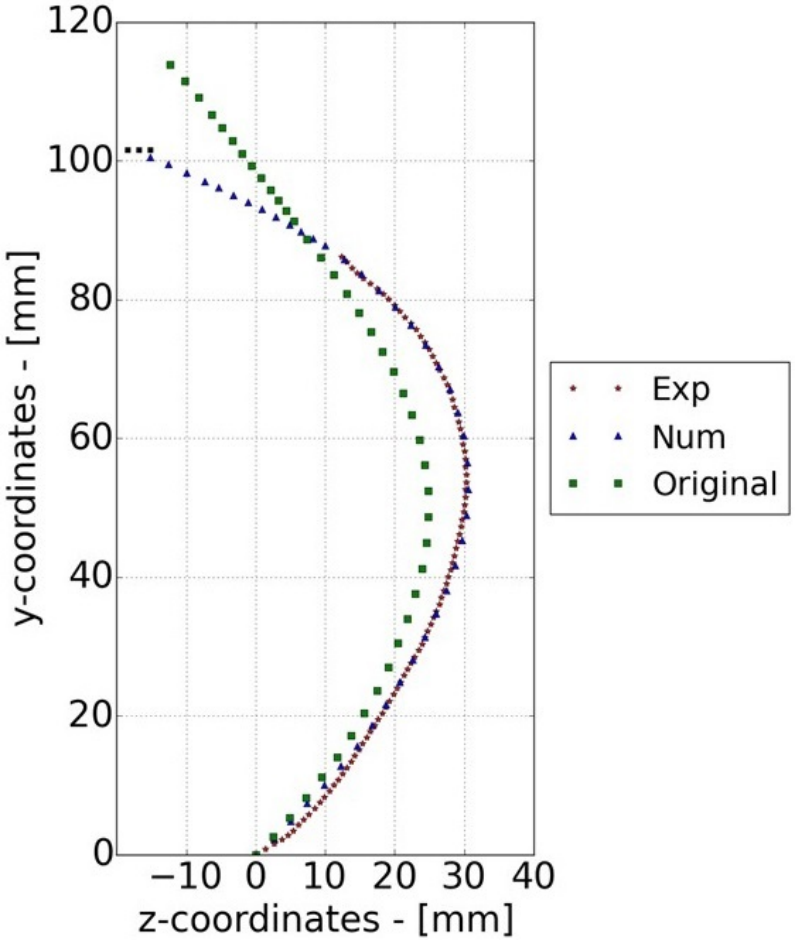

Figure 6.7: Comparison between DIC, revised numerical (experimentally determined material parameters) and original (Maritz, 2015) model sidewall deformation for 500 kg and 175 kPa.

The maximum changes in sidewall deflection can be viewed in Table 6.1 for all of the evaluated load cases. The error percentage column provides relative error percentages between the numerical (revised) and experimental results, as per equation 6.1. The percentage improvement column in turn refers to the relative percentage increase in prediction accuracy between the revised numerical and original (Maritz, 2015) simulation results with regards to the experimental results, as per equation 6.2. Measurements were taken at the location against the sidewall that underwent the largest deformation change during loading. The revised numerical models matched both the DIC and experimental measurements of the maximum out-of-plane sidewall deformations, with less than a millimetres discrepancy. Prediction errors relative to the measured values were substantially reduced in comparison to the original simulation results.

Table 6.1: Maximum out-of-plane sidewall deformations (mm) due to radial tread load application. Experimental micrometer measurement and DIC results, as well as numerical simulation results using revised (experimentally determined) and Maritz (2015) (original) material parameters. Numerical results obtained from loading analysis simulation models (Section 5.3.2). Error % equal to relative error magnitudes between experimental and revised simulation results. Percentage improvement refers to the relative error between the revised and original simulation results with respect to the experimental measurements.

Inflation pressure: 100 kPa						
Load	DIC	Exp	Maritz	Revised	Error %	% Improvement
300 kg	10,77	10,50	2,81	10,12	3,62	69,62
500 kg	17,36	17,00	5,89	15,51	8,76	56,59
Inflation pressure: 175 kPa						
Load	DIC	Exp	Maritz	Revised	Error %	% Improvement
300 kg	6,37	6,50	2,21	6,56	-0,92	66,92
500 kg	11,67	12,00	4,36	11,21	6,58	57,08
700 kg	15,65	16,50	6,98	15,00	9,09	48,61
Inflation pressure: 250 kPa						
Load	DIC	Exp	Maritz	Revised	Error %	% Improvement
300 kg	4,50	4,50	1,91	4,53	-0,67	58,22
500 kg	8,11	8,50	3,57	8,44	0,71	57,29
700 kg	11,78	12,50	5,64	11,76	5,92	48,96

$$Error\ \% = \frac{Experimental - Revisednumerical}{Experimental} \times 100 \tag{6.1}$$

$$\%\ Improvement = \frac{Revisednumerical - Maritznumerical}{Experimental} \times 100 \tag{6.2}$$

6.3.3 Conclusion

The sidewall deformation of the updated (revised) numerical models was adequate in predicting the mechanical behaviour of the physical tire under inflation pressures of 100 and 250 kPa, and radial loads of 300 and 500 kg. This was due to the reduced stiffness of the experimentally determined material properties that allowed the models to deform appropriately. The maximum out-of-plane DIC sidewall deformation, physical measurements and numerical (revised) simulation results were within one millimetre of one another for each load case. Use of the experimentally determined material parameters resulted in a maximum sidewall deformation relative prediction error reduction of nearly 70 % from the original (Maritz, 2015) material models.

6.4 Tread contact patch

The contact patch profile between the tire tread and rolling drum surface was measured experimentally using a 5151 Newton Tekscan I-scan Evolution pressure mapping system. Measurements were taken at different load and inflation pressure values. Results were then compared to those obtained from the loading analysis models, as described in Section 5.3.2. This was done for both cross-sectional pressure distributions of the tread region under maximum displacement, as well as full contact patch contour plots.

6.4.1 Experimental setup and procedure

The 5151 Newton Tekscan I-scan Evolution pressure mapping system comprised of a hand-held USB port that attaches directly to a flexible thin-sheet pressure pad. Multiple sensels arranged in a square grid profile on the pad are used to measure applied loads at their respective locations by measuring changes in electrical resistance. The system can be viewed in Figure B.1, along with its specifications in Table B.6. Accompanying I-scan software was used to interpolate the measured sensel readings, providing a graphical representation of a particular contact profile.

The pressure pad was placed between the tire tread and rolling drum surface of the tire test bench, as shown in Figure 6.8. The 80 $\times$ 80 mm pad was carefully centred around the origin of the tread contact region and adjusted as to capture the entire contact region across the width of the tire, with masking tape preventing it from shifting. Two layers of thin sacrificial plastic sheets were then placed between the tread and pressure pad, to prevent damage to the sensels. The tread rubber had a tendency to expand and slide slightly relative to the drum when loaded, causing delamination of the sensel grid and subsequent failure of the pad.

The testing procedure and load case parameters were identical to those of the sidewall deformation measurements, as described in Section 6.3.1 and Table 6.1 respectively. An additional step was however required with regards to the calibration of the Tekscan software for each load increment.

This involved applying a known load, approximately a 10 % overload of the to-be-measured value, to the pad and saving the measurements to a calibration file. Loading the file calibrated the sensels prior to testing.

Figure 6.8: Pressure pad placement between drum and tire tread surfaces during contact patch measurements.

6.4.2 Processing

Individual sensel measurements and corresponding $x - y$ co-ordinates were obtained directly from the Tekscan software output files for each load case. This was done by means of a Python script file, followed by two graphing procedures. The first provided a pressure distribution profile across the width of the pad, with the second being a top-view contour plot showing the entire patch region. In both cases the numerical simulation results from the updated and original models were also included.

The cross-sectional profiles made it possible to directly plot and compare the numerical versus experimental pressure distributions on one graph. Values were obtained across the central contact region in each case where the tread displacements and therefore loads are a maximum. The graphs provided significant insight into the shape, deformation and load-bearing capacity of the tire as a function of load and inflation pressure variation. For all cross-sectional plots (Section 6.4.3) 0 represents the centre of the tread region.

Contour plot data originating from the numerical models required additional processing in order to be comparable with the pressure pad results. With the tread in contact with the rolling surface, it took on the curved shape of

the drum. The co-ordinates of each tread node in contact with the surface therefore had to be transformed onto an equivalent flat plane. This would be similar to removing the sensel pad from the tread and drum interface, with all the measurements being on the same equivalent flat plane surface.

The numerical and experimental data was processed by the same Python script, utilising a liner interpolating function to graphically illustrate the results. The colour maps and data ranges were the same for all load cases, with the latter being set equal to the maximum principal observed pressure value.

6.4.3 Results: cross-section

The numerical versus experimental results were similar for all load cases, with load and inflation pressure having inverse influences. Numerical results were obtained from the loading analysis simulation models (Section 5.3.2), using the experimentally established material parameters. Increase in load, for a relatively low constant inflation, resulted in significantly larger sidewall region loads located at the outer regions of each profile. Pressure magnitudes near the central tread remained relatively unaltered in comparison for both experimental and numerical cases, as shown in Figure 6.9 (a) and (b) respectively. The central legend provided in each figure is applicable to both graphs.

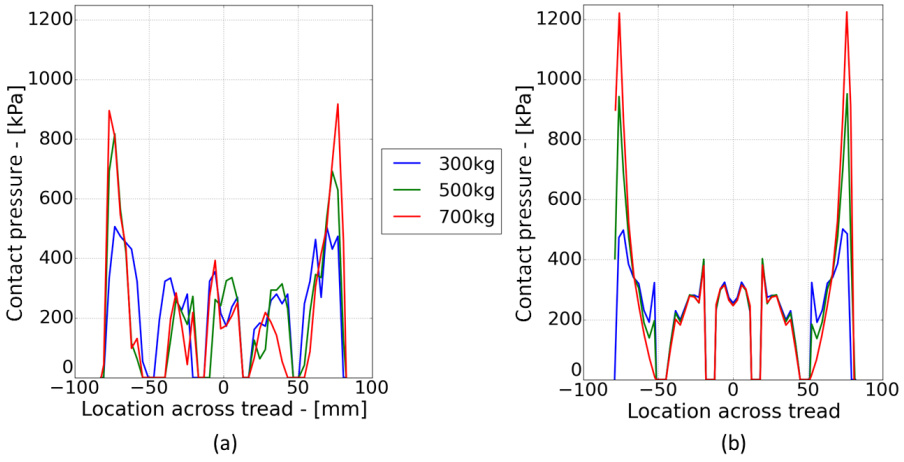

Figure 6.9: Influence of varying load on (a) experimental measurements and (b) numerical predictions of contact pressure profiles under constant inflation conditions of 100 kPa.

The influence of load variation at a high inflation pressure (250 kPa) was less severe, as shown in Figure 6.10. Both the experimental (a) and updated numerical (b) results are shown in the figure. Pressure distribution within the central tread remained fairly constant, with additional weight being supported by the outer sidewall adjacent regions.

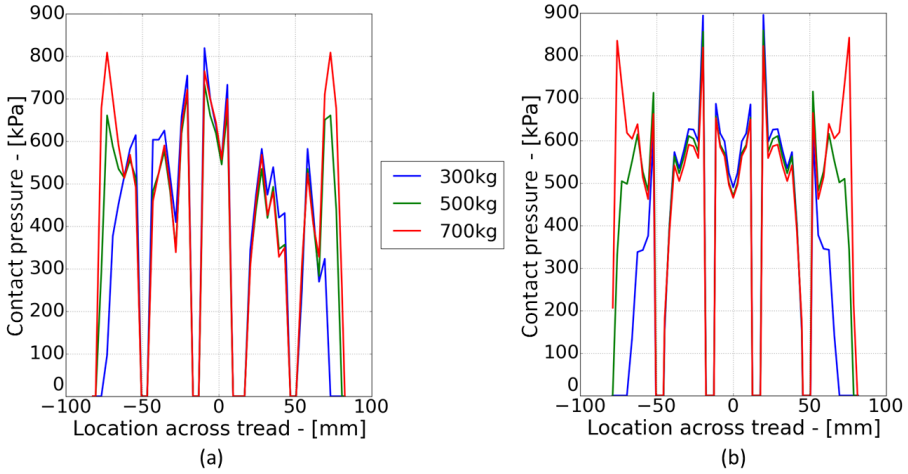

Figure 6.10: Influence of varying load on (a) experimental measurements and (b) numerical predictions of contact pressure profiles under constant inflation conditions of 250 kPa.

Altering the inflation pressure, for a constant given load, resulted in high variations within the central tread region. The contact pressure became more evenly distributed along the cross-section as a result of a pressure increase. This behaviour was observed for both the experimental and numerical cases, as shown in Figure 6.11 (a) and (b) respectively.

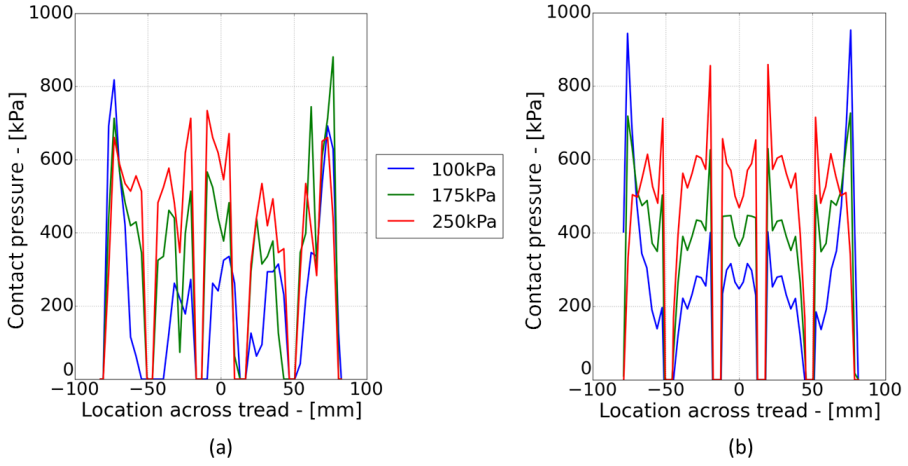

Figure 6.11: Influence of varying inflation pressure on (a) experimental measurements and (b) numerical predictions of contact pressure profiles under constant load conditions of 500 kg.

The original material parameter models (Maritz, 2015) exhibited similar trends with regard to load and inflation variations. Their distributions and magni-

tudes were however in error relative to the experimental and updated material model results. Pressure would either be focused on the inner tread or outer tread, with severe under predictions in the opposing regions for a particular load case. This is comparatively illustrated in Figure 6.12 (a) and (b) respectively.

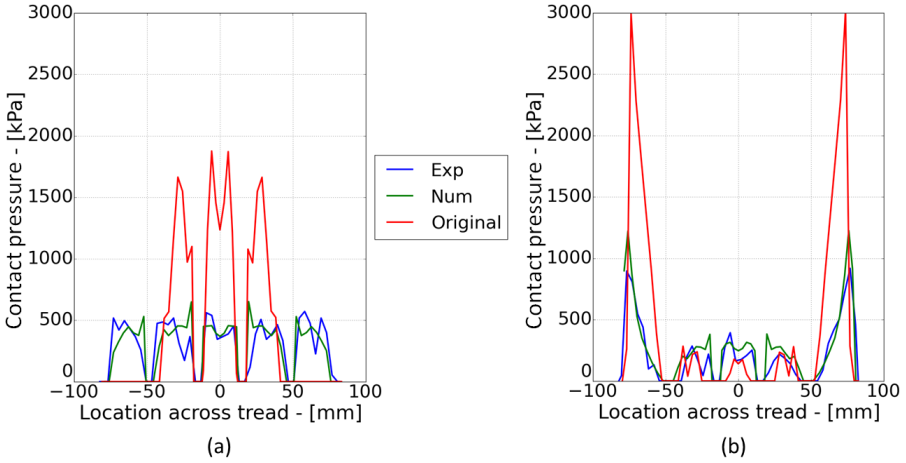

Figure 6.12: Comparison between experimental (Exp), numerical (Num) and original (Maritz, 2015) cross-sectional contact pressures for 300 kg & 175 kPa (a) and 700 kg & 100 kPa (b).

6.4.4 Results: contour plots

Graphical comparisons between the updated numerical and experimental contour plots yielded promising results, with both sets exhibiting similar trends with regards to contact profiles and magnitudes. The contact pressures ranged between 0 and a maximum of 1 000 kPa for both sets. Contour plots showing the contact pressure maps across the width of the tire and length of the contact area are presented in Figures 6.13 to 6.15 for three different load cases.

The legend colour bar in each figure is applicable to both the numerical and experimental profiles. A simplification made within the numerical models was the exclusion of the tread pattern along its circumferential direction. The purpose thereof was to reduce the required modelling and simulation costs. The circumferential tread was however clearly visible within the experimental results and could therefore be included in the scope of future projects if a more accurate representation of a tire is required.

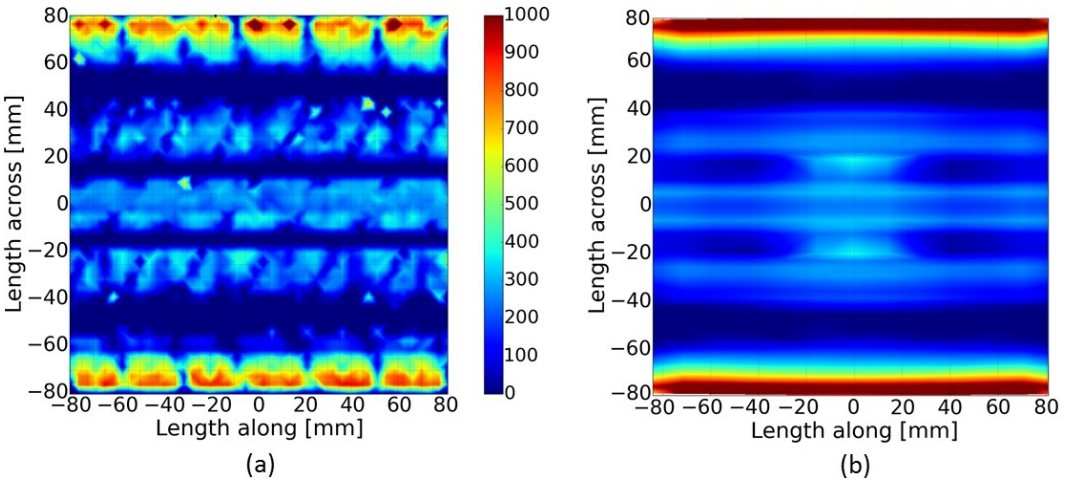

Figure 6.13: Contact pressure (kPa) distribution comparison between experimental (a) and numerical (b) results for 700 kg and 100 kPa. The central legend is applicable to both contour plots, unless stated otherwise.

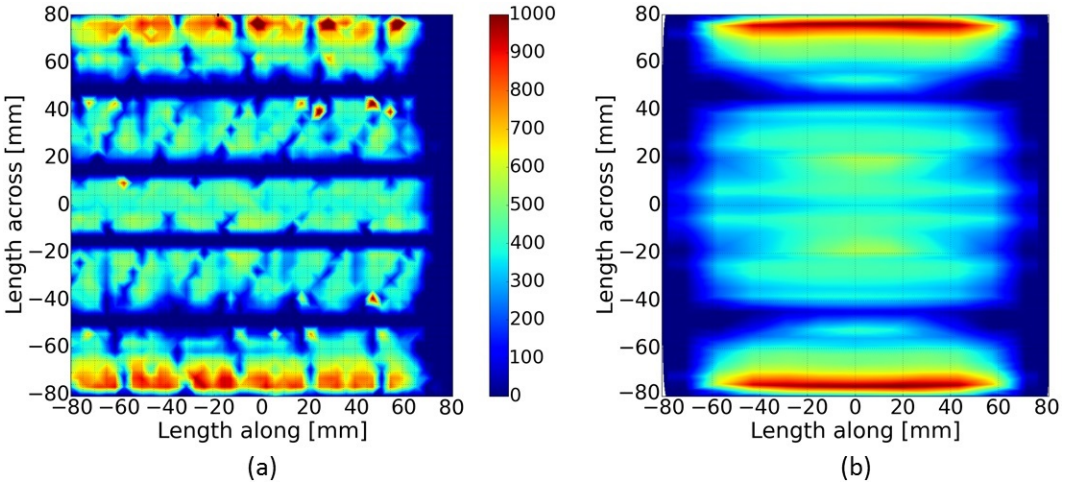

Figure 6.14: Contact pressure (kPa) distribution comparison between experimental (a) and numerical (b) results for 700 kg and 175 kPa.

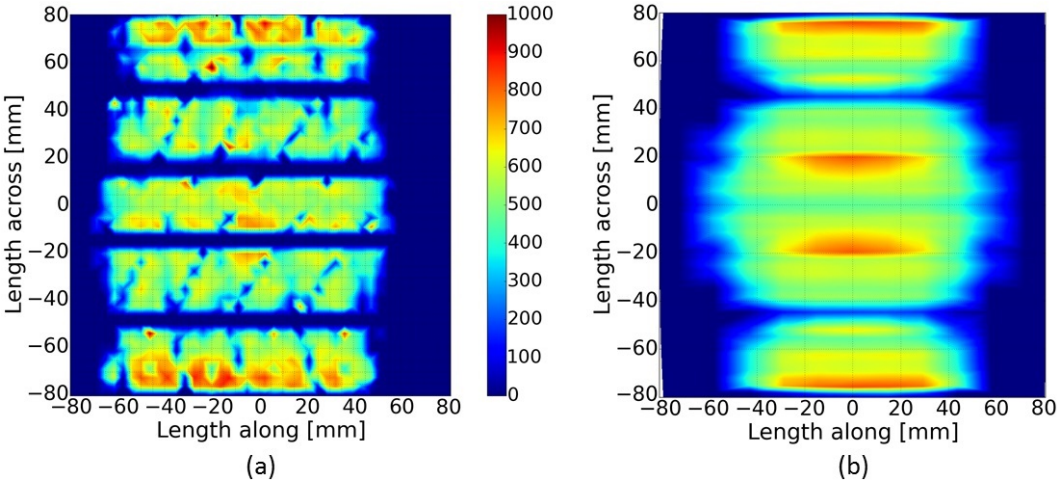

Figure 6.15: Contact pressure (kPa) distribution comparison between experimental (a) and numerical (b) results for 700 kg and 250 kPa.

The influence of inflation pressure and load variations on the distribution and intensity of pressure was clearly identifiable. Inflation pressure increases led to a shift in contact pressure towards the central tread region, resulting in more even distributions for high load cases. For a reduced load the resulting distributions tended towards higher intensities within the central tread region. This can be seen when comparing Figure 6.14 to Figure 6.16.

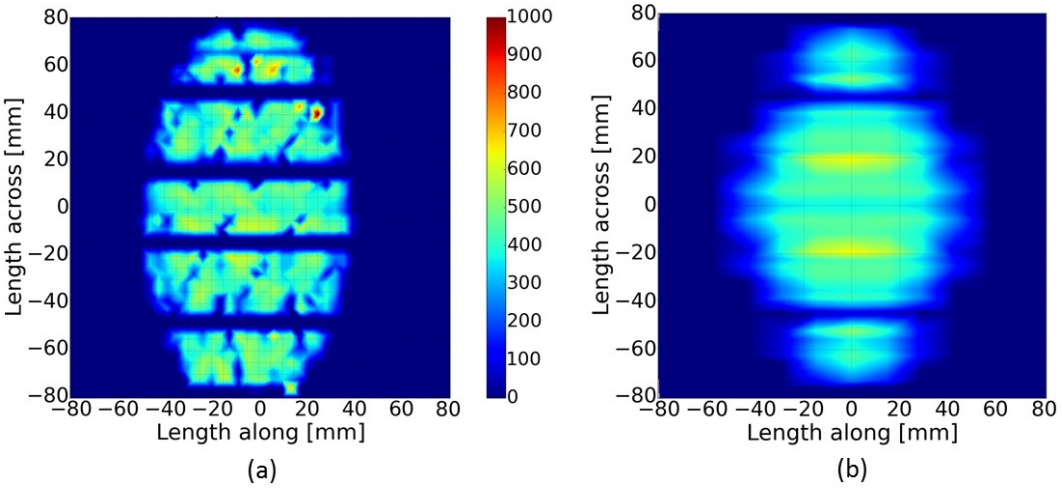

Figure 6.16: Contact pressure (kPa) distribution comparison between experimental (a) and numerical (b) results for 300 kg and 175 kPa.

A variation in load under constant inflation was observed to have an inverse effect, with the focus of contact pressure being shifted towards the sidewall regions. This migration from the central tread can be viewed in Figure 6.16, 6.17 and 6.14. For a low-inflation and high-load cases the majority of load was supported by the outer tread adjacent to the sidewall, as shown in Figure 6.13.

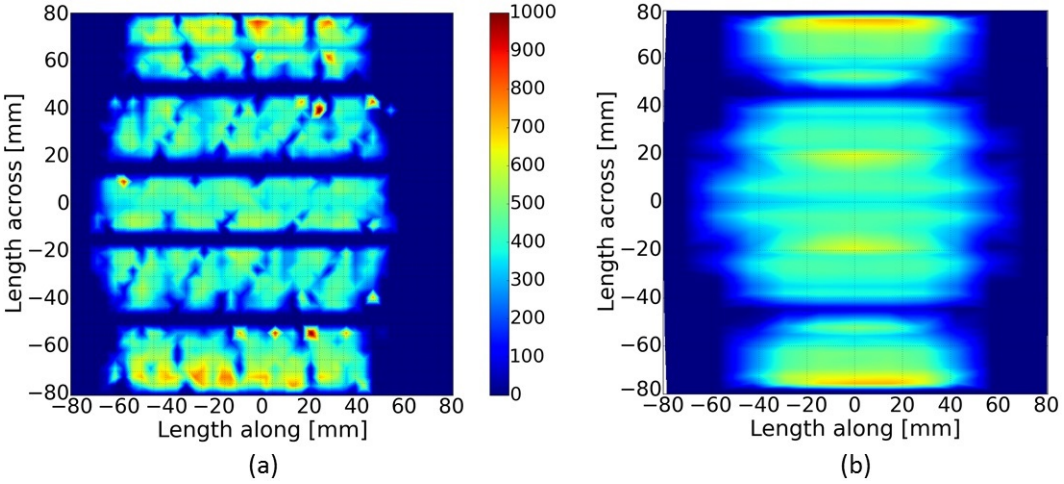

Figure 6.17: Contact pressure (kPa) distribution comparison between experimental (a) and numerical (b) results for 500 kg and 175 kPa.

Use of the original material parameters proposed by Maritz (2015) within the numerical models resulted in overly exaggerated contact patch pressure distributions with regard to both magnitude and profile shape. The elastomers models were too stiff to allow for sufficient deformation of the tire structure (Maritz, 2015), with a resulting contact pressure range increase to 2 750 kPa. Pressure would be focused within the central tread region during low load and high inflation load cases, as shown in Figure 6.18 (b). This behaviour was typical of a significantly over-inflated tire, during which only the central tread makes contact with the rolling surface. When the inflation was reduced and the load increased, the central tread would lift slightly away from the contact surface. This resulted in a circular focus of contact pressure along the outer region of the contact patch, as shown in Figure 6.19.

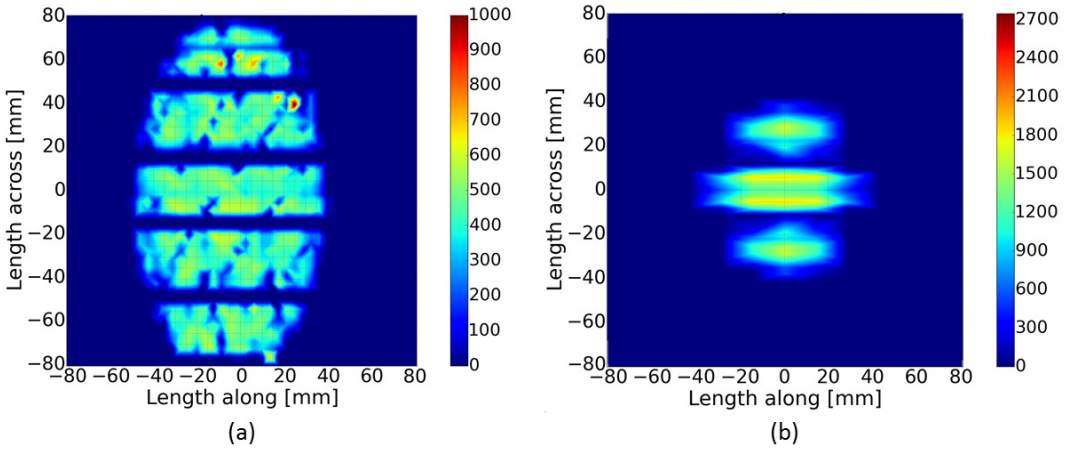

Figure 6.18: Contact pressure (kPa) distribution comparison between experimental (a) and original (Maritz, 2015) model (b) results for 300 kg and 175 kPa. The pressure range increased to 2 750 kPa when using the original material parameters.

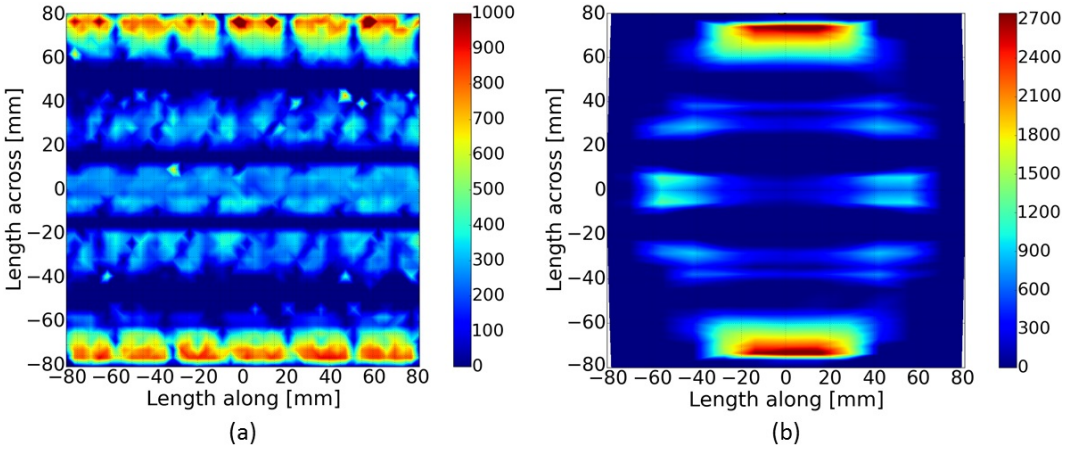

Figure 6.19: Contact pressure (kPa) distribution comparison between experimental (a) and original (Maritz, 2015) model (b) results for 700 kg and 100 kPa.

6.4.5 Conclusion

The ability of the numerical models using the experimentally determined material parameters to predict the tread contact behaviour of the tire was good. This was quantified through observation (subjective) of the obtained contact pressure profile results. Both the cross-sectional distributions and contour plots were remarkably similar to the experimental results for all of the considered load cases. The Python script file used during the processing procedure made it possible to plot the distributions of both data sets for each load case

using the same colour map and legend ranges. In both cases the contact pressure varied between 0 and maximum of 1 000 kPa.

Use of the original material parameters sourced from literature (Maritz, 2015) did not yield accurate simulations of the experimental results. The models would either drastically over- or under-predict the contact patch profile distribution magnitudes. The excessive material stiffness did not allow the structure to deform and distribute the load appropriately. Contact pressure magnitudes exceeded 2 700 kPa for high load cases. The contact profile results highlighted the importance of appropriate tire inflation pressures, in conjunction with individual wheel loads. Under-inflation and/or over-loading would result in excessive deformation and wear within the outer tread and sidewall region. Cornering stability of the tire would also be compromised. Excessive inflation on the other hand would result in insufficient traction due to a reduced contact profile size. Both extremes would reduce occupant safety and total tire life and should therefore be avoided.

6.5 Thermal energy processing

Elastic strain energy density values were obtained from the rolling analysis models for use in the heat generation rate calculations described in Section 2.5. The results served as input to the heat flux boundary conditions within the thermal models (Section 5.4), representing the heat generation due to hysteresis. A Python script file was created to extract the strains from the rolling analysis, calculate the resulting thermal heat flux and implement it into the corresponding thermal simulations.

6.5.1 Selection of increment range

The elastic strain energy density response of a node within the central tread region of a rolling analysis simulation model is shown in Figure 6.20. The peak regions 1 and 2 represent the periods of deformation due to contact with the rolling drum surface. Since hysteresis heating is solely due to the deformation of a material (Section 2.3), strains should only be extracted from either one of the two peak periods for the particular set of elements of interest.

Figure 6.21 provides a normalised illustration of deformation periods 1 and 2 plotted on top of one another, showing the high degree of similarity between the two. Strain values were normalized with respect to the maximum observed change, while the period represents a total of 0.06 s. The contact period during the second rotation, ranging from 1.55 to 1.61 s, was selected by default for the strain extractions and subsequent total strain energy calculations (Section 6.6). Selection of the first rotation period would have a neglect-able influence (Figure 6.21).

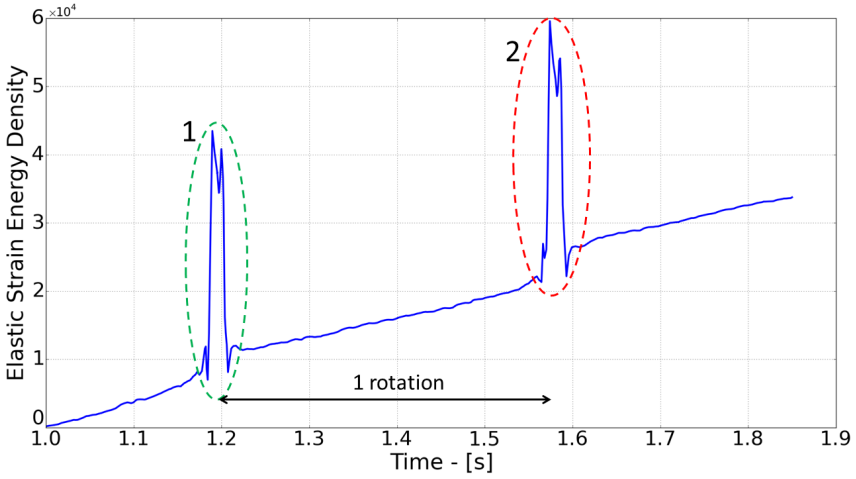

Figure 6.20: Elastic strain energy density (J/m^3) response of a single node within the central tread region, under 500 kg load and an inflation pressure of 175 kPa, for 2 rotations.

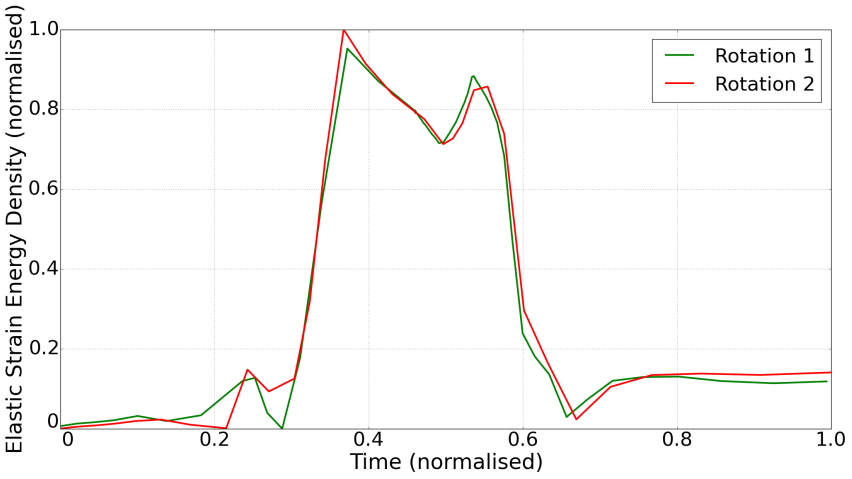

Figure 6.21: Normalised elastic strain energy density comparison between rotation 1 and 2 for 500 kg and 175 kPa showing neglectable variations.

6.5.2 Load, inflation and velocity variation

The influence of load and inflation pressure variations are shown in Figures 6.22 (a) and (b) respectively, for a node located within the central tread region. The results were normalised in each case and plotted from the same origin in order to identify the relative changes, as required by the total strain energy calculations. The influence of increased inflation pressure was clearly identifiable, with an increase in excess of 60 % from 100 to 250 kPa. This coincided with the findings from the contact patch evaluations, wherein the contact pressure was

focused within the central tread region as inflation increased. The majority of load, and therefore strain energy due to deformation, was focused within the central contact patch whilst being reduced elsewhere. This was verified when evaluating the behaviour of various node locations within the tire cross-section.

The influence of load variation for a constant inflation pressure was less significant (Figure 6.22 b). An increase in load resulted in a significantly larger contact patch area, as identified in Section 6.4.4, whilst minimising relative resulting strain increases within the central region. The deformation of the tire structure led to an even distribution of strain energy across the entire contact patch region.

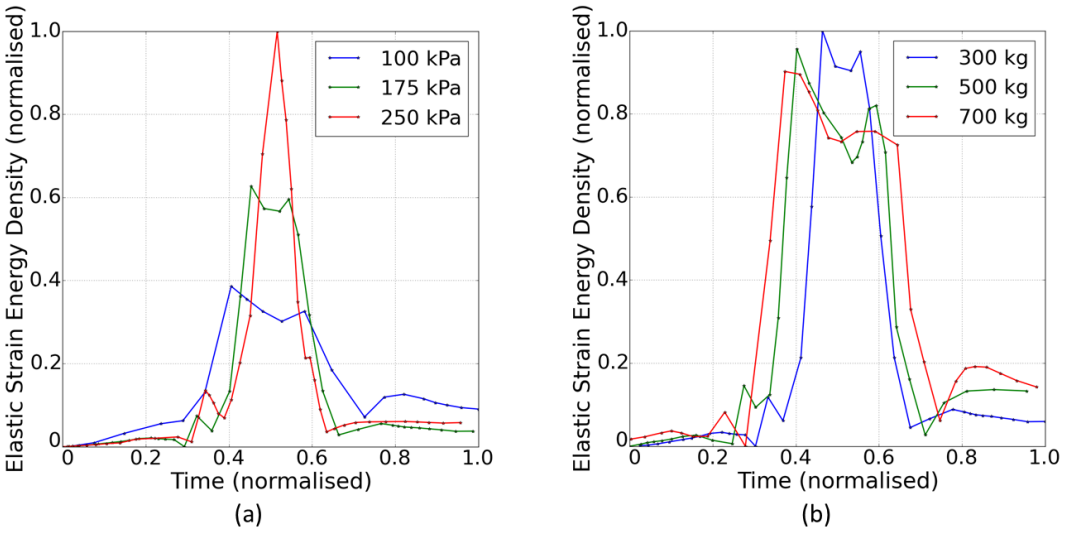

Figure 6.22: Influence of inflation pressure variation (a) under a constant load (300 kg) and load variation (b) for a constant inflation (175 kPa) on elastic strain energy density (J/m^3) response. Normalised results illustrated for a node located within the central tire tread, over the contact time of the second rotation.

The correlation of inflation and load variations with the resulting elastic strain energy density values was similarly described by the contact pressure profile behaviour for the entire tire cross-section. When the contact pressure in a particular location was altered it had a proportional influence on the strain energy within that region. In addition, changes in maximum amplitude values were observed to go hand in hand with the opposing behaviour during the increments before and after the peak.

A comparison of the influence of rotational velocity on the strain values for a node located within the centre of the outer tread region yielded a 1.37 % difference between 20 and 60 km/h. Values were obtained for the duration of one full rotation of the tire, comparing the total energy input due to deformation.

The influence of rotational velocity was therefore negligible with regards to the elastic strain energy densities of the models. Its influence on the thermal response of the tire was however included by the frequency component used within the heat flux calculations, as described in Section 2.5.

6.6 Total strain energy density

The total strain energy density values required for use in the heat flux calculations (Section 2.5) were obtained on an element basis from the elastic strain energy density results of the rolling analysis models. The total strain energy density for each element node was first calculated as the sum of increasing differences over the entire increment range. This was to only account for strain produced within the element due to positive deformations. For this equation 6.3 was used with reference to Figure 6.23. The figure illustrates the elastic strain energy density response of a single node during the second period of deformation. For each increment the elemental equivalent strain energy density is equal to the average of its nodal values. The total strain energy density for each element was in turn equal to its sum over the entire increment range.

$$TotalU_{SED} = \sum_{i=1}^{n} \Delta U_i \tag{6.3}$$

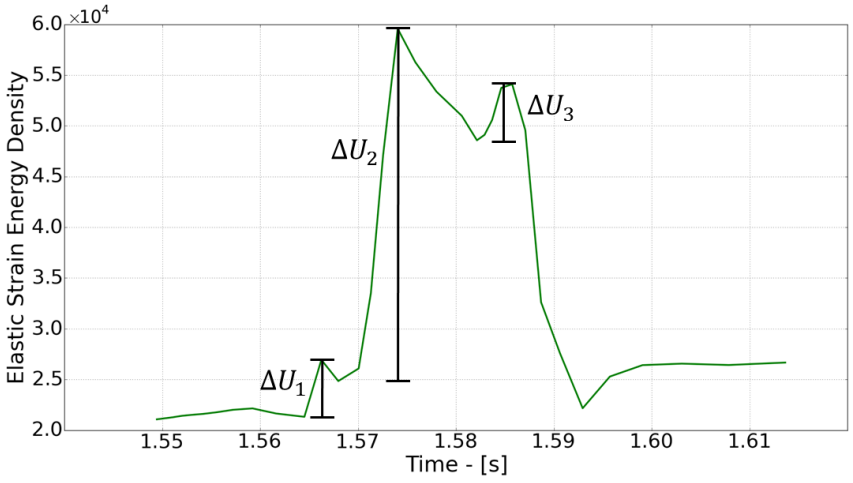

Figure 6.23: Nodal elastic strain energy density (J/m^3) increase during the second rotation.

6.7 Thermal heat flux processing

The next step was to process and incorporate the information from the elastic strain energy density result files into the thermal models as equivalent thermal heat flux boundary conditions. This was done using a Python script file, an element-ID list and the input file of each thermal model. The last is simply a sequential aces data input file, containing the entire definition of the simulation model.

The script file calculated the flux for a particular element, identified the corresponding axisymmetric thermal element via the ID list and wrote the values to the input file. This process was repeated for each element identified in the original list until all of the entries had flux values assigned to them. From there the file was imported and executed within MSC Marc to obtain the resulting temperature distribution prediction. Figure 6.24 provides an illustration of the process executed by the script file.

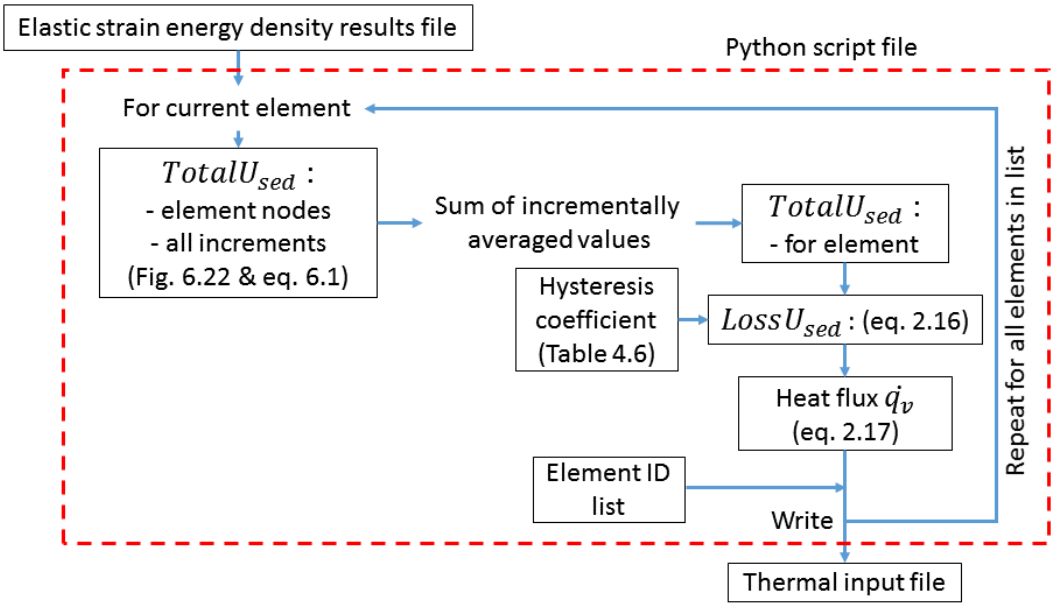

Figure 6.24: Conversion from elastic strain energy to thermal heat flux boundary conditions.

6.8 Conclusion

The findings presented in this chapter focused on the ability of the numerical models to replicate the deformation of the tire structure under a variety of loading conditions. Comparisons between experimental and numerical results revealed remarkable similarities for both sidewall deformation and tread contact profiles. The benefit of using the experimentally determined material parameters was emphasised further by including a comparison of results obtained from the original material models. Finally, the elastic strain energy density values obtained from the rolling analysis models were also discussed. It included a brief overview of the behaviour of the values as a function of the loading parameters of the model, as well as a discussion of the procedure followed in obtaining the resulting thermal heat flux for each element of interest.

Chapter 7

Thermal analysis and comparison

The results obtained from the thermal analysis are presented in the following chapter. Numerical simulation results are compared to experimentally measured temperatures of the internal tire cavity, outer tread surface and sidewall regions. The influence of load and inflation pressure variations was of interest for a constant velocity of 60 km/h. An evaluation of the model's prediction capability for a reduced velocity of 20 km/h is also included. The significance of the numerical results are further highlighted by comparison to results obtained from using the original material parameters proposed by Maritz (2015). A description of the experimental testing procedure is also included.

7.1 Experimental tire temperature measurements

The experimental tire test bench (Section 6.2) was used to determine the thermal response of a tire under steady-state rolling conditions. The test tire was identical to the one used for the material testing procedure. Sensors located on the test rim were used to record the internal cavity air and surface temperatures. A Flir model E60 0.10 thermal camera, with specifications as per Table B.7, captured the sidewall and tread distributions. The hand-held camera allowed for adjustment of object distance, emissivity and reference environment temperature values.

With the tire inflated to a set pressure, a constant radial load was applied to the tread via the rolling drum surface by means of a hydraulic jack. The acquired displacement was thereafter held constant by a large mechanical screw. All initial sensor values, including load, pressure and various temperatures were monitored via the In-touch PLC user interface on the test bench pc and recorded prior to testing. The required rotational velocity, air speed and temperature was adjusted within the software.

With the wheel rotating at a constant velocity; sensor measurements were recorded periodically at 15 minute intervals. Once the temperature readings were found to remain constant (within 0.1°C) for two consecutive increments, the test procedure was complete. Typical convergence time of the temperature values was in the order of 1.5 hours. Final measurements were then recorded of all sensor readings, followed by photographs of the sidewall and tread surfaces with the thermal camera.

7.2 Internal cavity surface

The internal tire cavity surface temperature values were measured during testing with the infrared (IR) Calex pyrocouples, as described in Section 6.2. All of the results were obtained for a velocity of 60 km/h, with the exception of those provided in Section 7.6 for a velocity of 20 km/h. Corresponding numerical simulation (Section 5.4) results were extracted from the nodal locations along the path a-b, as shown in Figure 6.3. Results obtained for a constant inflation pressure of 250 kPa can be viewed in Figure 7.1 for three load increments. The area-averaged experimental temperature measurements are illustrated by straight horizontal coloured lines located within the three vertical grey columns. Each column illustrates the measurement region for each of the three IR temperature sensors used during testing, with reference to Figure 6.3. The colours of both the experimental lines and numerical curves correspond to the provided legend, while the shoulder location is indicated by the vertical black line.

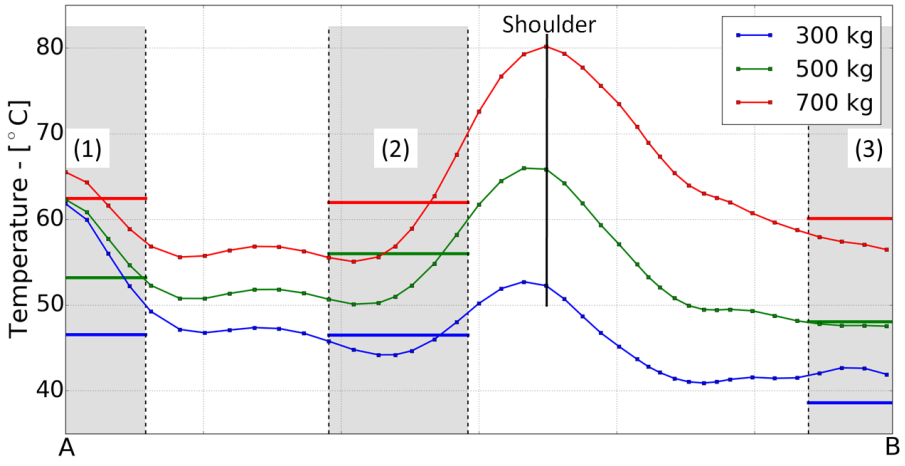

Figure 7.1: Internal cavity temperature results comparison for a constant high inflation pressure of 250 kPa. Area-average experimental temperature results represented by horizontal coloured lines, with grey columns (1, 2 & 3) illustrating IR sensor measurement regions with reference to Figure 6.3.

All three numerical cases exhibited similar trends, with over-predictions in the central tread region (1). The second sensor values were in turn slightly under-predicted, with the sidewall region (3) providing both over and under predictions for the different load cases. Temperature was focused within the central and outer tread block regions within the vicinity of the tire shoulder. An increase in inflation pressure was most notable within the shoulder region, with large relative temperature increases. This corresponded with the contact pressure observations made during the contact patch evaluations (Section 6.4).

A reduction in inflation pressure to 175 kPa saw overall increased prediction accuracies within the central tread region (1), as shown in Figure 7.2. For loads of 300 and 500 kg the results were acceptable with regards to the second sensor values, with slight under predictions being obtained. The third IR region within the tire sidewall in turn saw relatively small under predictions. The results were less accurate for the high load (700 kg) load case, with predominantly under predicted temperatures. Numerical results again indicated maximum temperatures within the shoulder region for all of the load cases.

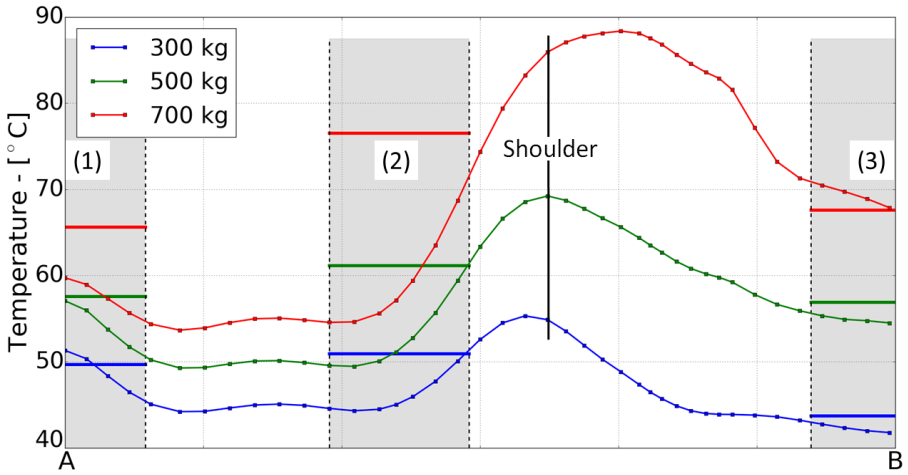

Figure 7.2: Internal cavity temperature results comparison for a constant inflation pressure of 175 kPa.

An increase in inflation pressure for a constant load of 300 kg saw a change in the trends of the numerical simulation results. The maximum temperatures shifted away from the shoulder to the central tread (1) region, as shown in Figure 7.3. The first and second experimental sensor values were over- and under-predicted respectively. The sidewall region (3) saw a combination of slightly over- and under-predicted results.

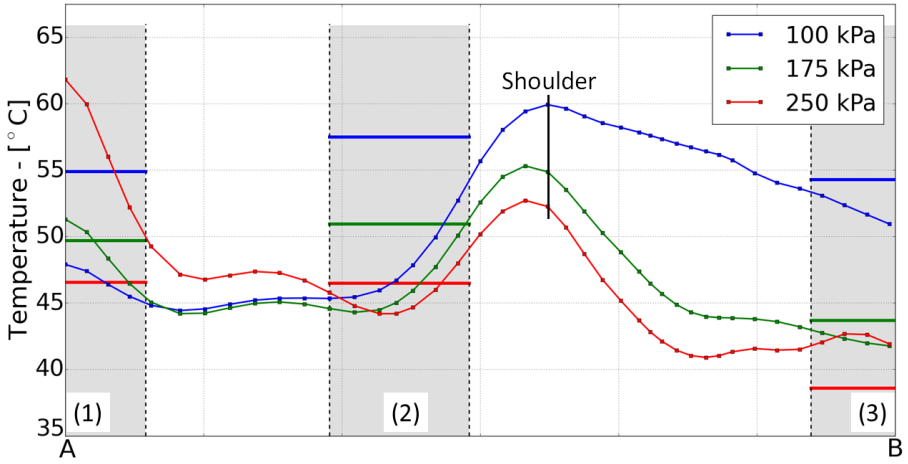

Figure 7.3: Internal cavity temperature results comparison for a constant load of 300 kg.

7.3 Outer tread surface

The tread region temperature distributions for a low load and inflation pressure can be viewed in Figure 7.4. Both the thermal camera image (a) and numerical simulation profile (b) is shown in °C. The legend bar within the camera image shows the maximum and minimum recorded temperature values.

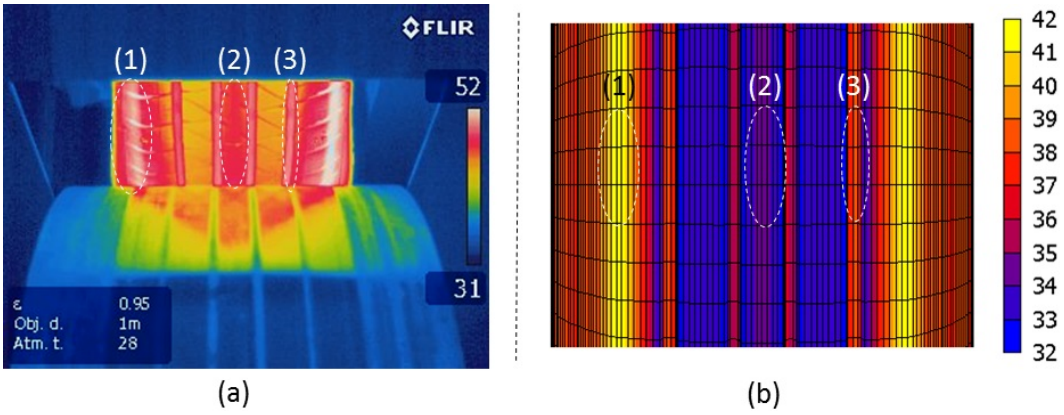

Figure 7.4: Tread region temperature (°C) comparison for 300 kg and 100 kPa, with (a) experimental and (b) simulated (revised materials) results.

The overall distribution trends corresponded well, with maximum temperatures being present within the shoulder regions and circumferential under-cut grooves, as highlighted by numbers 1 and 3 respectively. The central tread band (2) was also slightly warmer in comparison to the regions on either side.

The brightly coloured region directly adjacent to the bottom of the tread was due to reflection against the rolling drum surface and should not be taken into account. When increasing the inflation pressure and load to values of 175 kPa and 500 kg, the experimental temperature distributions appeared largely similar, as seen in Figure 7.5 (b). A significant change could however be observed in the numerical result magnitudes, with the highest temperature remaining within the shoulder regions. Simulation results under-predicted the experimental measurements by a value of 4.8°C for the particular region. The central tread region also saw a notable increase in temperatures and temperature gradients across its width.

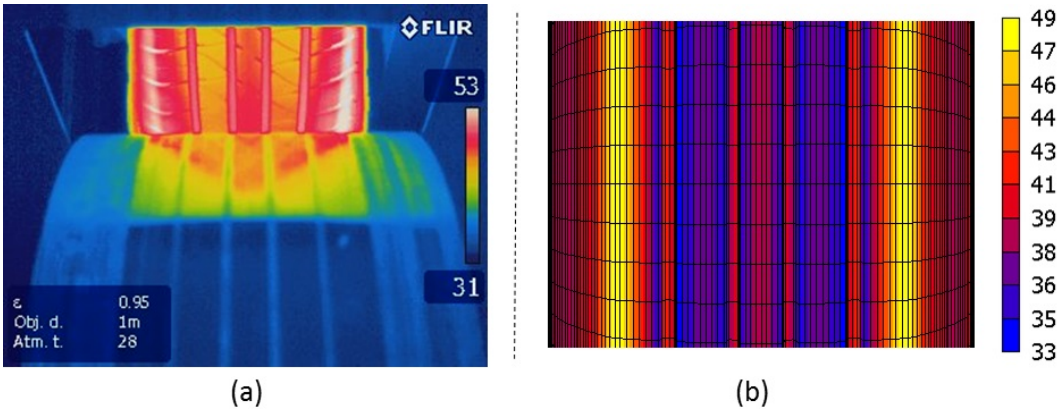

Figure 7.5: Tread region temperature (°C) comparison for 500 kg and 175 kPa, with (a) experimental and (b) simulated (revised materials) results.

The distributions for a high load and inflation pressure provided the best correspondence between experimental and numerical results. Figure 7.6 shows the result for a load and inflation of 700 kg and 250 kPa. The difference between the simulated and measured temperatures for the shoulder and outer circumferential tread grooves was equal to 0.5 and 6.2°C respectively.

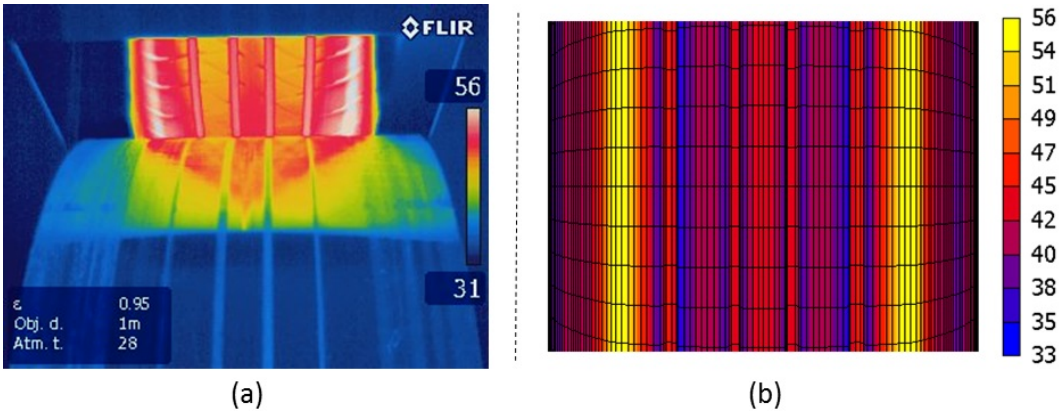

Figure 7.6: Tread region temperature (°C) comparison for 700 kg and 250 kPa, with (a) experimental and (b) simulated (revised materials) results.

7.4 Outer sidewall surface

The sidewall temperature distributions revealed similar results to those of the tread, with maximum values within the tire's shoulder region. Figure 7.7 shows the experimental (a) and numerical (b) results obtained for a low load and inflation case. Only a quarter of the simulation sidewall is shown in order to provide a more detailed view. In both cases the temperature dropped along the radial direction from the shoulder, with the central sidewall region having the lowest values. The values then rose again up to the bead and rim interface. This is further illustrated in Figure 7.8 for three different load cases.

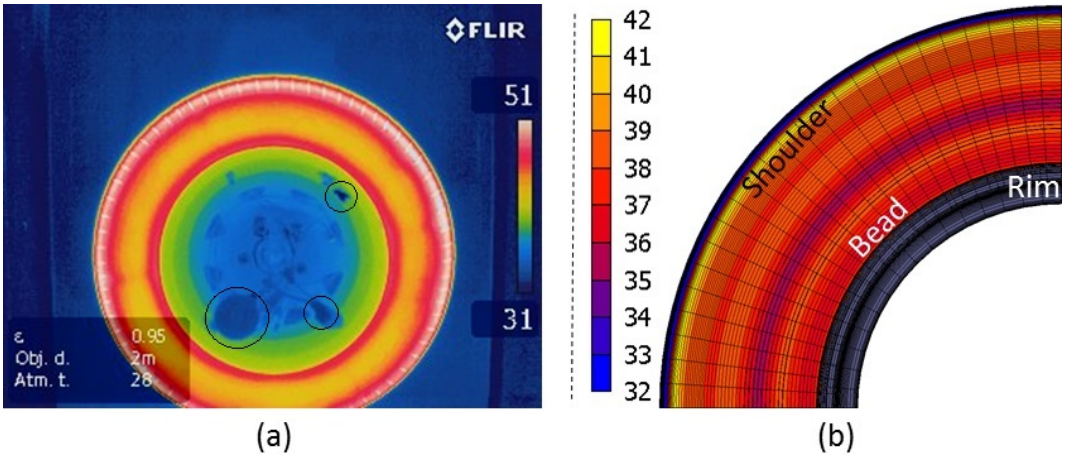

Figure 7.7: Sidewall temperature (°C) comparison for 300 kg and 100 kPa, with (a) experimental and (b) simulated (revised materials) results. Black circled items in (a) are sensors mounted onto the inner rim surface.

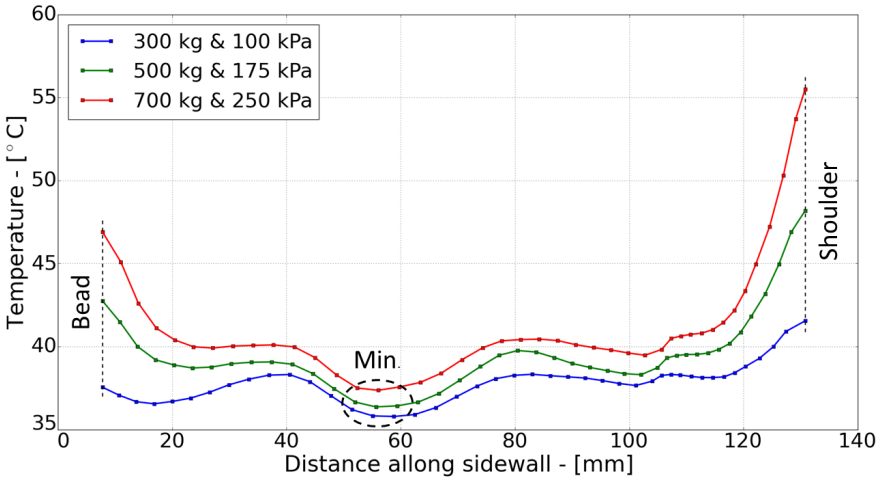

Figure 7.8: Temperature distribution comparison along external sidewall of simulation models. Results illustrate the relatively cool (min.) central region temperatures between the bead and shoulder regions.

An increase in inflation pressure and load resulted in higher temperatures and temperature gradients along the sidewall, with maximum values within the shoulder and bead regions. Additional results can be viewed in Figure 7.9 and 7.10. These figures correspond with the graphs of Figure 7.8. The models provided the best predictions of experimental results for the high load and inflation pressure load case (Figure 7.10).

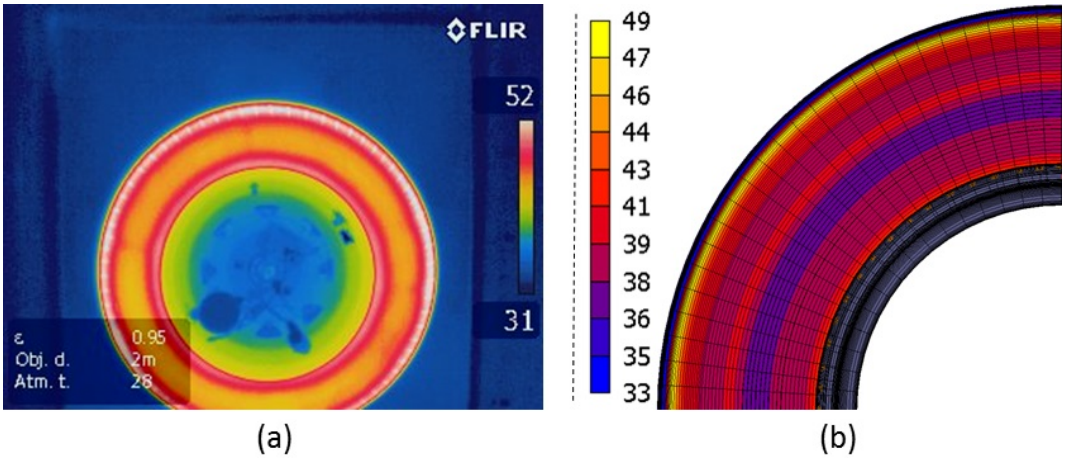

Figure 7.9: Sidewall temperature (°C) comparison for 500 kg and 175 kPa, with (a) experimental and (b) simulated (revised materials) results.

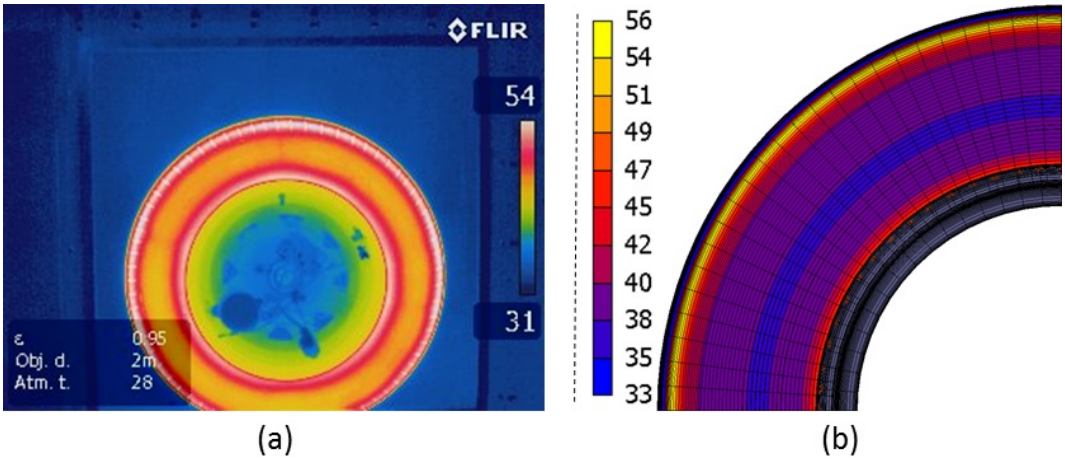

Figure 7.10: Sidewall temperature (°C) comparison for 700 kg and 250 kPa, with (a) experimental and (b) simulated (revised materials) results.

7.5 Comparison to original materials

An evaluation of the cross sectional equivalent of total strain distributions within the tire region under maximum radial deformation, as obtained from the loading analysis simulations (Section 5.3.2), yielded compelling results. As shown in Figure 7.11 for a load of 700 kg and inflation of 250 kPa, the revised simulation results clearly indicated strain peaks within the tire shoulder region. The Maritz simulation, in-turn, suggested an even distribution along the central sidewall region. This illustrates the differences in material stiffness between the experimentally established materials (revised) and those originally used by Maritz (2015).

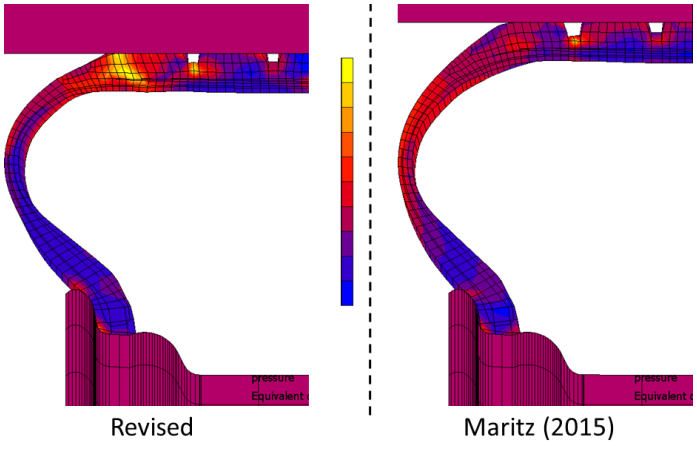

Figure 7.11: Cross sectional equivalent of total strain distribution comparison between revised and Maritz simulation results for a load of 700 kg and inflation of 250 kPa.

The Mooney Rivlin material models (Section 2.1) used to simulate the tire elastomer regions are invariant based treatments of rubber, as a function of the principal strain magnitudes. The elastic strain energy density obtained from the rolling analysis models (Section 5.3.3), that was in turn used to predict the rate of thermal heat flux due to hysteresis (Section 6.6 and 6.7), is therefore a function of the total (principal) strain due to deformation. As a result, the heat generation and steady-state temperature distributions within the tire would be representative of the total strains within its cross section. Figure 7.12 provides a cross-sectional illustration of the resulting temperature distributions obtained from using the revised and original (Maritz, 2015) materials for a load of 700 kg, inflation of 250 kPa and velocity of 60 km/h.

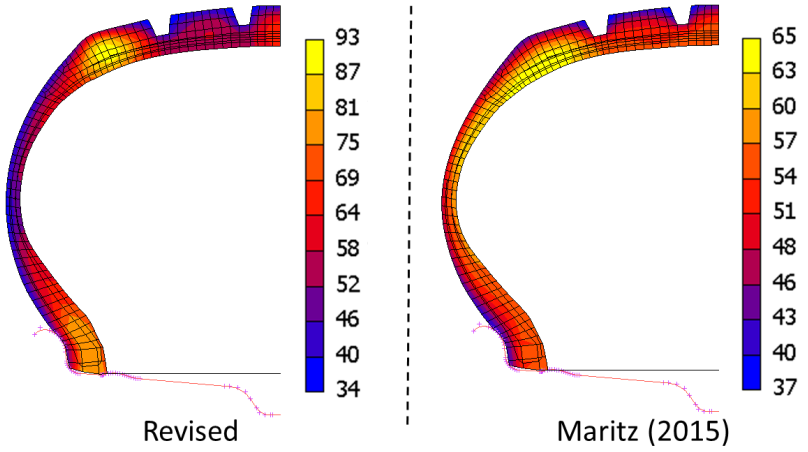

Figure 7.12: Cross sectional temperature distribution comparison between revised and Maritz simulation results for a load of 700 kg and inflation of 250 kPa.

The thermal distributions corresponded with those of the strains (Figure 7.11), with the revised material simulation model predicting a peak temperature within the tire shoulder region. Additional hot-spots were also present within the central tread and bead regions. In contrast, the Maritz material simulation suggested an even temperature distribution along the central sidewall region.

When comparing the external tread surface temperature distributions to an equivalent experimental thermal camera image, the advantage of using the experimentally determined materials become apparant. Figure 7.13 provides a comparison for an inflation of 250 kPa, load of 700 kg and rotational velocity of 60 km/h. Both numerical distribution profiles, as seen on the right, were plotted for the same temperature range, as per the legend.

As with the experimental results, the revised simulation model suggested a peak temperature within the tire shoulder region (1), along with additional temperature hot-spots within the central tread (2) and tread undercut groove (3) regions. This was in contrast to the Maritz simulation distributions, which suggested a peak temperature within the tread undercut groove (3) regions.

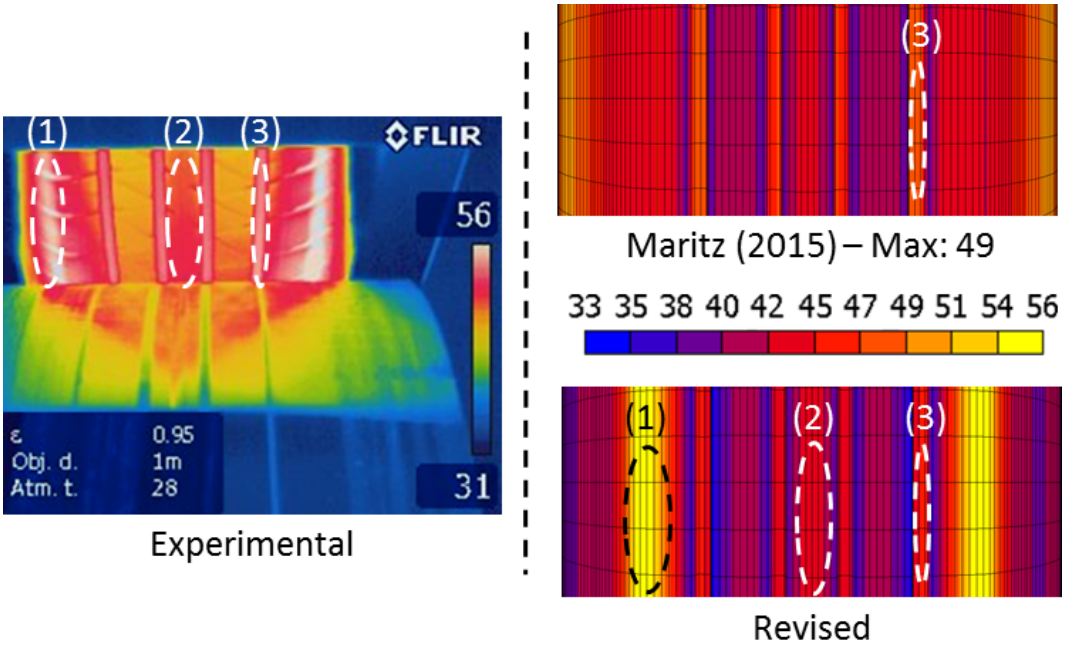

Figure 7.13: Tread region temperature (°C) comparison for a load of 700 kg and inflation of 250 kPa, illustrating experimental, revised and original (Maritz, 2015) simulation results. Both revised and Maritz results plotted for the same temperature range, as per the legend.

When evaluating the sidewall temperature distribution results for the same load case the results were similar, with the revised material simulations providing a significantly improved prediction. The results can be viewed in Figure 7.14, with both experimental and revised simulation distributions indicating a peak temperature within the tire shoulder region. This is followed, in both cases, by a cooler central sidewall and finally a slightly warmer bead region. The Maritz simulation contradicted these results, suggesting a peak temperature within the central sidewall region. A direct comparison of the external surface temperatures obtained from the revised and Maritz simulations is illustrated in Figure 7.15, providing additional insight to the temperature distribution variations.

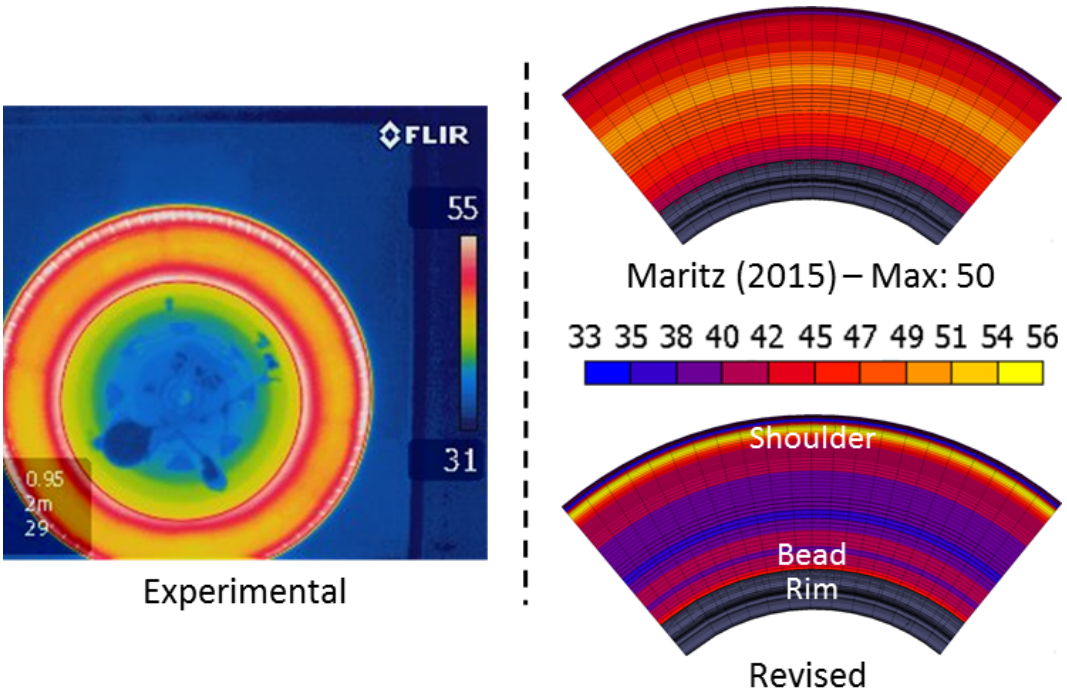

Figure 7.14: Tread region temperature (°C) comparison for a load of 700 kg and inflation of 250 kPa, illustrating experimental, revised and original (Maritz, 2015) simulation results. Both revised and Maritz results plotted for the same temperature range, as per the legend.

Figure 7.15: External surface temperature comparison between revised and Maritz simulation results for a load of 700 kg and inflation of 250 kPa.

7.6 Reduced rotational velocity

The model's thermal prediction capabilities were evaluated for a reduced velocity of 20 km/h. The rate of heat generation and elastomer hysteresis coefficient values are both a function of the wheels rotational frequency (Section 2.5 & 4.4.2). Furthermore, the external forced convection film coefficient value is a function of the relative air velocity. These factors would alter the tire's thermal behaviour, irrespective of the negligible influence of velocity on the models elastic strain energy density response (Section 6.5.2). Simulation results were subsequently compared to experimental measurements for the internal cavity, tread and sidewall regions. A comparison to results obtained from using the original material parameters (Maritz, 2015) was also conducted.

Results obtained for the internal cavity surface can be viewed in Figure 7.16 for three load cases. The numerical results all exhibited similar trends, with temperature peaks within the shoulder and central tread (1) regions. This corresponded with the results obtained from the 60 km/h load cases. The most promising predictions were obtained for the high load (700 kg) and inflation pressure (250 kPa) load case.

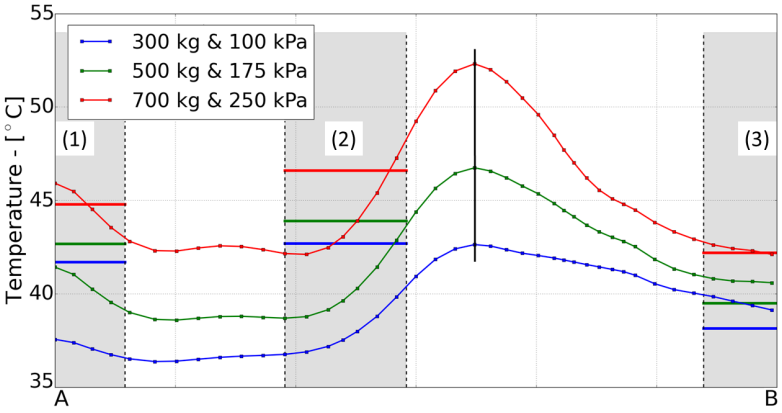

Figure 7.16: Internal cavity temperature results comparison for a reduced velocity of 20 km/h. Area-average experimental temperature results represented by horizontal coloured lines, with grey columns (1, 2 & 3) illustrating IR sensor measurement regions with reference to Figure 6.3.

Simulation results of the external tread surface corresponded well to experimental temperature distributions for the reduced rotational velocity load cases. The models tended to slightly over predict the maximum values, again being located within the shoulder, central tread and circumferential groove regions. A typical comparison is shown in Figure 7.17, with (a) being experimental and (b) numerical. The influence of inflation pressure and load variations on the distributions were the same as observed during the 60 km/h load cases.

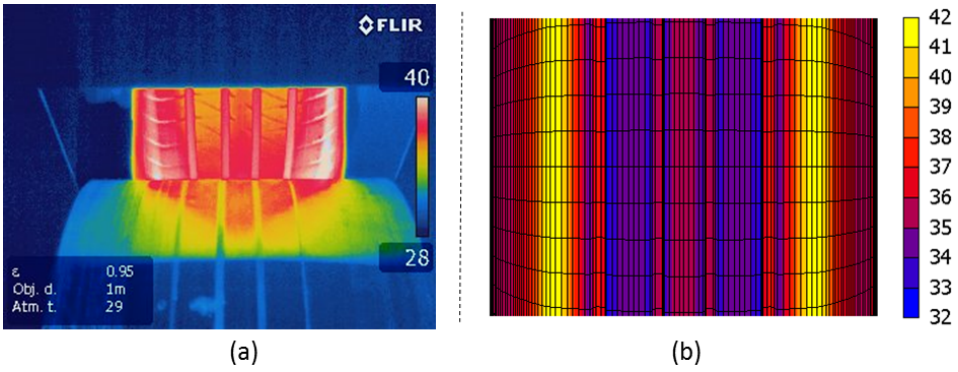

Figure 7.17: Low speed (20 km/h) tread region temperature (°C) comparison for 500 kg and 175 kPa, with (a) experimental and (b) simulated (revised materials) results.

Figure 7.18 illustrates the slightly under-predicted sidewall profile temperatures obtained for a low load (300 kg) and inflation pressure (100 kPa). Maximum temperatures were located within the shoulder and bead regions, while the central sidewall was notably cooler. These distribution trends, as well as the model's response to inflation and load variations, were similarly noted for the 60 km/h load cases.

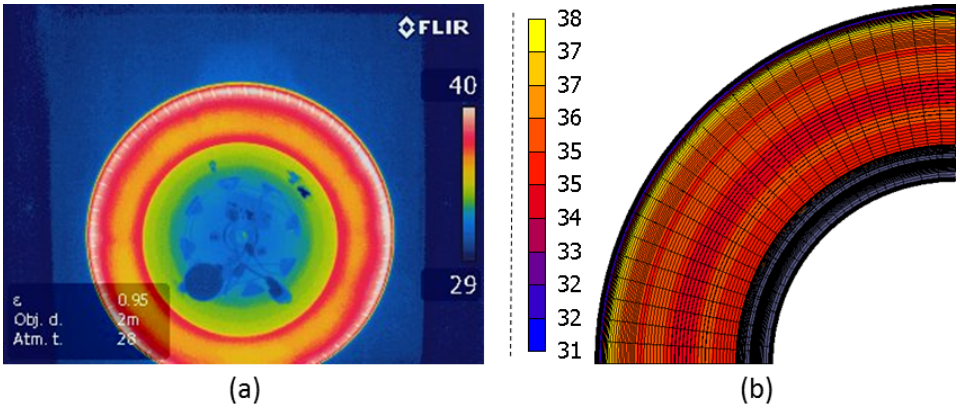

Figure 7.18: Low speed (20 km/h) sidewall temperature (°C) comparison for 300 kg and 100 kPa, with (a) experimental and (b) simulated (revised materials) results.

The improvement in the model's prediction capabilities due to the use of the updated material parameters was also evident for the low velocity simulations. Figure 7.19 shows a typical cross sectional comparison to the results obtained from using the original materials. The reduced material stiffness resulted in a more appropriate and realistic distribution of the hysteresis induced heating.

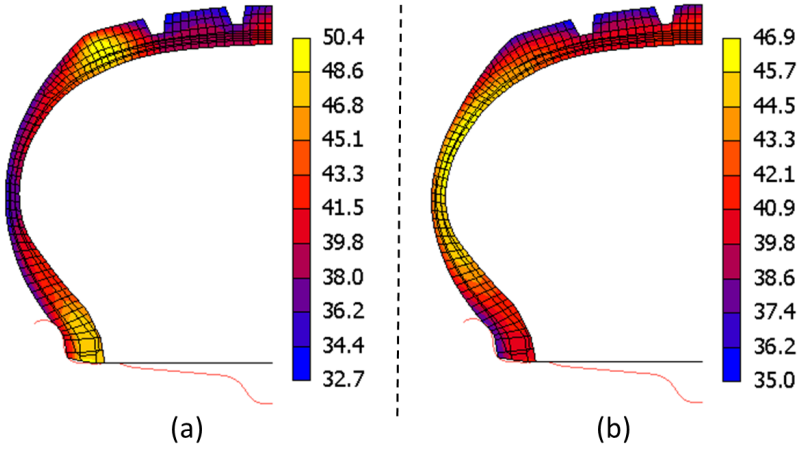

Figure 7.19: Low speed (20 km/h) cross sectional temperature (°C) comparison using revised (a) and original (b) material parameters for 500 kg and 175 kPa.

7.7 Conclusion

This chapter provided a comparison between experimental measurements and numerical predictions of the temperature distributions within an automotive truck tire under steady-state rolling conditions. The internal cavity, external sidewall and tread surface regions were of interest, with experimental measurements being obtained using the built-in test-bench IR temperature sensors and a hand-held Flir thermal camera.

Temperatures were identified to be a maximum within the shoulder, circumferential tread grooves and bead regions for all load cases, whilst the central tread and sidewall regions had notably lower operating points. Simulation models using the revised material parameters were able to replicate this behaviour to a fair extent, with emphasis on the high load and inflation load cases. This was also verified for a change (reduction) in rotational wheel velocity. For a load of 700 kg and inflation of 250 kPa, the models provided the best prediction of both the internal and external surface regions.

The significance of using the experimentally obtained (revised) material parameters was highlighted by a comparison with results obtained from using the original materials. The material definitions used by Maritz (2015) provided inaccurate results with regards to both magnitude and distributions. The majority of heat was focused within the central and upper sidewall regions due primarily to the materials excessive stiffness. A correlation between the material (rubber) stiffness, resulting strain distributions and final thermal results was also identified. The deformation and resulting strain energy of the revised materials was adequate to provide significantly improved prediction results.

Chapter 8

Conclusion

The overall project goal was to experimentally determine and validate the material properties of an automotive truck tire for use in a series of structural and thermal FE simulation models. The models originally created by Maritz (2015) made use of material definitions sourced from published literature. They lacked the ability to accurately predict deformation and steady-state rolling temperature distributions of the modelled tire. This was primarily due to the use of a single, extensively stiff, elastomer (rubber) material region across its entire cross section. The actual tire, however, consisted of three individual rubber regions, with varying degrees of material stiffness.

To achieve the project goal (Section 1.2) and improve simulation results, a series of objectives, as listed in Section 1.3, had to be achieved. During the execution of the project all of these objectives were successfully completed, thereby reaching the goal. The major project findings and conclusions are presented in the following sections of this chapter, along with a set of recommendations for future continuation.

8.1 Material parametrisation

Uni-axial tensile tests were executed to attain the stress-strain response curves of samples from a 215/70R15 steel-belted radial tubeless tire. Appropriate locations and orientations were selected in order to minimise the number of sample types. This made it possible to obtain the response of each material region through a combination of direct curve fits and iterative optimisation procedures. The complex tire geometry and construction made it impractical to attain appropriate tensile samples for each individual material.

Two- and three-term variants of the third-order Mooney-Rivlin elastomer model provided excellent fits for the rubber materials. Isotropic material definitions were used to represent the structural rebar reinforcements. The stress-strain response curves of combined material tensile test simulation models provided acceptable representations of experimental test data when using the identified material properties. Results obtained from a dynamic mechanical analysis of the rubber materials dismissed the use of the popular hysteresis coefficient value of 0.1, as previously obtained from literature.

8.2 Simulation models

The material properties and definitions were updated from those originally proposed by Maritz (2015). Minor alterations were also made to the reinforcement rebar definitions to better match measured values. Adjustments to load case parameters were made where required in order to aid model convergence due to reduced stiffness of the new materials. The overall modelling concept of three consecutive structural simulations for the inflation, loading and rolling, followed by a fourth thermal analysis remained unaltered. The process of downstream data transfer between consecutive models was streamlined by using a combination of Python scripts and MSC Marc procedure files. The structural deformation of the tire models during the inflation and load application phases saw significant improvements. Experimental sidewall deformation and tread contact patch profiles matched exceptionally well. The significance of using the experimental material properties was further highlighted by comparison of results obtained from using the original materials.

8.3 Thermal analysis and comparison

The tire temperature distributions were evaluated and compared under steady-state rolling conditions for a variety of load and inflation pressure increments. Experimental measurements were attained from a rolling drum tire test bench and hand-held thermal camera. Numerical distribution trends of the external tread and sidewall surfaces corresponded well with experimental results, with maximum values located within the shoulder, circumferential grooves and bead regions. The central tread and middle sidewall regions had cooler overall operating temperatures in both cases. For high load and inflation pressures the models provided the best predictions of the measured tire response. In addition, a change in the rotational wheel velocity did not hinder the model's prediction capabilities.

Use of the experimentally attained material parameters resulted in excellent thermal prediction capabilities. Furthermore, the advantage of using experimentally determined material parameters was highlighted by a comparison

with temperature distribution results obtained from using the original material definitions (Maritz, 2015). The previously used, excessively stiff, elastomer materials resulted in large strain concentrations within the sidewall regions during deformation. The models now provided a more accurate representation of the actual tire response, with similar temperature distribution patterns and magnitudes.

A clear and definitive correlation could not be identified between the internal cavity temperature measurements and external surface distributions. The thermal behaviour of a tire is too complex to be predicted by the analysis of a single region's response, such as the internal or external surfaces. In order to prevent the occurrence of pyrolysis and thermo-oxidation within a tire, both regions must be monitored individually. An alternative would be to measure the central rubber temperature by means of a permanently infused sensor device.

8.4 Future work

The tread pattern of the tire was simplified by only including the major circumferential grooves in order to reduce the required modelling and computational expenses. Future work can incorporate the individual tread pattern blocks, as to obtain a more accurate representation of the tire. This would increase to the ability of the model to simulate the influence of rolling resistance on strain energy and heat generation. The method of expansion from the axisymmetric to 3-D tire model would have to be revised in order to do so.

A computational fluid dynamic (CFD) analysis of the tire can be used to provide a more realistic approach for the modelling of external forced convection on the tread and sidewall regions during rotation. The results would require validation by means of an equivalent experimental analysis. This would require extensive alterations to the current tire test bench facility, as well as specialised sensors to measure the convective heat flux behaviour on the tire surface.

A chemical analysis on the heat transfer properties of the tire rubber and reinforcement materials should be conducted in order to validate the currently used values obtained from published literature. The tire test bench facility should be upgraded to provide a wider range of temperature readings. Additional sensors could be placed within the tire cavity in order to provide measurements of its entire surface region. This would enable a more comprehensive comparison to the simulated cavity surface temperatures. The sensors and method of installation would need to be robust in order to withstand cyclic tire loads and rotational forces, without hindering the air seal of the cavity.

Appendices

Appendix A

Digital Image Correlation procedures

The required calibration and post-processing procedures for using the LaVision StrainMaster 2D/3D DIC equipment is provided in the following Appendix. Figure A.1 shows its components mounted on a portable tri-pod stand, as typically used during the execution of the project. Please refer to Appendix B for equipment specifications.

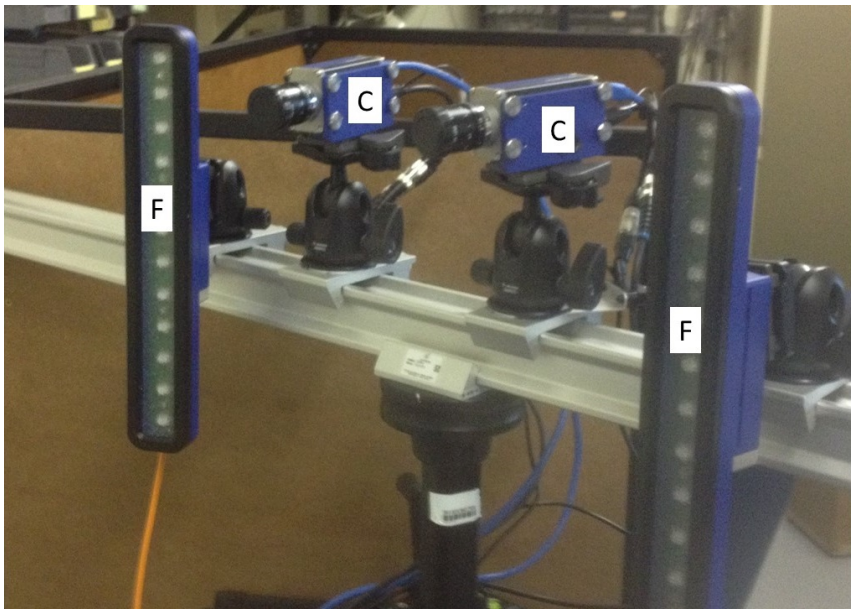

Figure A.1: LaVision Digital Image Correlation equipment used for strain-based measurement of tire samples and sidewall deformation profile analyses. It comprised of two digital cameras (C), with LED illumination strobe lights (F) on either side.

A.1 Calibration

In order to obtain accurate results the DIC apparatus must be calibrated every time before use. Failure to do so would results in inaccurate measurements. The required steps are as follows:

1. Adjust cameras and light-sources:
    - Adjust camera and led light-source positions to be horizontally in-line with and facing towards the intended measurement (deformation) zone. Cameras should ideally be located on both sides of the data acquisition unit on the stand, with one light source at each end.
    - Select *LiveRecording* mode within the DaVis software to view camera video feed.
    - Adjust camera distance as to capture the complete speckle region applied to the area of interest. The entire initial and final deformed states should be captured.
    - Light sources should not reflect into camera view, as this would blur the image.
2. Adjust camera focus and aperture:
    - Ensure speckle pattern is in focus by adjusting camera focus by hand.
    - The *DynamicRange* values should be approximately 10.8.
3. Calibrate cameras:
    - Place calibration plate in front of the deformation zone.
    - Take one image, saving it appropriately.
    - Select *StrainCalibration* option, ensuring an *AverageDeviation* of less than 0.5 pixels for each camera..
    - Adjust camera position, focus and light source angles until acceptable deviations are acquired.

A.2 Processing

Following a DIC measurement the raw test data must first be processed via the $Surf + Vectors$ option within the DaVis software. The process is as follows:

1. Define $Mask$ and $SeedingPoints$:
   - Include entire speckle pattern region of interest.
   - Add one point within every 'in-tact' sample section. Multiple seeding points to be used in the event of a discontinuities within the region of interest.
2. Set $SubsetSize$ to equal no. pixels within one speckle. Zoom in on the image to do this.
3. Set $StepSize$ equal to half of Subset.
4. Select appropriate image range, dis-regarding past point of sample failure.
5. Start processing and export data.

Appendix B

Equipment specifications

Specifications of the specialised equipment used during the execution of the project is provided in the following Appendix.

Table B.1: Metex M-3850D digital multimeter.

Parameter	Value
Operating temperature	0-40°C
Min DC voltage	400 mV (100 μV resolution)
Max DC voltage	400 V (100 mV resolution)
Min AC voltage	400 mV (100 μV resolution)
Max AC voltage	400 V (100 mV resolution)
Min DC current	400 μA (100 nA resolution)
Max DC current	20 A (10 mA resolution)
Min AC current	400 μA (100 nA resolution)
Max AC current	20 A (10 mA resolution)
Min resistance	400 Ω (0.1 Ω resolution)
Max resistance	40 MΩ (1 kΩ resolution)
Min frequency	4 kHz (1 Hz resolution)
Max frequency	40 MHz (10 kHz resolution)

Table B.2: LaVision StrainMaster DIC.

Parameter	Value
Camera resolution	1 600 × 1 200 pixels
Camera dynamic rate	12 bit
Camera shutter gate	1 μs
Camera speed	30 frames/s
Accuracy	40 μstrain locally 3 μstrain globally
Optics	f=50 mm; 1:1.8

Table B.3: LaVision StrainMaster Controller DAC.

Parameter	Value
Sample resolution	16 bit
Sample rate	250 kHz (total)
No. channels	8
No. cameras	2
No. illumination units	2

Table B.4: MTS Criterion Model 44 tensile tester.

Parameter	Value
Max. rated load capacity	30 kN
Force measurement accuracy	± 1 % of applied force
Max. test speed	1020 mm/min
Min. test speed	0.005 mm/min
Position accuracy	within ± 0.5 % of set position
Total crosshead travel	1000 mm

Table B.5: IR Calex PyroCouple.

Parameter	Value
Measurement range	0 to 250 °C
Ambient range	0 to 70 °C
Emissivity	0.95
Spectral response	8 to 14 μm
Response time	240 ms

Table B.6: 5151 Tekscan I-scan pressure pad.

Parameter	Value
Matrix width	165.4 mm
Matrix height	165.4 mm
Total no. sensels	1 936
Resolution	7.1 sensels per sq-cm
Max. pressure	2 413 kPa

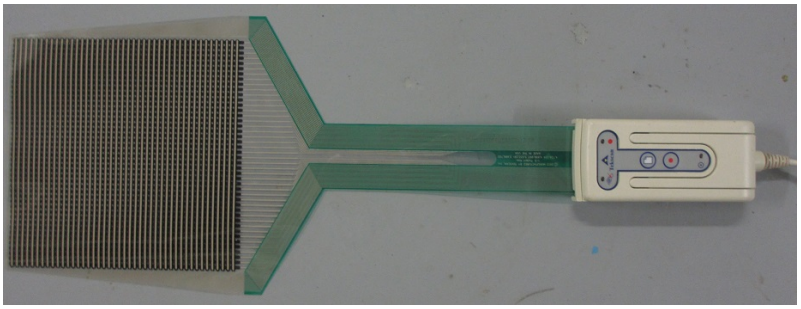

Figure B.1: 515 Newton Tekscan I-scan Evolution pressure pad and USB handle used for contact patch measurements.

Table B.7: Flir model E60 0.10 thermal camera

Specifications	
Measurement range	-20 to 120 °C
Field of view	25 °
Measurement distance	0, 1 or 2 m
Settings	
Emissivity	0.95
Atmospheric temperature	29 °C

Appendix C

Simulation model load and load case particulars

The following Appendix supplies additional information on the revised numerical simulation models, with reference to Chapter 5. Details on the load case parameters used to control the various boundary conditions within each model are provided. The circumferential expand patterns used when constructing the loading and rolling meshes are also included.

Table C.1: Modelling parameters used for all Cavity Pressure Loads.

Modelling parameters	
Solution procedure	Iterative
Polytropic process exponent	1
Ambient pressure	101.33 kPa
Reference properties	
Reference pressure	100 kPa
Reference temperature	298.15 K
Reference density	1.14 kg/m^3

Table C.2: Inflation load case: both inflation and thermal analyses.

Parameters	
Load case time	2 s
Initial fraction of load case time	0.01
Minimum fraction of load case time	1e-005
Maximum fraction of load case time	0.5
Desired number of recycles/increments	5
Time step increase factor	1.2
Max number of recycles	10
Iterative procedure	Full Newton Raphson
Damping ratio	0.0002
Convergence criterion	
Type	Relative residual
Relative force tolerance	0.001

Table C.3: Load application load case: both loading and rotational analyses.

Parameters	
Load case time	1.5 s
Initial fraction of load case time	0.0001
Minimum fraction of load case time	1.00E-09
Maximum fraction of load case time	0.05
Desired number of recycles/increments	90
Time step increase factor	1.2
Max number of recycles	180
Iterative procedure	Full Newton Raphson
Damping ratio	0.0002
Convergence criterion	
Type	Relative residual
Relative force tolerance	0.001

Table C.4: Rotational load case: rolling analysis.

Parameters	
Load case time	0.85 s
Initial fraction of load case time	0.001
Minimum fraction of load case time	1e-007
Maximum fraction of load case time	0.05
Desired number of recycles/increments	45
Time step increase factor	1.2
Max number of recycles	90
Iterative procedure	Full Newton Raphson
Damping ratio	0.0002
Convergence criterion	
Type	Relative residual
Relative force tolerance	0.001

Table C.5: Heating load case: thermal analysis.

Parameters	
Load case time	1e+006
Initial fraction of load case time	0.01
Minimum fraction of load case time	1e-005
Maximum fraction of load case time	0.5
Desired number of recycles/increments	5
Time step increase factor	1.2
Max number of recycles	10
Iterative procedure	Full Newton Raphson
Damping ratio	0.0002
Convergence criterion	
Type	Relative residual
Relative force tolerance	0.001

The following two tables provide details on the expand repetitions and angles used during the construction of the loading and rolling model meshes from an initial axi-symmetric model.

Table C.6: Expand settings: loading analysis model.

Angle	no. Repetitions
2.5°	18
5°	6
7.5°	6
10°	12
7.5°	6
5°	6
2,5°	18

Table C.7: Expand settings: rolling analysis model.

Angle	no. Repetitions
2.5°	5
5°	6
7.5°	5
10°	20
7.5°	5
5°	6
2.5°	5

List of References

Assaad, M.C., Kimble, B., Huang, Y.M., Burgan, R., Fralick, G.C., Wrbanek, J.D. and Gonzalez, J.M. (2008). Thin film heat flux sensor for measuring film coefficient of rubber components of a rolling tire. *Tire Science and Technology*, vol. 36, no. 4, pp. 275–289.

Baranowski, P., Bogusz, P., Gotowicki, P. and Malachowski, J. (2012). Assessment of mechanical properties of offroad vehicle tire: Coupons testing and fe model development. *Acta mechanica et automatica*, vol. 6, no. 2, pp. 17–22.

Boyce, M.C. and Arruda, E.M. (2000). Constitutive models of rubber elasticity: A review. *Rubber Chemistry and Technology*, vol. 73, no. 3, pp. 504–523.

Browne, A.L. and Wickliffe, L.E. (1980). Convective heat transfer coefficients at the tire surface: A parametric study. *GM Research Publications GMR*.

Carwile, L.C.K. and Hoge, H.J. (1966). Thermal conductivity of soft vulcanized natural rubber: Selected values. Tech. Rep. 3, Pioneering Research Division U. S. Army Natick Laboratories, Natick, Massachusetts.

Cengel, Y.A. and Ghajar, A.J. (2015). *Heat and Mass Transfer: Fundamentals and Applications - Fifth Edition in SI Units*. 5th edn. McGraw-Hill Education, New-York, NY.

Cho, J.R., Lee, H.W., Jeong, W.B., Jeong, K.M. and Kim, K.W. (2013). Numerical estimation of rolling resistance and temperature distribution of 3-d periodic patterned tire. *International Journal of Solids and Structures*, vol. 50, no. 1, pp. 86–96.

Conradie, J.M. (2014). *Finite Element Modelling of Off-Road Tyres*. Mechanical Engineering, University of Pretoria, Pretoria, South Africa.

Cook, R.D., Malkus, D.S., Plesha, M.E. and Witt, R.J. (2002). *Concepts and Applications of Finite Element Analysis*. 4th edn. John Wiley and Sons, Inc., Wisconsin, Madison.

du Plessis, A., le Roux, S.G. and Guelpa, A. (2016). The ct scanner facility at stellenbosch university: An open access x-ray computed tomography laboratory. *Nuclear Instruments and Methods in Physics Research B*, , no. 384.

Ebbot, T.G., Hohman, R.L., Jeusette, J.P. and Kerchman, V. (1999). Tire temperature and rolling resistance prediction with finite element analysis. *The Journal of the Tire Society*, vol. 27, no. 1, pp. 2–21.

Hild, F. and Roux, S. (2006). Digital image correlation: from displacement measurement to identification of elastic properties: a review. *Strain: An International Journal for Experimental Mechanics*, vol. 42, no. 2, pp. 69–80.

Kovac, I. and Krmela, J. (2012). Fe analysis of automobile tire. In: *Advanced Research in Scientific Areas*, vol. 1, pp. 1809–1812.

Kumar, N. and Rao, V.V. (2016). Hyperelastic mooney-rivlin model: Determination and physical interpretation of material constants. *MIT International Journal of Mechanical Engineering*, vol. 6, no. 1, pp. 43–46.

Lin, Y. and Hwang, S.J. (2004). Temperature prediction of rolling tires by computer simulation. *Mathematics and Computers in Simulation*, vol. 67, no. 1, pp. 235–249.

Maritz, J.C. (2015). *Numerical Modelling and Experimental Measurement of the Temperature Distribution in a Rolling Tire*. Mechanical Engineering, Stellenbosch University, Stellenbosch, South Africa.

MSC (2010). *Experimental Elastomer Analysis*. MSC Software Corporation, Santa Ana, CA.

MSC (2013). *Basic Nonlinear Analysis using Marc and Mentat: MAR101 Course Notes*. MSC Software Corporation, Santa Ana, CA.

Tang, T., Johnson, D., Smith, R.E. and Felicelli, S.D. (2014). Numerical evaluation of the temperature field of steady-state rolling tires. *Applied Mathematical Modelling*, vol. 38, no. 1, pp. 1622–1637.

Volschenk, A.D. (2015). *Commissioning of an Automotive Wheel Test-Bench*. Mechatronic Engineering, Stellenbosch University, Stellenbosch, South Africa.

VR&D (2001). *DOT Users manual*. Vanderplaats Research & Development Inc., Colorado Springs, CO., 5th edn.

Vu-Khanh, T., Dolez, P., Arrieta, C., Nohilé, C. and Ha-Anh, T. (2008). Exploratory study of heavy truck tire blowout and explosion phenomena. *Safety Science*, vol. 46, no. 9, pp. 1334–1344.